Università di Pisa

Facolta di Scienze Matematiche Fisiche e Naturali

Corsi di Laurea Specialistica in Scienze Fisiche

Anno Accademico 2004-2005

Tesi di Laurea Specialistica

LIGO-P050032-00-R

Experimental study of a non-gaussian Fabry-Perot resonator to depress mirror thermal noise for gravitational waves detectors

Candidato

Marco Giacinto Tarallo

Relatore

Dr. Phil Willems

Dr. Riccardo DeSalvo

Prof. Francesco Fidecaro

Contents

Chapter 1

Introduction

General Relativity predicts that massive accelerating and rotating stellar objects emit gravitational waves which propagate through space with the speed of light. These waves appear as special solutions of the field equations in general relativity. Such solutions were found by Einstein in 1916 [1] but the predicted strength of their interaction appeared so weak that until the seventies the real existence of gravitational waves was in doubt. Any attempts to directly detect gravitational waves have not been successful yet. However, their indirect influence has been measured in the binary orbital decay of the neutron star system PSR1913+16 [2] [3]. This convinced the scientific community about the possibility of gravitational wave detection.

The last twenty-five year saw the birth and diffusion of this new field of research: gravitational wave physics. Two kinds of gravitational wave detectors have been constructed and now are operating around the world, *resonant bar* detectors and *light interferometers* detectors. In particular, since the 1990s the construction of large scale Gravitational Wave Interferometric Detectors (GWIDs) was funded in several countries. GWIDs developed the idea of Michelson's interferometric experiment to measure the phase shift of its fringes induced by a gravitational wave pass through the detector.

Some of the GWIDs use Fabry-Perot cavities as sensing devices for such interferometers, so that these interferometric antennas measure the variation of the phases between the light beams that come out of two perpendicular identical Fabry-Perot cavities. The effect of a gravitational wave is a squeezing for one of them while the other will be stretched. The variation that is measured depends on any displacement of the reflective surfaces of the two mirrors. Such physical displacement can be caused by fundamental

noise sources and it can also mimicked by the measurement, because of any technical noise affecting the detection process.

At the moment, all GWIDs are using proved concepts and technologies in order to collect and analyze gravitational wave data quickly, reaching a detection range for inspiraling binary neutron stars of about 10 Mpc in the case of the LIGO interferometers. Future generation of detectors have the ambitious goal to improve the strain sensitivity by a factor 10 up to the standard quantum limit and beyond. The sensitivity will be dominated by sources of fundamental noise which are the direct result of such physical mechanisms as the Brownian motion caused by thermal activity at non-zero temperature, or the statistical errors that affect the measurement due to discreteness of photons and their quantum nature.

In the frequency range of maximum sensitivity, mirror thermal noise is the dominant fundamental noise source. The probe used in GWIDs for measuring the position of the mirror is a gaussian-shaped laser beam. Because of its relatively small sampled area, the ordinary gaussian beam is not the optimal choice to minimize sensitivity to mirror thermal noise. Thorne et al. [4] proposed a new family of light beams, the *Mesa beams*, supported by special nonspherical mirrors, the so-called *Mexican hat* mirrors, to reduce the impact on the GWID sensitivity of thermal noise and make beating the standard quantum limit an achievable goal.

This thesis consists of the experimental work needed for the complete understanding of such new optics before a direct application in the next GWID generation.

Detailed experimental work has been performed on a prototype built in the LIGO laboratories of the California Institute of Technology. Started in the summer of 2003 by Willems, D'Ambrosio, DeSalvo and Simoni [5] [**?**], the aim of this experiment is to explore all of the main properties of such an optical cavity including: generating the designed Mesa beam; studying the reliability of its control; characterizing beam distortions due to surface imperfections and misalignments; measuring the efficiency of the coupling to a gaussian input beam.

It is possible to generate our desired flat-top, wider Mesa beam just reshaping the profile of one or both the facing mirrors of the optical resonator. The characteristic "Mexican hat" graded phase mirror profile has been designed to support a Mesa beam. Three test mirrors have been manufactured by the LMA laboratory (Lyon, France) in order to study the behavior of this

new family of laser beams in our Fabry Perot prototype.

As theoretical and design background for our experiment, this thesis deals with all the physical characteristics of finite size optical resonators and the related experimental issues like lock acquisition techniques. The main features of spherical resonators are highlighted as starting point for a detailed comparison with the Mexican hat case.

An overview of the Mesa beam design and the related theoretical issues we want quantify in the experiment is included.

The second part of this thesis treats all the experimental issues of our experiment: a Fabry-Perot, folded, suspended optical resonator 7 meters long conceived to store Nd:YAG laser light with optics sizes scaled down from the Advanced LIGO baseline parameters. It is placed inside a vacuum pipe and the spacing between the mirrors is determined by three INVAR rods. A cavity finesse of about 100 is achieved by choice of the reflectivity of the input (flat) mirror. The other two mirrors, the folding mirror, and the end mirror, which can be either a spherical or a Mexican hat mirror, have high reflectivity coatings. During this year of operations, the cavity was always operated in air. The stability of the mechanics has been tested with a spherical mirror, 8 meters radius of curvature. The input and output optics layout has been developed to match and study this preliminary cavity configuration.

The control electronics, necessary to keep the cavity locked on a resonance, have been made and assembled so that it is possible to use either a side-lock feedback on the laser frequency or the cavity length dithering technique. A high voltage driver circuit has been designed and assembled to drive the mirror piezo actuators.

A preliminary study of the cavity beam profile was performed for the spherical optics configuration: several beam profile samples of the fundamental mode and higher order modes were compared to the theoretical predictions.

The last part of this work was the characterization of the cavity behavior with the first Mexican hat mirror. Since spherical symmetry is lost for such a resonator, the resonant beam depends on the particular mirror and input beam alignment. Beam profiles recorded were compared with realistic simulations based on the Fast Fourier Transform implementation of the beam propagation and using the actual Mexican hat mirror map.

As result of the experimental work, several transverse electromagnetic

field patterns, which are the resonant modes of our cavity, showed a good agreement with the theoretical predictions for the cavity higher order modes. Finally, the first Mesa beam fundamental mode was acquired and analyzed. It reveals some deviations from the ideal Mesa beam which we believe are mainly due to imperfect cavity optics.

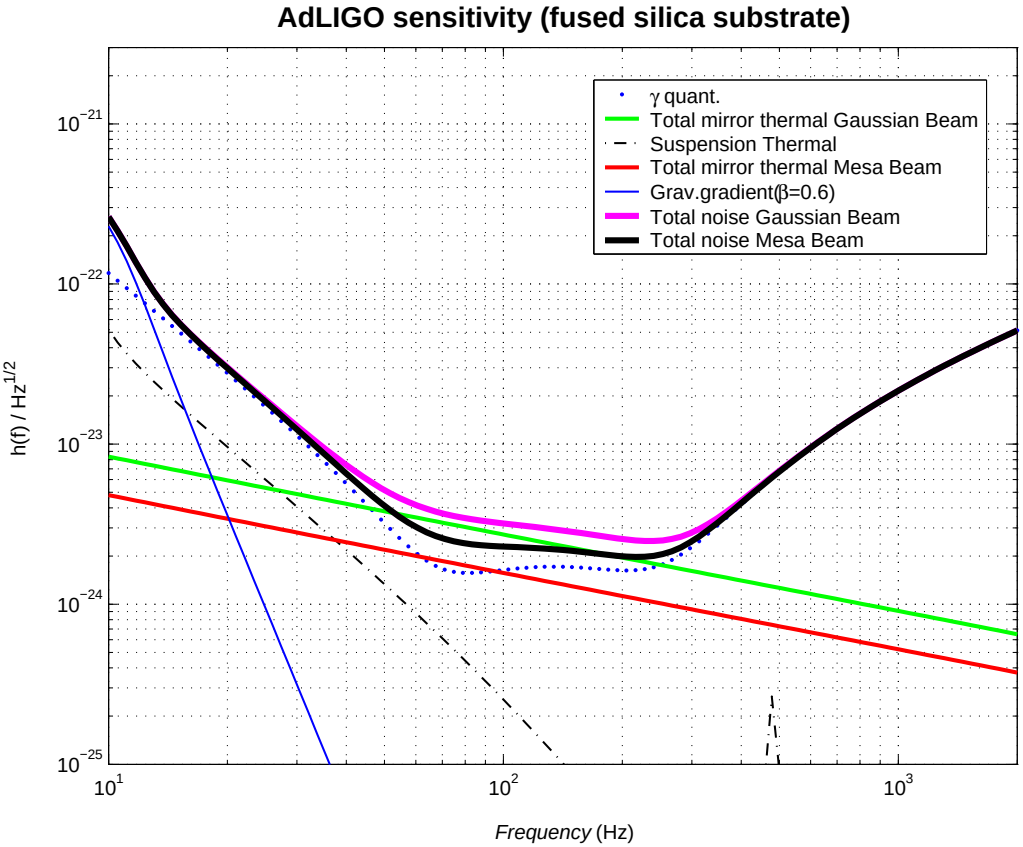

Figure 1.1: Sensitivity curve for the planned Advanced LIGO configuration with Fused Silica test masses. The black curve is the expected noise if the Mesa beam is employed

Chapter 2

Thermal Noise

In this chapter we want to point our attention to the theory of thermal noise evaluation and how thermal noise affects a Gravitational Wave interferometer sensitivity. In particular, starting from the Fluctuation-Dissipation theorem, we will show the relevant geometrical dependence of mirror thermal noises on the probing beam profile.

2.1 Fluctuation-Dissipation Theorem

The thermal motions are fluctuations of generalized coordinates of systems due to the energy that stochastically flows to and from the heat bath. Famous examples are the Brownian motion of small particles of pollen [6] and the fluctuation of the voltage across a resistance [7]. In gravitation experiments the thermal motion of mechanical oscillators is one of the limits of measurement. For these systems it can be evaluated from the the equipartition principle as the root mean square of the displacement due to a kinetic energy $k_b T$.

This approach is not adequate for interferometric gravitational wave detectors. Since they are characterized by high sensitivity in a broad frequency band, their thermal noise has to be evaluated from the whole system's dissipation properties. The Fluctuation-Dissipation Theorem (FDT), established by Callen et al. [8],[9],[10],[11], predicts thermal fluctuations relating the spectrum of the thermal motions to the dissipation of systems. Let's consider a one dimensional system and let's call X its generalized coordinate. The generalized force, F, represents the interaction between the system and

externals.

The information of the system dissipation is included in the response of X to F. This response is defined by several functions: the impedance Z, as

$$Z(\omega) \equiv \frac{\tilde{F}(\omega)}{i\omega\tilde{X}(\omega)} \tag{2.1}$$

where $\tilde{F}$ and $\tilde{X}$ are the Fourier components of the generalized force and coordinate, respectively. The admittance Y of the system is defined as the inverse of the impedance

$$Y(\omega) \equiv \frac{1}{Z(\omega)} \tag{2.2}$$

The real part of the impedance is called resistance of the system and the real part of the admittance is called the conductance.

The FDT states that the power spectral density of X and the response of the system are related by the formula

$$G_X(\omega) = \frac{4k_BT}{\omega^2}\ \mathrm{Re}[Y(\omega)] \equiv \frac{4k_BT}{\omega^2}\sigma(\omega) \tag{2.3}$$

This relationship is called the first fluctuation-dissipation theorem, which can be rewritten by using the definition of transfer function $H(\omega) \equiv \tilde{X}/\tilde{F}$ as

$$G_X(\omega) = -\frac{4k_BT}{\omega}\mathrm{Im}[H(\omega)]. \tag{2.4}$$

Fluctuations caused by the fluctuating force are also related to the system dissipation as

$$G_F(\omega) = 4k_BT\ \mathrm{Re}[Z(\omega)] \equiv 4k_BTR(\omega). \tag{2.5}$$

Equation (1.5) is known as the second fluctuation-dissipation theorem. The two FDTs are equivalent.

Sources of dissipation, and thus sources of noise in mechanical systems, are both external and internal losses. Typical examples of the external losses are the residual gas damping and the eddy current damping induced in a conductor moving in a magnetic field (as the magnets attached to the interferometer mirrors for the length positioning, which are controlled by coils actuators). In most cases, these kinds of damping are reduced sufficiently in a GWID. Thus, the dissipation is dominated by the internal losses in the mechanical system.

Two of the most important kinds of internal dissipation are *structural damping* and *thermoelastic damping*. The typical approach to internal loss mechanisms is the extension of the Hooke's law for elastic bodies adding an imaginary part to the elastic constant, described by the *loss angle* $\phi(\omega)$. Structural damping has a ϕ which doesn't depend on frequency. There isn't any clear model that explains this phenomenon. In fact it is physically impossible that the loss angle has no dependence on the frequency, since $\phi(\omega) \rightarrow 0$ for $\omega \Rightarrow 0$. In some cases a frequency independent ϕ has been attributed to friction from material dislocations [12]. The source of the friction in materials is always a bistable microstate that can oscillate between two energy levels separated by a small energy barrier. Dislocation movements for most metals, switching molecular bonds for glasses, protons flipping between different bond orbitals in all hydrogen adsorbing materials are examples of dissipation sources.

The thermoelastic damping is characterized by a loss angle with a broad frequency dependence around a certain characteristic frequency τ^{-1} described as

$$\phi(\omega) = \Delta \frac{\omega\tau}{1 + (\omega\tau)^2}, \tag{2.6}$$

where Δ represents the strength of the loss and τ corresponds to the relaxation time.

The theory of this mechanism was given by Zener [13],[14]. It is caused by an inhomogeneous strain of an elastic body. Since the thermal expansion coefficient is not zero, the strain changes the temperature in the elastic body. If the strain is inhomogeneous, a gradient of temperature occurs and thus a heat flow. The elastic energy is dissipated owing to this heat flow. Thus the time constant τ represents the typical relaxation time of the above gradient of temperature.

2.2 Test mass thermal noise

Thermal noise affects the light beam path in a gravitational wave detector through two different sources: pendulum suspension thermal noise and mirror thermal noise.

The induced noise displacement from the suspension wire dissipation has been evaluated by multi modal expansion and structural damping process with constant loss angle ϕ_p. Hooke's law establishes the relation between the

return force of the pendula and the suspension point displacement. Using the FDT it's possible to express the suspension noise as [15]

$$\tilde{X_p}(\omega) = \sqrt{\frac{4k_B T\omega_p^2\phi_p}{m}\frac{1}{\omega^5}}\ [\mathrm{m}/\sqrt{\mathrm{Hz}}], \tag{2.7}$$

at $\omega >> \omega_p$ (pendulum resonant frequency) and $\omega < \omega_V$ (violin frequency).

In the case of mirror thermal noise we have to distinguish among different dissipation processes:

Bulk Brownian noise : bistable states distributed homogeneously in the mirror substrate convert oscillating elastic energy into heat and perturb the position of the mirror's surface, this is usually called Brownian noise. The dissipation mechanism is not theoretically calculated but it is estimated by measurements of ring down Q factors and described as a constant ϕ (frequency dependent) dissipation model[1].

Thermoelastic noise : The oscillating squeeze and stretch of the substrate material causes an oscillating, inhomogeneous temperature distribution: heat flows down the temperature gradient in such a way that it converts oscillation energy into additional heat.

Mirror Coating noise : imperfections in the mirror coating material, and in the interface between the alternating layers of coating, yield heat when the coatings are squeezed and sheared in response to external forces. Both Brownian and thermoelastic dissipation mechanism are present.

Since it is very difficult to evaluate the transfer function of a mechanical system (such as a GW interferometer test mass), Levin [16] proposed a direct approach to the displacement of a test mass thermal noise: the FDT shows the relation between the thermal noise and the imaginary part of the transfer function of the dissipating system, which actually represents the energy dissipated in the system. Thus Levin rewrote the FDT using the dissipated energy W_{loss}

[1] In fused silica, the bistable states are Si-O-Si bonds that flex between two local equilibria. In this case, we do have a model which has a loss angle $\phi \propto f^{3/4}$ frequency dependence

$$G_X(f) = \frac{2k_B T}{\pi^2 f^2} \frac{W_{loss}}{F_0^2}. \tag{2.8}$$

The value W_{loss} is the average dissipated power when the oscillatory force, expressed as $F_0 \cos(2\pi f t) P(\mathbf{r})$ is applied on the system, where $P(\mathbf{r})$ is the pressure distribution applied on the surface. This more useful form of the FDT can be used to calculate the mirror thermal noise of a finite sized test mass.

2.2.1 Bulk Brownian noise

Thermal noise due to homogeneously distributed damping processes such as Brownian bulk noise in GW detector mirrors can be estimated using complex valued elastic coefficients whose imaginary part is related to the dissipation mechanism. For example, the structural damping can be parametrized by material's Young modulus

$$E = E_0[1 + i\phi], \tag{2.9}$$

Measurements have shown that ϕ is dependent on f, but its dependence is sufficiently slow that it can be neglected in the frequency region of interest.

To calculate the power spectral density associated to Brownian Bulk motions, we express W_{loss} in Eq. 2.8 as

$$W_{loss} = 2\pi f U_{max} \phi, \tag{2.10}$$

where U_{max} is the maximum energy of elastic deformation due to the oscillatory pressure previously defined. This energy is derived by using elasticity theory, and will depend on which monitoring beam profile you use as well as the mirror's dimensions. In the case when the beam has a gaussian profile and the mirror is approximated by a semi infinite half-space, the displacement spectral density will be about [17]

$$S_X^{BB}(f) \approx \frac{4k_B T}{f} \frac{1 - \sigma^2}{2\pi E_0 r_0 \sqrt{2\pi}} \phi, \tag{2.11}$$

$$\Rightarrow S_X^{BB}(f) \propto \frac{1}{r_0}. \tag{2.12}$$

In Eq. 2.11, I called E_0 and σ respectively the Young's modulus and Poisson ratio of the material, while r_0 is the beam radius for a gaussian

power distribution. The correction for finite size effect has been calculated by Bondu et al.[18] and corrected by Liu and Thorne and it could be as larger as several tens per cent [17].

As previously stated, bulk Brownian thermal noise has a geometrical dependence on the beam profile, but it is very weak since the rms of the induced displacement is proportional to $r_0^{-\frac{1}{2}}$.

2.2.2 Bulk thermoelastic noise

If test mass thermal noise was only due to Brownian fluctuations, the best requirement to choose a good substrate for GW interferometers would simply be a high quality factor Q_{int} (small loss angle) of internal mechanical modes of the mirrors.

Nonlinear effects as thermal expansion can transform, as previously pointed out, temperature fluctuations into surface fluctuations and so affects GW detection. The time scale in which these fluctuations assume importance is $\tau = f_{GW}^{-1}$, where f_{GW} is the typical frequency of the detection band. From thermodynamical arguments the length scale for the restoring heat flow is

$$r_T = \sqrt{\frac{\kappa}{C_V \rho}\tau}, \tag{2.13}$$

where κ is the characteristic thermal conductivity and C_V the specific heat of the substrate material. r_T is the length which establishes where the mirror thermodynamical fluctuations affect the surface displacement measured by the light beam. In a volume of about $(r_T)^3$, this displacement can be estimated as [19]

$$\Delta X = \alpha_{Bulk} \Delta T r_T \approx \alpha_{Bulk} r_T \sqrt{\frac{k_B T^2}{\rho C_V (r_T)^3}}. \tag{2.14}$$

The temperature fluctuations in such volumes can be considered as independent ones. The number of such volumes N that contribute to mirror surface fluctuations is roughly equal to the ratio between the cube of the beam radius and their volume, $N = (r_0/r_T)^3$. Then, the average surface noise displacement is

$$\bar{X}(f) = \frac{\Delta X}{\sqrt{N}} = \alpha_{Bulk} r_T \sqrt{\frac{k_B T^2}{\rho C_V r_0^3}} \propto r_0^{-3/2} \tag{2.15}$$

A detailed calculus of Bulk Thermoelastic noise, performed by Braginsky et al. [20] and refined by Liu and Thorne [17] gives the following result for the displacement power spectral density for a half infinite mirror:

$$S_X^{BTE}(f) = \frac{2}{\sqrt{2}\pi^{5/2}} \frac{\alpha_{Bulk}^2 k_B T^2 (1+\sigma)^2 \kappa}{(\rho C_V)^2 r_0^3 f^2} \tag{2.16}$$

Because of its large dependence on the medium thermal expansions coefficient thermoelastic noise can be the dominant source of noise in the frequency band $f_{GW} = 100Hz$ for mirror substrate with high α_{Bulk} like sapphire, even if it has a very low Q_{int}.

As we already seen in Eq. 2.15 by simple physical considerations, bulk thermoelastic noise can be drastically reduced using its relevant dependence on the beam size.

2.2.3 Coating noise

In order to use high reflectivity mirrors in GW interferometers, multi-layer optical coatings are applied to the mirror substrate surface. To obtain the required high reflectivity, multi-layers, dielectric coatings are used. Such coatings consists of alternating layers of two dielectric materials with differing refractive indexes (i.e., Ta_2O_5/SiO_2 for initial LIGO).

In particular, Levin [16] pointed out that, despite the relatively small thickness of these layers, the surface losses can lead to relevant thermal noises. Since the key quantity is the power dissipated when an oscillating pressure is applied, and that it is proportional to the square of the stress at each point where the pressure is applied, one expects that

$$W_{loss}^{coating} \propto \left(\frac{F_0}{r_0^2}\right)^2 r_0^2 = \frac{F_0^2}{r_0^2}, \tag{2.17}$$

$$\Rightarrow S_X^{coating} \propto \frac{1}{r_0^2}. \tag{2.18}$$

The total Brownian thermal noise of a test mass is proportional to the loss angle ϕ which can be experimentally estimated. If we consider the limit when the coating is very thin compared to the width of the pressure distribution, then

$$\phi = \phi_{substrate} + \frac{\delta U d}{U} \phi_{coating}, \tag{2.19}$$

where δU is the energy density stored at the surface integrated over the surface, U is the total energy stored in the mirror, and d is the thickness of the coating. Using again Levin's method with the new ϕ, it's possible to see that the coating Brownian noise contribution is [21]

$$S_X^{CB}(f) = \frac{k_B T}{\pi^2 f} \frac{(1+\sigma)(1-2\sigma)d}{E r_0^2} \phi_{coating}. \tag{2.20}$$

Since it has been measured that coating film loss angle is much higher than the substrate one (for fused silica $\phi_{substrate}/\phi_{coating} \approx 10^{-5}$), coating Brownian noise will be the fundamental limit in the highest sensitivity frequency band for Advanced LIGO which is planned to have fused silica substrates for its test masses.

Thermoelastic dissipation can also occur in the coating film. The mathematical approach to its evaluation is much more complex than to the other ones. In particular, it shows a different frequency behavior at high frequency [22]. In the frequency band $f < \tau_f^{-1}$, where τ_f is the thermal diffusion time across the film ($\tau_f^{-1} \simeq 6$ kHz for Ta_2O_5/SiO_2 multi-layer coating), coating thermoelastic noise can be estimated by the equation

$$S_X^{CTE}(f) = \frac{4 k_B T^2}{\pi^{3/2}\sqrt{f}} \frac{l^2}{r_0^2} (1+\sigma_s)^2 \frac{C_f^2}{C_s^2} \frac{\alpha_{Bulk}^2}{\sqrt{k_s C_s}} \Delta^2, \tag{2.21}$$

where Δ^2 is a dimensionless combination of material constants that vanishes when the film and substrate are identical,

$$\Delta^2 \equiv \left\{ \frac{C_s}{2\alpha_{Bulk} C_f} \frac{\alpha_{coating}}{(1-\sigma_f)} \left[\frac{1+\sigma_f}{1+\sigma_s} + (1-\sigma_s)\frac{E_f}{E_s} \right] - 1 \right\}^2, \tag{2.22}$$

2.3 Mesa beam test mass thermal noise

In this paragraph we'll anticipate some results about thermal noise reduction allowed by a reshaped stored beam with a flat top power distribution and larger radius: the Mesa Beam.

The table below summarizes the geometrical dependence of each kind of test mass thermal noise.

Thermal noise	$S(r_0)$
Bulk Brownian	r_0^{-1}
Coating (all kinds)	r_0^{-2}
Bulk Thermoelastic	r_0^{-3}

Table 2.1: Mirror thermal noises power spectral density dependence on the gaussian beam radius

The Mesa beam has been proposed for Advanced LIGO as an alternative to the usual gaussian beam in order to take advantage on the particular dependence on the light spot size. In particular, sapphire thermoelastic noise can be reduced by the use of Mesa beam testing light [23] because of its high dependence on the beam radius.

In the case of fused silica substrate, coating thermal noise is reduced to yield a sensitivity gain factor of about 1.7, as shown in the following figure [24].

In the end, mirror thermal noise reduction is the main motivation to study the features of such a resonators supporting flat top beam profiles.

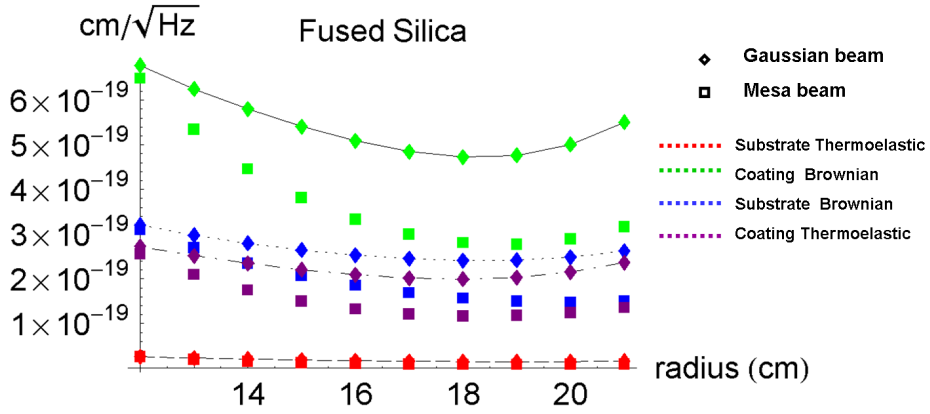

(a) Mirror displacements induced by each different contribute to test mass thermal noise vs. mirror size, at frequency $f = 100$Hz

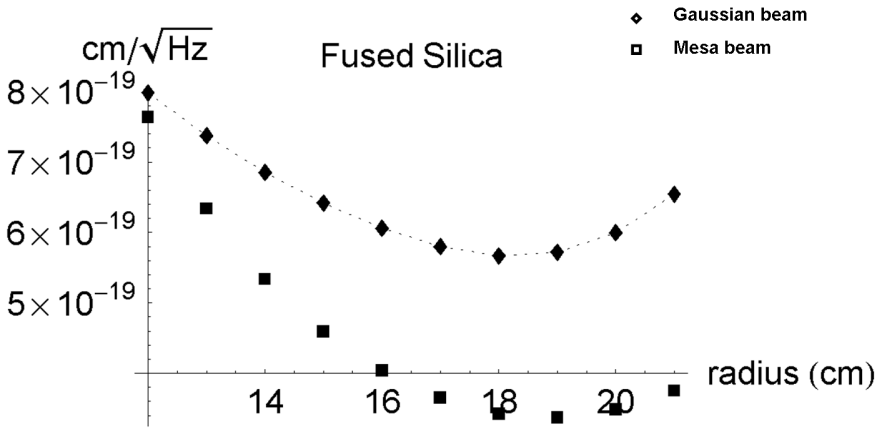

(b) Total thermal noise for gaussian beam and Mesa beam

Figure 2.1: Comparison between mirror thermal noises for gaussian and Mesa beam. The comparison was done by changing the aspect ratio of the mirror and keeping the total mass fixed at 40 kg, while the beam radii are adjusted in such a way that diffraction losses amounts always to 1 ppm

Chapter 3

Optical Resonators

Optical resonators are devices used to store a large amount of light. In particular one of these, the two mirror resonator or Fabry-Perot cavity (FP), has found a large application in GW interferometric detectors because of its ability to sustain light for times much greater than the photon transit time.

In this chapter we will present a brief description of laser beam theory in real resonators and then point our attention to the main features of the coupling of the incoming laser field with such an optical system. FP behavior for misaligned and unstable geometrical configurations, the resonance conditions and the lock keeping techniques will be discussed. All of the physical concepts and notations here introduced, will be applied in order to study and characterize our Mesa beam cavity.

3.1 Laser beams free propagation

A laser beam is coherent and monochromatic light. The phasor amplitude $\tilde{E}(x, y, z)$ of the field distribution satisfies the equation

$$\left[\nabla^2 + k^2\right] \tilde{E}(x, y, z) = 0, \tag{3.1}$$

where $k = 2\pi/\lambda$ is the wave number that characterizes the light propagation in the considered medium. For light traveling in the z direction, is convenient to write

$$\tilde{E}(x, y, z) = \psi(x, y, z)e^{-jkz}, \tag{3.2}$$

where ψ is a complex scalar wave amplitude which describes the transverse profile of the beam, and e^{-jkz} is the plane wave propagating in the z axis. Basically, the field amplitude slowly depends on the propagation direction, because this dependence is just due to diffraction effects. These considerations are translated into the *paraxial approximation* which consists of a dropping of the second partial derivative in z in Eq.3.1. The resulting paraxial wave equation is

$$\frac{\partial^2\psi}{\partial x^2} + \frac{\partial^2\psi}{\partial y^2} - 2jk\frac{\partial\psi}{\partial z} = 0, \tag{3.3}$$

or for a generic set of transverse coordinates $\mathbf{s}$,

$$\nabla_t^2\psi(\mathbf{s},z) - 2jk\frac{\partial\psi(\mathbf{s},z)}{\partial z} = 0. \tag{3.4}$$

A possible solution of Eq.3.3 is a scalar field ψ with a gaussian intensity profile, the so-called "*gaussian beam*":

$$\begin{aligned}\psi_{gauss}(x,y,z) &= \frac{1}{\tilde{q}(z)}\exp[-jk\frac{x^2+y^2}{2\tilde{q}(z)}] \\ &\equiv \frac{1}{\tilde{q}(z)}\exp[-jk\frac{x^2+y^2}{2R(z)} - \frac{x^2+y^2}{w^2(z)}],\end{aligned} \tag{3.5}$$

where the complex parameter $\tilde{q}$ has been expressed in the two more convenient real function $R(z)$ and $w(z)$, which are respectively the wavefront radius of curvature and the beam spot size. Their definition comes from the $\tilde{q}(z)$ parameter as follows:

$$\frac{1}{\tilde{q}(z)} \equiv \frac{1}{R(z)} - j\frac{\lambda}{\pi w^2(z)}. \tag{3.6}$$

The propagation law between two points in the optical axis z for $\tilde{q}(z)$ is established as

$$\tilde{q}(z_2) = \tilde{q}(z_1) + z_2 - z_1. \tag{3.7}$$

Except the polarization, the last two equations describe entirely all the physical properties of a coherent light beam with a gaussian intensity profile. In fact, manipulating them it is possible to observe that a gaussian beam contracts to a minimum diameter $2w_0$ at the *beam waist*, where the phase

front is plane. The two parameters $R(z)$ and $w(z)$ are determined by the waist size w_0 and by the distance z from the waist position as follows:

$$w^2(z) = w_0^2 \left[1 + \left(\frac{\lambda z}{\pi w_0^2} \right)^2 \right] \tag{3.8}$$

$$R(z) = z \left[1 + \left(\frac{\pi w_0^2}{\lambda z} \right)^2 \right]. \tag{3.9}$$

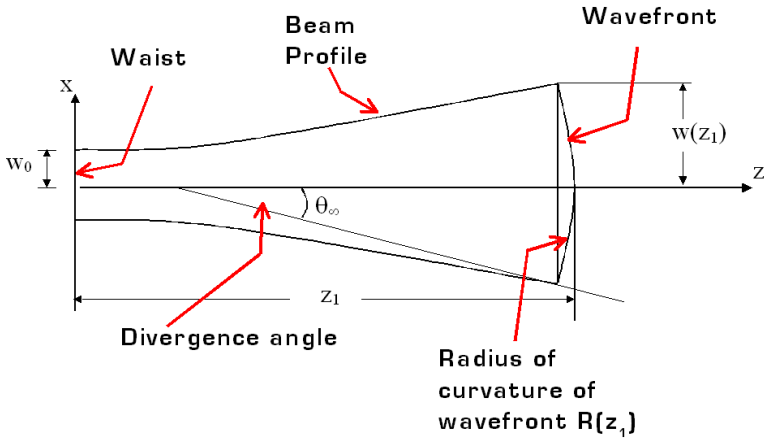

Figure 3.1: Free propagation of a gaussian beam

Thus, the contour of a gaussian beam is a hyperbola with an aperture angle θ, called the *divergence* of the beam, equal to

$$\theta_\infty = \frac{\lambda}{\pi w_0}. \tag{3.10}$$

The divergence angle characterizes the beam propagation in the "far-field" region. The region in which a gaussian beam can be considered collimated is $2z_R$, where $z_R \equiv \pi w_0^2/\lambda$ is the called "Rayleigh range", which is the quantity that marks the dividing line between the near-field and the far-field.

It is also possible define the *radius* of the beam $r_0 = w/\sqrt{2}$.

3.1.1 Higher order modes

The gaussian beam is not the only solution for Eq. 3.4. Solutions of Eq. 3.4 form a complete and orthogonal set of functions and are called the "modes of propagation" [25].

In particular, for a system with a rectangular (x, y, z) geometry, a complete set of solutions is furnished by the "Hermite-gaussian" functions:

$$\begin{aligned}\psi_{mn}^{HG}(x,y,z) &= \frac{A_{mn}}{w(z)} H_m\left(\sqrt{2}\frac{x}{w(z)}\right) H_n\left(\sqrt{2}\frac{y}{w(z)}\right) \times \\ &\times \exp\left[-\frac{x^2+y^2}{w^2(z)} - \frac{jk(x^2+y^2)}{2R(z)} - j(kz - \phi_{mn}(z))\right] \end{aligned} \quad (3.11)$$

where H_j's are the Hermite polynomials of order j, ϕ_{mn} is the Gouy phase defined as

$$\phi_{mn}(z) \equiv (m+n+1)\arctan\left(\frac{\lambda z}{\pi w_0^2}\right), \quad (3.12)$$

and A_{mn} is a normalization constant.

If the geometry of the system is cylindrical, a more suitable set of solutions are in general the Laguerre-gaussian solution of the form

$$\begin{aligned}\psi_{pl}^{LG}(r,\theta,z) &= C_{pl}\left(\sqrt{2}\frac{r}{w(z)}\right)^l L_p^l\left(2\frac{r^2}{w^2(z)}\right)\exp(-jl\theta) \times \\ &\times \exp\left[-\frac{r^2}{w^2(z)} - \frac{jkr^2}{2R(z)} - j(kz - \phi_{pl}(z))\right], \end{aligned} \quad (3.13)$$

where the generalized Laguerre polynomial L_p^l has been has been introduced. Now the Gouy phase can be expressed as function of the radial and angular order numbers as

$$\phi_{pl}(z) \equiv (2p+l+1)\arctan\left(\frac{\lambda z}{\pi w_0^2}\right). \quad (3.14)$$

Here L_p^l are the generalized Laguerre polynomials, while all the other quantities are exactly the same as in the Hermite-gaussian situation. In both cases, when the order numbers (m, n) (or (p, l)) are both zero, we obtain the

previous gaussian beam or TEM_{00}, which is also called the "fundamental mode".

Both the Hermite-gaussian functions and the Laguerre-gaussian functions provide a complete basis set of orthogonal functions. Each field of the set is characterized by a single complex parameter $\tilde{q}$ at any reference plane z_0. Thus, every beam can be expanded in the form [26]

$$\tilde{E}(x,y,z) = \sum_{m,n} c_{mn} \psi_{mn}^{HG}(x,y,z) e^{-jkz}. \tag{3.15}$$

The coefficient c_{mn} (or c_{pl} for the Laguerre-gaussian set) will depend upon the arbitrary choice of $\tilde{q}$ at z_0.

Real lasers are usually affected by some astigmatism or tilted surfaces that usually provides a small rectangular symmetry of the laser cavity, so that laser beams usually oscillate in near Hermite-gaussian rather than near Laguerre-gaussian modes.

Given a set of modes of propagation, every transverse field modes have a different Gouy phase, which means a different spatial frequency. In particular, from Eq.3.12 one sees that when the transverse mode order increases, the phase velocity increases with the mode number. If we take the fundamental mode frequency as reference frequency, the frequency spacing is given by the relation

$$\Delta\omega_{mn} = (m+n) \arctan\left(\frac{\lambda z}{\pi w_0^2}\right) = (m+n) \arctan\left(\frac{z}{z_R}\right). \tag{3.16}$$

In resonators this leads to differences in the resonant frequencies of the various modes of oscillation.

3.2 Finite mirrors resonators

A laser beam can be stored between two mirrors of finite size when the beam light itself is "resonant", which means the electromagnetic field is in a self-consistent configuration so that the electromagnetic field returns with exactly the same transverse pattern (but possibly with a reduced amplitude because of diffraction from mirror's edge) and an absolute phase shift after the round trip.

A structure with finite mirror apertures is intrinsically lossy and, unless energy is supplied to it continuously, the electromagnetic field in it will decay. So the starting point is to consider a mode of the resonator as a slowly decaying field configuration whose relative field distribution doesn't change with time. Solutions to this problem can be found be invoking the Fresnel-Kirchhoff formulation of Huygens' principle and assuming that the dimensions of the resonators are large compared to the wavelength and the resonating field is substantially transverse electromagnetic field mode (TEM) of the resonator.

Mathematically, the propagation integral is a linear operator equation: the resonant modes will be, if they exist, the *eigenvectors* for the round-trip operator given by the kernel $\tilde{K}$ as

$$\gamma_{mn}\tilde{E}(\mathbf{s}) \equiv \int\int \tilde{K}(\mathbf{s},\mathbf{s}_0)\tilde{E}(\mathbf{s}_0). \tag{3.17}$$

The function $\tilde{K}$ is commonly called the propagation kernel of simply "propagator". Any plane inside the resonator can be taken as reference and the exact form of resonator's propagator will depend on this choice. If the reference plane is chosen at an aperture (for example at the input mirror), and the only intervening element before the next aperture is free space, the propagator will be simply Huygens' integral for free space.

After a round trip, the transverse mode pattern has the same phase and amplitude variation, but it will be reduced in amplitude and shifted in absolute phase by the complex eigenvalue γ_{mn}. The transverse field, solution of the Eq. 3.17, will have a different field pattern $\tilde{E}(\mathbf{s}, z)$ at each transverse z plane within the resonator.

In a open-sided resonator with finite-diameter mirrors, as for a GW interferometer, some of the radiation will spread out after each round trip, and so the magnitudes of the transverse eigenvalues will therefore always be less than unity, i.e. $|\gamma_{mn}| < 1$. Thus, the diffraction loss of each TEM is

$$\mathcal{L}_{mn} = 1 - |\gamma_{mn}|^2 . \tag{3.18}$$

The lowest-loss eigenmode, i.e. the one with the largest value of $|\gamma_{mn}|$ will (normally) be the dominant mode in the cavity.

The Eq. 3.17 establish the mathematical peculiarities for the cavity resonant modes, which differ from the free space propagation modes. Since the round-trip propagation kernel $\tilde{K}(\mathbf{s},\mathbf{s}_0)$ for open-sided resonator is generally

found not to be a hermitian operator, the properties of orthogonality and completeness are in general lost. It cannot be rigorously proved that within a given resonator can be written in the form

$$\tilde{E}(\mathbf{s}) = (?) \sum_{mn} c_{mn} \tilde{E}_{mn}(\mathbf{s}). \tag{3.19}$$

3.2.1 Transverse eigenmodes for resonators with spherical mirrors

The existence of solutions for the integral equation Eq. 3.17 has been proved for resonators geometries such as two mirrors with parallel-plane and spherically curved surfaces. An analytical solution has also been found [27] in the case of *confocal resonator*, which are symmetric cavities with a spacing between the mirrors equal to their radius of curvature. Their electromagnetic field transverse distribution over any arbitrary plane orthogonal to the propagation axis can be approximatively expressed as the known Hermite-gaussian functions.

Since the surfaces of constant phase of the confocal resonator are spherical, it is apparent that the Hermite-gaussian eigenmodes set also represents the field distribution between two spherical reflectors of arbitrary spacing. This approximation is more valid as the Fresnel number $N \equiv a_1 a_2 / \lambda L$ goes to infinity, where a_1 and a_2 are the transverse dimensions of the two mirrors.

Thus, the problem of finding resonant modes for spherical cavities can be solved as follows: given two curved mirrors M_1 and M_2, with radii of curvature R_1 and R_2 and spacing L, we ask to find the gaussian beam that satisfies the resonance condition for the given resonator geometry. Using the equation 3.9 for $R(z)$ and imposing that the wavefront curvature must match the mirror curvature at each mirror, the resonant gaussian beam for a spherical cavity will have the waist spot size given by

$$w_0^2 = \frac{L\lambda}{\pi} \sqrt{\frac{g_1 g_2 (1 - g_1 g_2)}{(g_1 + g_2 - 2 g_1 g_2)^2}}, \tag{3.20}$$

and the spot sizes on the mirrors surfaces given by

$$w_1^2 = \frac{L\lambda}{\pi} \sqrt{\frac{g_2}{g_1(1 - g_1 g_2)}} \qquad \text{and} \qquad w_2^2 = \frac{L\lambda}{\pi} \sqrt{\frac{g_1}{g_2(1 - g_1 g_2)}}. \tag{3.21}$$

Here we introduced the "resonator g parameters" as $g_{1,2} \equiv 1 - L/R_{1,2}$. It is clear that we have a real solution, i.e. a stable resonator, only if the condition

$$0 \leq g_1 g_2 \leq 1 \tag{3.22}$$

is satisfied. If a gaussian beam is found resonant for a given (infinite) spherical resonator, then all its Hermite-gaussian (or Laguerre-gaussian) functions are eigenmodes for that cavity. However,the Hermite-gaussian or Laguerre-gaussian functions are a good approximation of a spherical cavity, as well as the Fresnel number goes to infinity. Hence, we can consider for almost all further discussions $TEM_{mn} = \psi_{mn}^{HG}$, for a rectangular symmetric resonator.

The frequency spacing between each transverse mode and the fundamental mode is function of the g parameters as follows:

$$\omega_{qmn} = \left[q + (n+m+1)\frac{\arccos(\pm\sqrt{g_1 g_2})}{\pi} \right] \frac{\pi c}{L} \qquad \text{(HG)}, \tag{3.23}$$

$$\omega_{qpl} = \left[q + (2p+l+1)\frac{\arccos(\pm\sqrt{g_1 g_2})}{\pi} \right] \frac{\pi c}{L} \qquad \text{(LG)}. \tag{3.24}$$

3.3 Optical response of a Fabry-Perot cavity

In this section, we want to investigate how a monochromatic electromagnetic field is stored in a Fabry-Perot resonator.

The first issue about such an interferometer is its axial resonance condition. Assuming that the input field is perfectly mode matched, that means the transverse field propagation law doesn't change inside and outside the cavity, let consider the input field as a generic ψ_{in} and r_i, t_i and $\mathcal{L}$ are the field reflectivity, transmittivity and losses for each mirror [see Fig. 3.2].

The equations for the fields are:

$$\begin{cases} \psi_1 = t_1 \psi_{in} - r_1 \psi_4 \\ \psi_{tr} = t_2 \psi_1 e^{-jkL} \\ \psi_3 = -r_2 \psi_2 \\ \psi_{ref} = -r_1 \psi_{in} + t_1 \psi_4 \end{cases}$$

The resulting fields are:

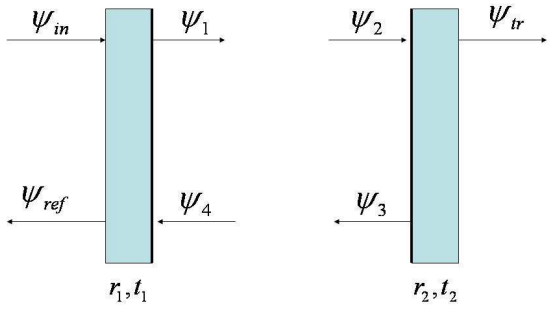

Figure 3.2: Electromagnetic fields in a Fabry-Perot resonator

$$\psi_{tr} = \frac{t_1 t_2 e^{jkL}}{1 - r_1 r_2 e^{2jkL}} \psi_{in}, \tag{3.25}$$

$$\psi_1 = \frac{t_1 e^{jkL}}{1 - r_1 r_2 e^{2jkL}} \psi_{in}, \tag{3.26}$$

$$\psi_{ref} = \left(-r_1 + \frac{t_1^2 r_2 e^{jkL}}{1 - r_1 r_2 e^{2jkL}} \right) \psi_{in}. \tag{3.27}$$

From ψ_1 it is possible to calculate the power stored inside the cavity as function of the incoming power as

$$\begin{aligned} P &= |\psi_1|^2 = P_{in} \frac{t_1^2}{(1 - r_1 r_2)^2 + 4 r_1 r_2 \sin^2(kL)} \\ &= \frac{t_1^2}{(1 - r_1 r_2)^2} \frac{P_{in}}{1 + \dfrac{4 r_1 r_2}{(1 - r_1 r_2)^2} \sin^2(kL)} = g^2 P_{in} \mathcal{A}(\phi), \end{aligned} \tag{3.28}$$

introducing the Fabry-Perot gain g and the Airy function $\mathcal{A}(\phi)$. The maximum stored (and thus transmitted) power corresponds to the peak of the Airy function, i.e. when the detuning phase $\phi \equiv kL = n\pi$.

The detuning phase can be changed to match the resonance condition both by varying the length of the cavity and/or the frequency of the input

light. If L is fixed, the resonance condition is achieved when the incoming beam has a frequency $\nu = n\frac{c}{2L} \equiv n\Delta\nu_{FSR}$, where the spacing between two successive axial resonances has been called the *free spectral range* (FSR) of the cavity. In the case of our 7.3 m cavity, the FSR is roughly 20.5 MHz. For a frequency-stabilized electromagnetic field, if we express the actual cavity length as $L = L_0 + \xi$, in which L_0 is an integer number of half wavelength and ξ a length offset, this offset has to be $\xi = n\frac{\lambda}{2}$ to match a resonance peak.

So varying the cavity length one covers a FSR every $\lambda/2$. In the case of incoming plane waves for a resonator formed by two facing infinite flat mirrors, there are no resonance inside a FSR. For spherical cavities small changes of the length (or the frequency) can yield a higher order TEM mode resonant. Thus, for a not-perfectly mode matched FP cavity, its resonant frequency spectrum can be scanned sweeping over few FSRs of the cavity, as shown in Fig 3.3.

Each line of the cavity spectrum corresponds to a TEM mode and has a peculiar width due to the proper width of the Airy function and the characteristic losses of its specific TEM mode. If we consider the ideal case of no losses on the system, it is possible to extract from the formula of the Airy function the frequency interval with amplitude more than 1/2:

$$\begin{aligned} \mathcal{A}(\phi) &= \frac{1}{1 + \dfrac{4r_1r_2}{(1-r_1r_2)^2}\sin^2(\phi)} \\ &\simeq \frac{1}{1 + \dfrac{4r_1r_2}{(1-r_1r_2)^2}\pi\dfrac{\nu}{\Delta\nu_{FSR}}} = \frac{1}{1 + \left(2\mathcal{F}\dfrac{\nu}{\Delta\nu_{FSR}}\right)^2}, \end{aligned} \tag{3.29}$$

where $\mathcal{F}$ has been called the *finesse* of the cavity with the following definition

$$\mathcal{F} = \frac{\pi\sqrt{r_1r_2}}{1 - r_1r_2}. \tag{3.30}$$

Finally the values of ν such that the power amplitude is half its maximum are

$$\nu = \pm\frac{\Delta\nu_{FSR}}{2\mathcal{F}} \tag{3.31}$$

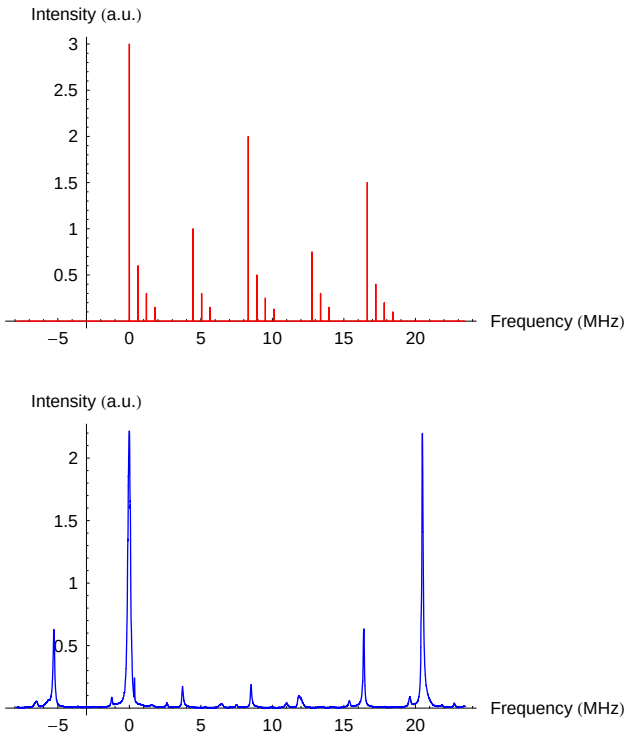

Figure 3.3: Fabry-Perot transverse modes spectra. On the top, theoretical spectrum for a 7.32 m long resonator with $g_1 = 1$ and $g_2 = 0.085$. On the bottom, a length sweeping intensity map taken with a spherical mirror whose nominal radius of curvature of 8 meters

and the *full width half maximum* (FWHM) of the resonance is

$$FWHM = \frac{\Delta\nu_{FSR}}{\mathcal{F}}. \tag{3.32}$$

The cavity finesse and its FSR are an alternative set of parameters equivalent to r_1, r_2 and L for a Fabry-Perot resonator. The first is related to the width of each resonance and the gain of the resonator as follows: $g^2 \simeq 2\mathcal{F}/\pi$. Thus, the finesse contains only a photometric information about mirrors. Whereas, the FSR contains a geometrical (longitudinal) information about the cavity. We can write even the Eq. 3.23 and 3.24 with respect to the cavity FSR as follows

$$\omega_{qmn} = \left[q + (n+m+1)\frac{\arccos(\pm\sqrt{g_1 g_2})}{\pi}\right] 2\pi\Delta\nu_{FSR} \qquad \text{(HG)}, \tag{3.33}$$

$$\omega_{qpl} = \left[q + (2p+l+1)\frac{\arccos(\pm\sqrt{g_1 g_2})}{\pi}\right] 2\pi\Delta\nu_{FSR} \qquad \text{(LG)}. \tag{3.34}$$

3.3.1 Optical cavity locking

Due to environmental motions of the mirrors, a long Fabry-Perot resonator wouldn't be able to keep the resonance condition by itself, even if the incoming laser beam had a perfectly stabilized frequency. The aim of the "lock" is to maintain the distance between the mirrors constant with respect to the input field wavelength fluctuations and at the desired resonance position. Thus, the lock acquisition consists of generate a length or frequency (or both) error signal to feedback to the system and automatically maintain the resonator in resonance.

One of the simplest and most widely used lock technique is the *side-lock* technique. Its work principle consists on acquiring the cavity transmission signal by means of a photodiode and to compare it with a reference signal, which can be a voltage offset or an analogous signal generated by part of the input light[1]. The difference between the transmitted signal and its reference is used as error signal to produce the feedback on the mirrors displacement or the laser frequency. Obviously the control will be tighter where the sensitivity

[1]for example, it can be extracted through a pick-off along the input beam path

to the detuning phase changes is larger, and null where $dV_{tr}/d\phi = 0$. In particular, this technique allows to lock on the side of the Airy curve and it has the disadvantage to not permit the lock on the peak of a resonance.

Another disadvantage of the side-locking is that amplitude fluctuations in the light source are all seen by the cavity and these are more important when the phase sensitivity is higher. This problem can be recovered by using part of the input intensity signal as reference, which is affected by the same fluctuations.

A technique used to lock on the peak of a resonance is the so-called *dither-lock* technique. It usually consists of applying a small modulation to the cavity length. The modulation ΔL must be compared to the cavity FSR. In this case we can write $L(t) = L_0 + \xi + \Delta L \cos(\omega_d t)$. In proximity of a resonant peak, the transmitted field will be

$$\begin{aligned}
\psi_t &= \frac{t_1 t_2 e^{j\frac{2\pi}{\lambda}(L_0+\xi+\Delta L\cos(\omega_d t))}}{1 - r_1 r_2 e^{2j\frac{2\pi}{\lambda}(L_0+\xi+\Delta L\cos(\omega_d t))}} \\
&\simeq -t_1 t_2 e^{j\frac{2\pi}{\lambda}(\xi+\Delta L\cos(\omega_d t))}\left[1 + r_1 r_2 + j r_1 r_2 \frac{4\pi}{\lambda}(\xi + \Delta L\cos(\omega_d t))\right] \\
P_t = |\psi_t|^2 &= (t_1 t_2)^2 \left[(1 + r_1 r_2)^2 + \left(\frac{4\pi}{\lambda} r_1 r_2\right)^2 (\xi + \Delta L\cos(\omega_d t))\right]. \quad (3.35)
\end{aligned}$$

The transmission signal component with frequency ω_d,

$$I_{mod} = (t_1 t_2)^2 \left(\frac{4\pi}{\lambda} r_1 r_2\right)(2\xi \Delta L \cos(\omega_d t)) \quad (3.36)$$

can be extracted by demodulating it from the transmitted beam signal using a mixer which multiplies the signal with the same local oscillator that provide the cavity length modulation. the demodulated signal is than integrated over a limited period to eliminate the DC component. This operation is usually performed by means of a lock-in amplifier. The demodulated signal a good error signal to lock the cavity because since it is zero at the peak of each resonance and is sensitive to sign of ξ.

The dithering technique allows to lock on the peak of the Airy curve. The disadvantage of dithering is that it is implemented with piezoelectric of magnetic coil actuators. This means that it has limited capabilities ($\approx$10

kHz) to shift the demodulation away from frequencies in which the laser is dominated by amplitude noise.

Furthermore, both peak and side-locking techniques have a limited recovery range, since the resonance peaks are very narrow for high finesse cavities. All this problems could be avoided by a direct modulation of the light that can bring the work frequency at many MHz, but expensive electro-optic components must be used.

3.3.2 Optical Cavity matching

The optical response of a Fabry-Perot resonator will depend on the matching between the incident laser beam and the cavity itself.

The maximum gain is achieved when the input laser beam couples completely to the fundamental (longitudinal) spatial mode of the cavity and not at all to the higher-order spatial modes. It happens when the input beam axis is perfectly aligned to the cavity optical axis, and when the beam propagation parameters of these two, as the beam waist and its position for a gaussian beam, are matched.

The problem of cavity matching and alignment was widely treated by Anderson [28] in the case of spherical mirrors. The starting point is the identification of the cavity optical axis, which correspond to the line intersecting the center of curvatures of the two mirrors. It defines a set of eigenmodes which are generally the Hermite-gaussian or Laguerre-gaussian functions. Any input beam can be expanded and expressed as a linear combination of these eigenmodes [29]. A generic mismatching between the incident field and the cavity fundamental mode can be one of these four kinds:

1. translation of a length a between the input beam axis and the cavity axis;

2. a tilt angle θ between the input beam axis and the cavity axis;

3. waist sizes mismatch;

4. difference b between longitudinal positions of the two waists.

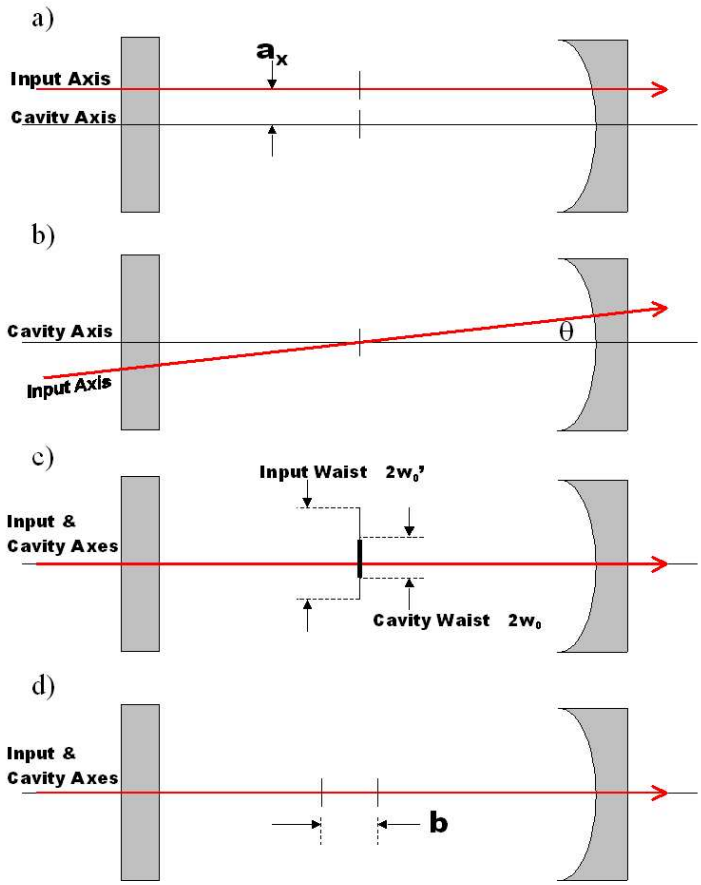

Figure 3.4: Misalignments for a spherical cavity.

It is possible to show that the input beam couples with the first excited transverse mode, for example the TEM_{01}, for small values of the misalignment parameters a and θ, while a "mode mismatch" (waist mismatch) couples a gaussian TEM_{00} to the second order transverse mode as the TEM_{20} Hermite-gaussian or the TEM_{10} Laguerre-gaussian.

Degree of freedom	Parameter	Coupling coefficient	Mode
Transverse position	a	a/w_0	$U_1(\mu)$
Angular tilt	θ	θ/θ_∞	$U_1(\mu)$
Waist size	$w_0^{'}$	$w_0^{'}/w_0 - 1$	$V_1(r)$
Waist position	b	$b/2z_R$	$V_1(r)$

Table 3.1: Couplings due to misalignments of an input beam with respect to the cavity fundamental mode. Here we have used $\psi_{mn}(x,y) = U_m(x)U_n(y)$ or the symbol V_p for the radial component of the Laguerre-gaussian functions.

The square of the coupling coefficients, shown in the Tab. 3.1, corresponds to the amount of power not injected in the fundamental mode for small misalignments. They were calculated assuming that the input beam can be considered as the cavity fundamental mode with an "off-axis" argument and then expanded in a power series with respect to the misalignment parameter. It is possible to measure experimentally misalignment coefficients by first identifying the individual modes and then sweeping through the cavity spectrum by more than a FSR. Maximizing the peak of interest in the frequencies spectrum is a useful tool in order to find the best possible alignment.

Since feeding a perfect gaussian field pattern doesn't guarantee the full power gain performance for a Fabry-Perot resonator, suitable mode matching techniques have to be used. The easiest solution to match the laser input beam is a thin lens, but other more complex systems can be used.

A thin lens transforms the phase front of laser beams in exactly the same way as those of spherical waves. As the diameter of a beam is the same on the two surfaces of a thin lens, the $\tilde{q}$ parameters of the incoming and outgoing beams are related by [25]

$$\frac{1}{\tilde{q}_2} = \frac{1}{\tilde{q}_1} - \frac{1}{f}, \tag{3.37}$$

where the $\tilde{q}$'s are measured at the lens. The propagation of paraxial rays

through a more complex optical structure can be analyzed using the $ABCD$ transfer matrix. The $\tilde{q}$ parameter of the output beam can be calculated from

$$\tilde{q}_2 = \frac{A\tilde{q}_1 + B}{C\tilde{q}_1 + D}. \tag{3.38}$$

The problem of mode matching a spherical cavity with a generic laser oscillator, tuned to its fundamental mode can be analyzed using the single thin lens formula [Eq. 3.37]. the location and the sizes w_1 and w_2 of the two waist of the two beams to be transformed into each other are supposed to be known. The mode match is then performed choosing a lens of a focal length larger than a characteristic length f_0, established by the two waist sizes as

$$f_0 = \frac{\pi w_1 w_2}{\lambda}, \tag{3.39}$$

and adjusting the distances of the beam waists d_1 and d_2 from the lens according to [30]:

$$\begin{cases} d_1 = f \pm \dfrac{w_1}{w_2}\sqrt{f^2 - f_0^2} \\ \\ d_2 = f \pm \dfrac{w_2}{w_1}\sqrt{f^2 - f_0^2} \end{cases} \tag{3.40}$$

These two relations can be used with either both plus signs or both minus signs for matching.

We can generalize the method above by using $ABCD$ matrix formalism and solve the Eq. 3.38. The system of equations to be solved is

$$\begin{cases} -Cf_0^2 = B \\ \\ Dw_2^2 = Aw_1^2 \end{cases} \tag{3.41}$$

Chapter 4

The Mesa beam

4.1 Supergaussian transverse modes

The fundamental gaussian TEM_{00} has great flexibility and utility in many applications, and additionally it has a easy and attractive mathematical form. Nevertheless, many laser applications require a different intensity profile: since in a cylindrical volume with a diameter $d = 3w$ just a quarter of it is filled by a gaussian intensity distribution, a gaussian beam is not appropriate for high power applications.

One set of potential beam profile that satisfy the request of a flat-top, more uniform transverse power distributions, is given by the *supergaussian* functions, with analytical form [Fig.4.1]

$$\psi_{sg}(r) = \exp\left[-\left(\frac{r}{w_0}\right)^{2n}\right]. \tag{4.1}$$

Such a field pattern can be obtained shaping a gaussian beam with a diffractive optic and use a refractive lens to produce a focused flat top intensity. At the focus of the lens, the Fourier transform of the input beam intensity pattern is then produced [31].

It was shown also that certain optical resonators formed by two facing graded phase mirrors - i.e. aspherical mirrors - can have a fundamental mode with supergaussian features [32],[33],[34],[35]. The mirror profile, in this case, was designed in such a way to match the phase wavefront for a prescribed intensity profile.

A different analytical approach to design flattened beam was proposed

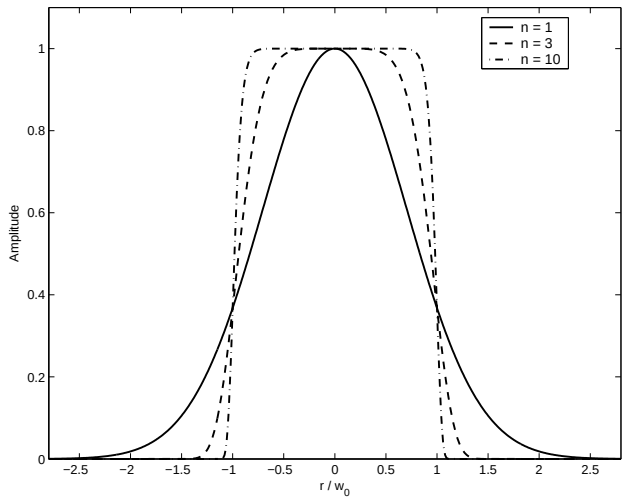

Figure 4.1: Supergaussian beam profiles with index n=1(ordinary gaussian beam), 3 and 10

by Gori [36]: the flat top beam can be obtained as a sum of Laguerre Gauss modes in the cylindrical coordinate system. The main advantage of such transverse field distribution is that the field that they produce upon propagation can be evaluated in a simple way without introducing any approximation except, of course, that the paraxial regime is assumed to hold.

Tovar [37] has proposed a new class of beams, called *multi-Gaussian beams*, that can reproduce the flattness of a super-gaussian transverse field. They consists of a small sum (or an integral over a disc) of finite-width gaussian beams side by side with the same width, phase curvature and absolute phase. Unlike the flattened Gaussian beams, each of the multi-Gaussian beam components can be traced individually without resort to further series expansion. Hence, this approach has an analytical form more desirable in order to know the beam diffraction characteristics.

In the case of gravitational wave interferometers, their sensitivity requirements need very small diffraction losses ($\approx$ 10 ppm per bounce) in their arms. This excludes ordinary refractive techniques to flatten the resonant beam shape in their Fabry-Perot arms and so decrease significantly test mass thermal noise. Furthermore, beam propagation must be exactly known in order to characterize interferometer performances. These issues are essentially the main motivations that induced Thorne et al. [38] to introduce a new family

of flat top beams and the "Mexican hat" mirrors that support them which could be optimal for reduction of mirror thermal noises: the *Mesa beams*.

4.2 Mesa Fields

In this paragraph it will be described how the Mesa beam has been constructed to reduce test mass thermal noise and match all the requirements for its possible application in a GWID.

As described in [38],[39], the Mesa beam needs to have an intensity distribution that is nearly flat across most of the light beam impinging on the surface of both the cavity mirrors, and that then falls as rapidly as possible, satisfying diffraction constraints, at the beam's edges. As discussed in the previous section, it is possible to design a flatter beam by overlapping gaussian functions: since for an optical cavity of length L the gaussian beam which has the least increasing radius, and so the least diffraction loss per bounce, has a waist size $w_0 = b = \sqrt{L/k}$, the optimal choice for a multi-Gaussian beam is the so-called *minimal Gaussian*. Starting from the half of the symmetric cavity, the analytical form after $L/2$ for the minimal Gaussian is

$$\psi_{minGauss}(r) = \exp\left[\frac{-r^2(1+i)}{2b^2}\right]. \tag{4.2}$$

Thus, to produce the Mesa mode pattern, the above minimal-gaussian fields are superposed over a radius $r = D$, so to obtain the unnormalized eigenmode (for an ideal no-loss optical system)

$$\begin{aligned}\psi_{mesa}(r) &= \int_{r'<D} \mathrm{d}^2\vec{r}\,' e^{\frac{-(\vec{r}-\vec{r}\,')^2(1+i)}{2b^2}} \\ &= 2\pi \int_0^D e^{\frac{-(r^2+r'^2)(1+i)}{2b^2}} I_0\left[\frac{rr'(1+i)}{b^2}\right] r'\,dr', \end{aligned} \tag{4.3}$$

where I_0 is the modified Bessel function of order zero. The above definition of the Mesa beam can be applied to every custom resonator size. Once the mirror size is set, diffraction losses requirements will determine the size of the integration disc D. The diffraction losses for each reflection of a cavity mode off a mirror are given, approximatively, by the *clipping approximation*

$$\mathcal{L}_{clip} = \frac{\int_R^\infty |\psi_{mesa}(r)|^2 \, 2\pi r dr}{\int_0^\infty |\psi_{mesa}(r)|^2 \, 2\pi r dr}. \tag{4.4}$$

In actuality, boundary effects due to finite size mirrors affect the field distribution causing the true diffraction losses to differ lightly from the clipping approximation value. Starting from the baseline design for advanced LIGO which set the actual diffraction losses to $\mathcal{L}_0 = 10$ ppm, the proposed fiducial Mesa beam has a radius $D = 4b$, and diffraction losses modestly larger [38]. In Fig. 4.2 a profile of the normalized Mesa beam power is plotted together an ordinary gaussian with same diffraction losses.

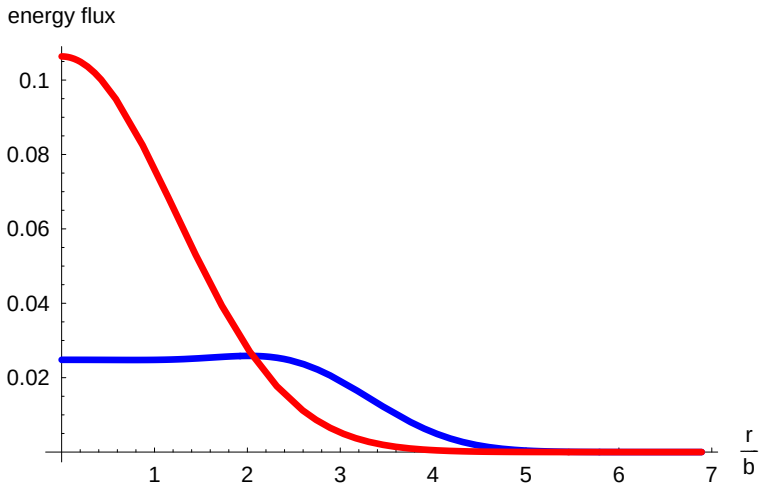

Figure 4.2: Comparison between the power distribution of the gaussian mode with $r_0 = 1.73b$ for advanced LIGO nearly-flat configuration, and the Mesa beam power distribution with $D = 4b$

4.3 "Mexican hat" Fabry-Perot cavity and resonant eigenmodes

The Fabry-Perot cavity supporting the electromagnetic field expressed in Eq. 4.3 can be built reshaping the mirrors in such a way that when the beam hits a reflective surface that matches its wavefront, the sign of its phase

$$\Phi_{WF} = \Phi[\psi_{mesa}(r)] - \Phi[\psi_{mesa}(0)] \tag{4.5}$$

is flipped so that when it is propagated back it has the same shape (this is a good approximation for finite mirrors if the diffraction losses are small). The resulting height distribution as a function of radius r is given by

$$h_{MH}(r) = \frac{\Phi[\psi_{mesa}(r)] - \Phi[\psi_{mesa}(0)]}{k}. \tag{4.6}$$

Since this new mirror shape, as shown in Fig 4.3, has a shallow bump in the middle and a flaring outer edges, this resemblance to a Mexican hat (sombrero) gives the name to the mirror.

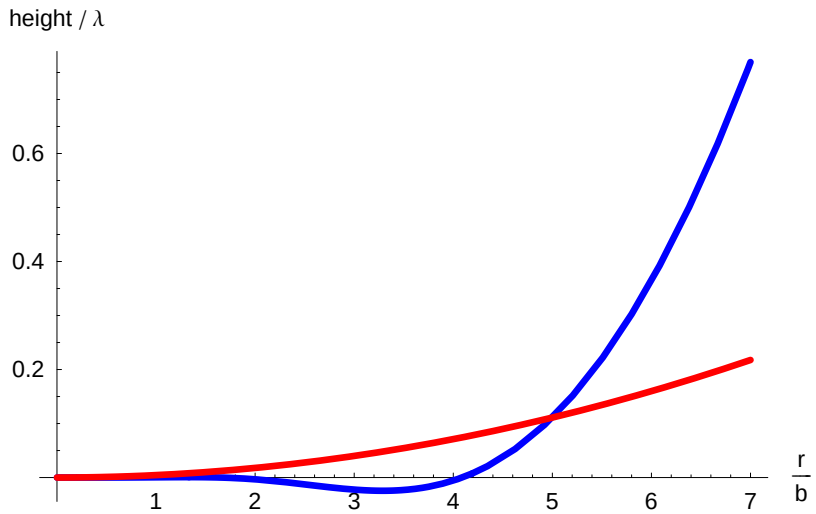

Figure 4.3: Nearly-flat mirrors: spherical mirror supporting gaussian beam (red), and Mexican hat supporting the equivalent Mesa beam

Since Φ_{WF} is cylindrically symmetric, we expect that the resulting symmetry of the MH mirror, is reflected in the MH cavity eigenmodes. It is possible to solve the Eq. 3.17 for a resonator with mirror profile as in Eq. 4.6. The resulting kernel for a symmetric cavity (in paraxial approximation) is [40]:

$$\tilde{K}(\vec{r},\vec{r}^{\,\prime}) = \frac{ik}{2\pi L}\exp\left[-ikL + ikh_{MH}(r) - \frac{ik}{2L}\left|\vec{r}-\vec{r}^{\,\prime}\right|^2 + ikh_{MH}(r^{\prime})\right]. \tag{4.7}$$

As long as the cavity mirrors have cylindrical shapes, it is possible to separate the radial from the azimuthal degree of freedom. Defining the phasor amplitude as

$$\tilde{E}(r,\varphi) = R(r)e^{-il\varphi}, \qquad l = \text{integer}, \tag{4.8}$$

the eigenequation Eq. 3.17 can be numerically solved as a series of one-dimensional integral equation, one for each l. After the appropriate discretization of the eigenmodes integral equation, the resulting vectors R_{pl} are approximated by the matrix eigenequation[1]

$$\gamma_{pl} R_{pl}(r_i) = \mathbf{K}^l R_{pl}(r_i). \tag{4.9}$$

Some of the obtained R_{pl} are shown in Fig 4.4 and compared with the analougus Laguerre-gaussian function. A first qualitative analysis of these graphs emphasizes how the central flatter part of the MH is reflected in the TEM_{01} and TEM_{10}, while the steep rim in the outer part contracts the power distribution of the higher modes. This makes the higher order mesa beams slightly different with respect the gaussian counterpart.

The effect of these differences requires a detailed analysis of the transverse modes distribution in the cavity spectrum. Since for a generic Fabry-Perot resonator, as the MH cavity, an analytical formula for its modes does not exist, one has to extrapolate it from the numerical results for the eigenvalues of each mode.

The found eigenmodes satisfy the resonance condition that states (for the round trip problem)

$$Arg\left[\gamma_{pl} e^{2jkL}\right] = 0, \tag{4.10}$$

that means the light in a given state interferes constructively with itself. Then, the condition for the beam frequency is translated into

$$2\pi n = 2L\frac{\omega_{pl}}{c} + Arg(\gamma_{pl}) = \frac{2\pi\nu_{pl}}{\Delta\nu_{FSR}} + Arg(\gamma_{pl}) \tag{4.11}$$

So each mode resonate at a certain frequency and all the other frequencies separated from that one by a integer numbers of FSRs. Thus we can extract the frequency separation between each eigenmode as

[1] only here the eigenvalue γ_{pl} is referred to input-end mirrors trip

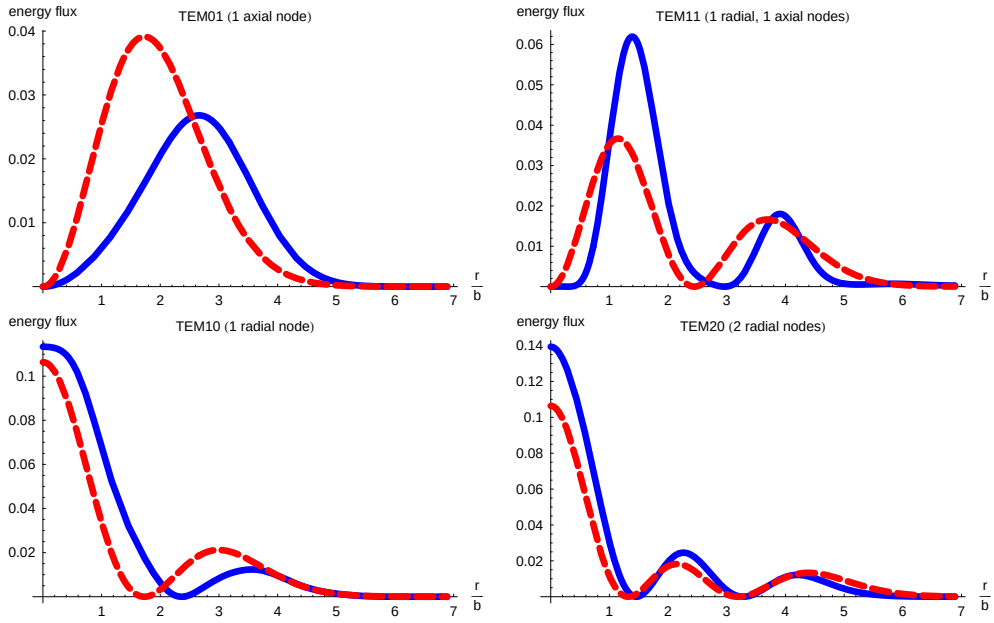

Figure 4.4: Comparison between normalized power distributions of eigenfuctions for a Mexican hat cavity (blue solid line) and the equivalent spherical (dashed red line) with same diffraction losses for the fundamental mode.

$$\Delta\nu_{ij} = \frac{Arg(\gamma_i) - Arg(\gamma_j)}{2\pi}\Delta\nu_{FSR}. \tag{4.12}$$

As anticipated before, for the mesa beams the cavity spectrum must be obtained numerically. The results for LIGO Fabry-Perot cavities [23] show that the eigenmodes are not distributed regularly within each FSR and from the comparison with the distribution of the eigenmodes for the gaussian-beam cavity, it is expected the mesa beam cavity to be slightly more sensitive to perturbation (as misalignments, mirrors imperfections) than the Gaussian-beam counterpart.

The procedure described above, consisting in a superposition of gaussians with parallel optical axes, yields supporting mirrors that are "nearly flat" (FM) and a beam propagation inside a cylinder generated by these parallel lines. This optical configuration is demonstrated to produce tilt instabilities for high power Fabry-Perot cavities as advanced LIGO [41],[42], while a "nearly concentric" cavity weakens this problem. It is possible to produce a nearly-concentric Mesa beam (CM) [43], with the same spot size on the mirrors surface, by overlapping minimal Gaussians whose optic axes all pass through the center of the cavity, and are distributed uniformly inside a cone with angular radius $\Theta = D/(L/2)$. It will be supported by a nearly-concentric MH mirror, which has a profile corrected from the sphere with radius of curvature equal to half of the cavity length.

From the manufacturing point of view, it is possible to obtain these two mirrors starting from a plane mirror (FM configuration) or a concentric sphere (CM configuration): in the first case the profile shown in Fig. 4.3 has to be added to the plane surface; in the second one, the MH profile has to be subtracted. This is due to a more general duality relation [44] that involves nearly-flat and nearly-concentric mirrors: it tell us that both power distributions and frequency spacing for the dual cavities TEMs are the same.

In order to make resonant a common laser beam, which is usually tuned to a gaussian fundamental mode, in to a MH cavity one way is use a mode-cleaning cavity before it to convert a gaussian beam into a Mesa beam, or to drive the system directly by a gaussian beam.

D'Ambrosio [39] dedicated an analytical study to find the optimal coupling between the cavity resonant mode and the driving field. This method is based on maximizing the overlap of these two field, expressed as

$$|\mathcal{C}|^2 = \frac{\left| \int \int r dr d\theta \psi_G^*(r) \psi_0(r) \right|^2}{\int |\psi_0(r)|^2 \, 2\pi r dr}, \tag{4.13}$$

where ψ_0 is the mesa field at the waist position, while the driving field ψ_G is normalized as

$$\psi_G(r) = \sqrt{\frac{2}{\pi w_G^2}} \; e^{-\left(\frac{1}{w_G^2} + \frac{jk}{2R_G}\right) r^2}. \tag{4.14}$$

If the mesa beam radius is chosen $D = 4b$, the overlap integral has its maximum value for zero curvature, that is, $1/R_G = 0$, and for $w_G = 3.62b$, while $|\mathcal{C}|^2 = 0.940$. This means that 94.0 per cent of the gaussian driving-beam light will enter the MH cavity, and the remnant 6.0 per cent will be rejected.

4.4 Effects of misalignment for a Mesa beam

In analogy with the spherical mirrors case, it is important to quantify the impact of misalignments for nearly-flat MH mirrors on the Mesa beam.

A perturbation approach to misalignments, as for spherical mirror, can be done even for the Mesa beam. Since the MH has a nonspherical shape, any misalignments involve a change of the symmetry of the resonant beam: not only there is a new axis of the cavity but the phase profile sensed by the beam is different. For spherical mirrors is not the case because any point on its surface has the same curvature. Then, the new modes of the MH cavity will have a different intensity distribution and phase wavefront.

Let's call $u_n(\vec{r})$ the unit-norm eigenfunction of the MH resonator. When a small mirror tilt is applied to the unperturbed cavity, its fundamental mode gets changed to

$$u_0^{'}(\vec{r}) = \left(1 - \frac{\alpha_1^2}{2}\right) u_0(r) + \alpha_1 u_1(\vec{r}) + \alpha_2 u_2(\vec{r}). \tag{4.15}$$

Here α_n are the mode-mixing coefficients that scale as $(\theta_{tilt})^n$. The first excited component will be odd in the axis orthogonal to the tilt rotation axis. Second order perturbations have to be taken into account, and they

will bring the information of the symmetry breaking, showing some enhanced power in the tilt rotation axis [[39] see Fig.16].

Another problem related to beam deformation could be due to the effects of mirror imperfections. Since the central bump has an height of about 27 nm, it is possible to imagine that a required precision in the bump deposition on a plane substrate of at least 2 nm can be easily missed in many points of the mirror, or mirror manipulation can yield surface distortions due to thermal or mechanical effects. This issue will be as much critic as the dimensions of the mirror are small.

The problem of mirror imperfection has been analyzed [39], and it shows that an odd contribution is provided to the field distribution along the mirror direction where the symmetry is broken.

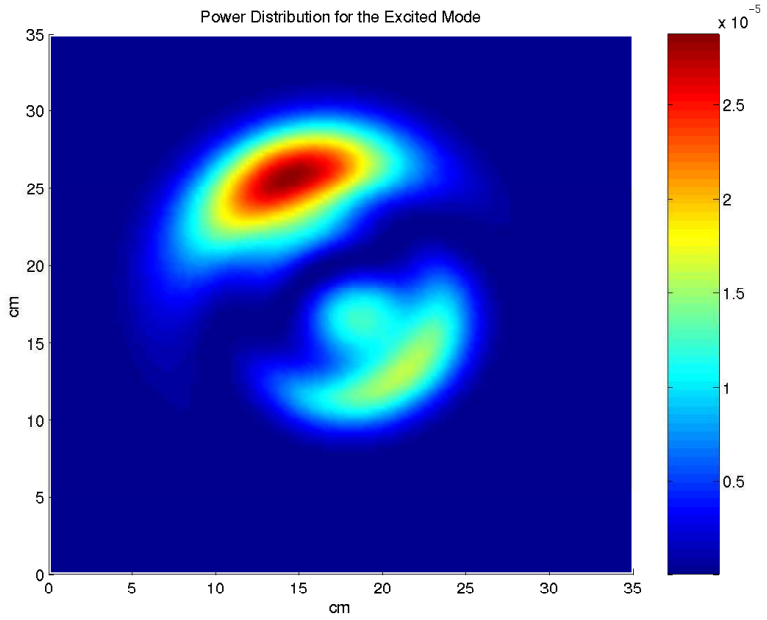

Figure 4.5: Residual power distribution for the funadmental Mesa beam mode simulated by FFT code. The lower peak is placed above the central deformation of the pseudo-LIGO set mass map, and its shape resemble the shape of this bump [45].

Chapter 5

Experimental setup

In this chapter the experimental setup of the Mesa beam cavity prototype is presented. It is possible to divide the experiment into four parts:

- **Input/Output optics bench**, where the injection laser beam light is prepared to be fed into the Fabry-Perot resonator and the transmitted beam is acquired in order to be subsequently processed.

- **The Fabry-Perot cavity**: here one can distinguish between the mechanical structure which supports the mirrors, and the optics themselves. It operated with either spherical optics or a custom MH mirror.

- **The control electronics**, which consist of the servo loop electronics needed to lock the cavity on its resonances, and the DC driver circuit designed and assembled to permit nano-adjustments of the cavity alignment.

- **The profile readout bench**, placed on the opposite end of the cavity tank with respect to the input bench, where a high resolution CCD camera acquires the beam intensity distribution.

The above setup has been implemented, with minimal differences, for both spherical and MH optical configurations. The first tests with spherical optics were very useful in order to understand the limits of the experimentnt and gain confidence with beam profile study.

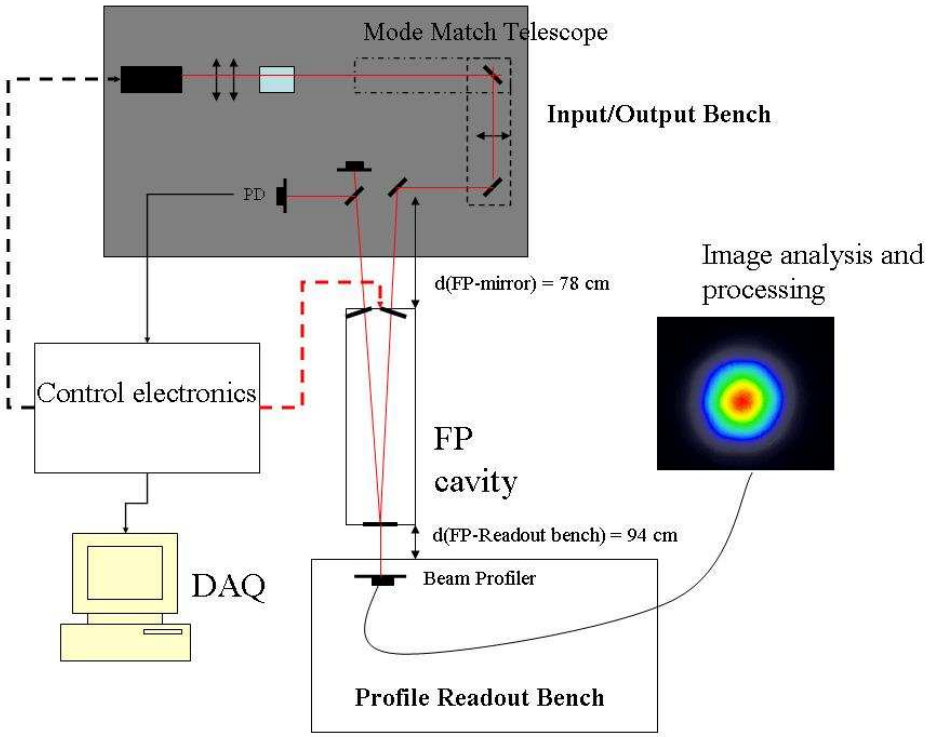

Figure 5.1: Overall view of the Mesa beam cavity prototype experimental setup

5.1 Input optics: layout and characterization

The initial input layout consisted of a laser oscillator, providing our input beam, two cylindrical lenses to reduce beam astigmatism, a Faraday rotator to protect the laser from light reflected from the cavity, three folding mirrors and one lens to mode match and align the input beam to the cavity.

As has been detailed in previous chapters, one important issue to be taken into account when one operates an optical resonator is the input beam. In perfect analogy with GWIDs, a laser light beam of wavelength $\lambda = 1064$nm is provided by a monolithic laser-diode-pumped Nd:YAG nonplanar ring oscillator. It is assembled in a Mephisto laser system (model name: "Mephisto 800"), which provides a laser power of about 800 mW. The laser is electronically controlled to have a low noise diode laser's injection current, a stable crystal temperature and a servo system to reduce intensity fluctuations. This noise eater essentially feeds back intensity fluctuations to the pump laser diode.

Such a laser system ensures a good beam stability in both frequency (1 MHz/min [46]) and intensity. It is possible to modulate the laser frequency by modulating the injection current. This is due to the fact that pump power variations are an important noise source for frequency fluctuations of this particular laser oscillator [47]. In fact, pump power modulation leads to a modulation of the deposited thermal energy in the amplification medium. This thermal modulation changes the index of refraction of the material as well as the length of the crystal; both phenomena result in a change of the optical path length in the Nd:YAG material. Hence these path-length modulations yield a frequency modulation of the laser.

It is possible to sweep this current modulation to feed back the servo error signal or to sweep the cavity spectrum in order to find the best alignment of the cavity itself.

The emitted laser radiation has a diffraction limited beam quality with a nominal waist size $w_0^{laser} = D_0/2 = 180\mu$m [46], where D_0 is the the total width of the beam which is automatically provided by any laser beam analyzer. $D(z)$ is defined as the distance between two points where the power intensity is $1/e^2 = 13.5$ % of the peak intensity amplitude.

I measured the actual beam profile in order to find: the laser waist size and location; what the beam profile looks like; and how gaussian it actually

is. To this end, a slit scanning beam profiler was employed (model name: Photon' "BeamScan"). This was useful because of its ability to accept fairly high powered beams, so I could measure the beam profile directly. The profiler provides beam diameters along two orthogonal axes with a space resolution, Δs, which depends on the working frequency it is used to rotate the slits. At f = 10 Hz, $\Delta s = 14.142\mu$m.

Fig. 5.2 shows x and y profiles collected at a distance of 995mm from the laser aperture along with gaussian fits. Measurements were performed at various distances to find the position of the waist. No adaptive optics were used, with just an iris close to the aperture in order to block the laser pump light, which is spatially separated from the Nd:Yag beam, mostly. The results are shown in the following table:

Parameter	Value	CI	Unit
D_{0x}	0.318	$\{0.313, 0.322\}$	mm
D_{0y}	0.356	$\{0.350, 0.361\}$	mm
z_{0x}	-164	$\{-178, -150\}$	mm
z_{0y}	-205	$\{-221, -189\}$	mm
Ellipticity	1.14		

Table 5.1: Results of the nonlinear regression for the laser beam waists in the x and y axes. The distances are taken from the laser aperture.

Qualitatively, the laser beam emitted by the laser system is a good TEM_{00} but shows both some deviation from the ideal profile and some astigmatism. In order to reduce the latter, I used two orthogonally oriented plano-convex cylindrical lenses with f=200mm and manually adjusted their position and measured the beam ellipticity in different points until the ellipticity was minimized.

Once a definitive positioning of the two lenses was established, the M^2 factor of the beam was measured. Its value gives a measure of "how many times diffraction limited" the real beam is in each transverse direction [48]. Its definition comes from the actual beam propagation law

$$\Theta_\infty = M^2 \frac{\lambda}{\pi w_0}, \tag{5.1}$$

where the actual beam propagation parameters have been defined as $W_0 = Mw_0$ and $\Theta_\infty = M\theta_\infty$. So, since $M^2 = 1$ quantifies how much a perfect

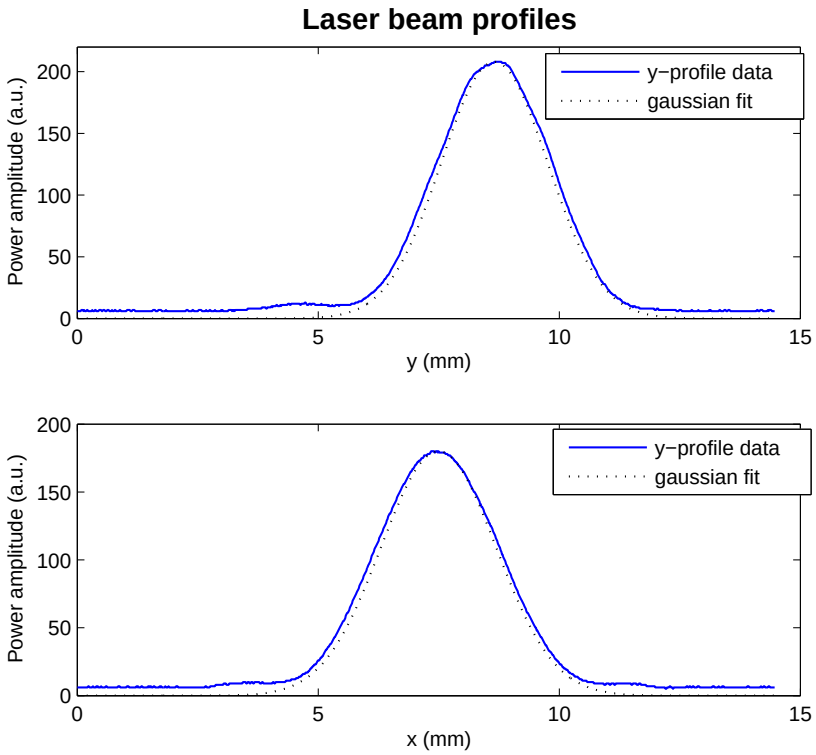

Figure 5.2: Two-dimensional profiles of the injection beam grabbed with a *BeamScan* profiler at a distance $z_1 = 995$mm from the laser aperture. The two orthogonal profiles are plotted together the gaussian power distributions which have a spot size, w, equal to the measured beam width at 13.5 % of the peak amplitude. As we can see, the gaussian function consistently underestimates the actual power distribution.

gaussian beam spreads out from its waist, any increase from this value may be due to a superposition of one or more transverse modes which are resonating together with the fundamental mode in the laser oscillator.

The experimental determination of M^2 followed a method included in the BeamScan instrument data analysis software. This method is based on the measurement of the beam width at the beam waist and after a distance equal to one Rayleigh range z_R at the two sides of the waist [see. [49]]. The estimated values for M_x and M_y given directly by the BeamScan software are shown in the Tab 5.2.

The new beam waist sizes and position were extracted from the new focused beam data.

Parameter	Value	CI	Unit
D_{0x}	0.218	$\{0.212, 0.224\}$	mm
D_{0y}	0.238	$\{0.231, 0.244\}$	mm
z_{0x}	683	$\{670, 696\}$	mm
z_{0y}	653	$\{639, 668\}$	mm
M_x^2	1.529		
M_y^2	1.622		
Ellipticity	1.09		

Table 5.2: Results of the nonlinear regression for the beam waists after the circularizing lenses and of the interactive program giving the M^2 measurement

From the last data set [see Tab. 5.2], one can conclude that the input beam is not an ideal TEM_{00} gaussian beam. However, the deviations produce a negligible effect on the coupling to our Fabry-Perot prototype. The extracted data are necessary in order to set the mode matching parameters. I took as reference values for both waist size and waist position the resulting averages: $w_0 = 0.114$ mm and $z_0 = 664$ mm.

The Faraday rotator was placed in the nearly-collimated beam region and followed by the mode matching lens. Before entering the cavity the light path was folded by three aluminum mirrors to achieve the optimal distance between the mode-matching lens and cavity (as established in Eq. 3.40). Practical reasons also set the minimal distance between the input bench and the cavity tank at d(table-cavity) = 588 mm. The overall view of the input optics is drawn in Fig. 5.3.

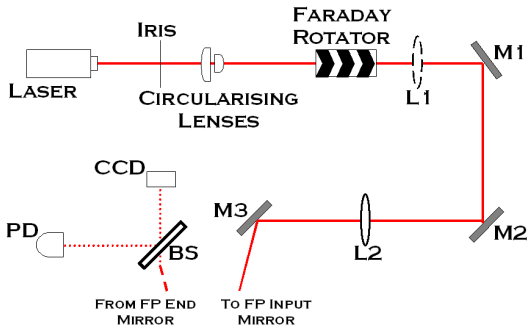

Figure 5.3: Schematic diagram of the Input/Output bench: L_1 is the mode-matching lens for the spherical optic case, placed approximatively at the same distance from the laser aperture I used to match the cavity; L_2 is the MH mode-matching lens at 2033mm far from the input waist.

5.2 Mechanical and optical cavity assembling

In this section the construction of the cavity is presented. Key design parameters are discussed along with their influence on the resulting electromagnetic field inside the structure. This work is complete and results have been published [50],[51].

An overview of the design and construction of the current MH test mirrors and expected beam behavior is also included.

5.2.1 Mechanical setup

Several issues motivated the final design of the cavity structure. We wanted to produce a resonant beam analogous to that on the surface of an advanced LIGO mirror. Hence the length of the prototype has to be

$$L_{prototype} = \left(\frac{R_{prototype}}{R_{adLIGO}}\right)^2 L_{adLIGO}, \tag{5.2}$$

where here R is the radius of the mirror. Once the diffraction losses (for the prototype the planned losses should be ≈1ppm) are fixed, the above equation establishes the cavity length. Table-top cavity lengths were excluded since a small radius mirror requires an unachievable manufacturing

precision by means the coating deposition technique[1]. The cavity length was chosen to be 16 meters, which became 8 for its half-symmetric cavity version.

A rigid structure was designed to sustain the optical elements: the longest available rods fixed the cavity length to 2×3.657 m = 7.32 m, through the use of a folding mirror at one end of the structure and the input and end mirror on the other end. The constituent material is INVAR because of its low thermal expansion coefficient (fractional expansion $\alpha = 2 \times 10^{-6} K^{-1}$). The required rigidity is achieved by three rods spaced by 5 triangular spacers. Two of them house the mirror mounts and are bolted at the ends of the structure.

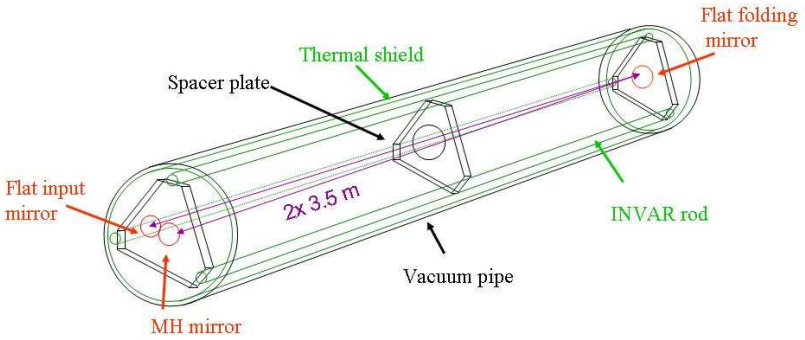

Figure 5.4: Schematic view of the mechanical structure

Ground vibrations can excite resonances in the rigid structure and disturb operations. To alleviate this problem the cavity is suspended by two pairs of maraging steel wires clamped to the second and the fourth spacers. This system provides the horizontal seismic isolation. Vertical seismic isolation is provided by GAS (Geometric-Anti-Spring) [52] blades which hold the

[1]The precision is not achievable by LMA Laboratories, as specified in Sec. 5.2.3, but diamond machining of aluminum mirrors could make a smaller optic. The price to pay was the profile could not be read from this aluminum mirror

suspension wires.

The structure is also enclosed in a vacuum tank. During this year of operations, the cavity was always used in air. The necessary space to mount the end barrels of the vacuum tank was left between the optical benches and the cavity. Hence the large distances shown in Fig 5.1.

The three mirrors are mounted in two monolithic holders, one of which is shown in Fig 5.5. The mirror holders are designed to allow a three dimensional rotation, which can be applied by three micro-metric screws mounted at 120◦ intervals around the periphery of the mirror. These three screws actually push piezo actuators, this allows us to not only translate the mirrors along the cavity axis but also to remotely control mirror alignment with high resolution. The elastic return force is supplied by a brass ring which is bent by pins aligned with each PZT on the opposite side of the mirror.

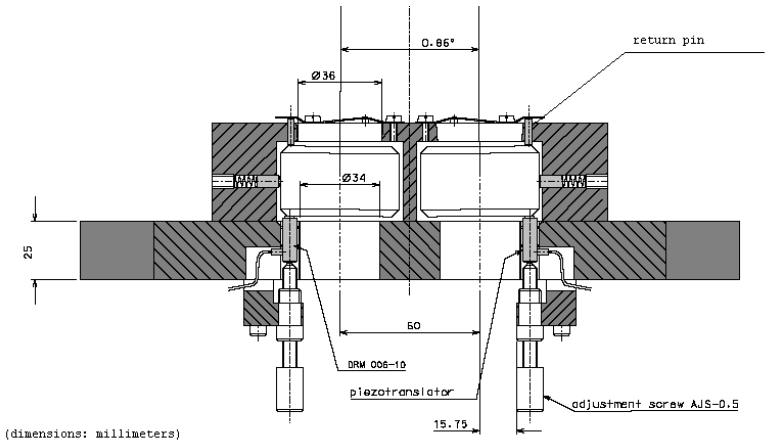

Figure 5.5: Transverese view of one of the two cavity end plates. The mirror positioning system is shown.

Both mechanical noises and piezo actuators were analyzed during the tests with a spherical end mirror. I will report these results in the following sections [see Sec. 5.5.2 and 5.5.3].

5.2.2 Cavity optics and spherical end mirror

Length constraints determined that our Fabry-Perot cavity be a half-symmetric, folded cavity. The optical elements consist of the three mirrors which are flat

in the case of the input and the folding mirror, and either spherical or "Mexican hat" in the case of the end mirror.

It is possible to re-write the cavity electromagnetic field equations for this configuration. They are broadly similar to those for a standard two-mirror Fabry-Perot resonator. The solution for the internal field and the transmitted one is the same as in the Eq. 3.28, we simply change the expression for the cavity finesse as follow:

$$\mathcal{F} = \frac{\pi\sqrt{r_1 r_2 r_f^2}}{1 - r_1 r_2 r_f^2} \tag{5.3}$$

where the folding mirror reflectivity r_f has been introduced.

The choice of the cavity finesse value represents a compromise between cavity optical performances, i.e. the ability of the cavity to clean the laser input beam into a pure cavity resonant mode, and technical difficulties. Ease of lock acquisition is as critical as a high cavity finesse. The finesse is established by the value of the input mirror reflectivity, since for both the folding mirror and the end mirrors a high reflectivity was chosen ($r_f^2 \simeq r_2^2 = 99.9\%$). The desired value of $\mathcal{F} = 100$ is approached by a power reflectivity value of $r_1^2 = 0.95$, which yields an actual finesse value equal to 110.

The fiducial cavity length is given by doubling the length of the rods, which fixes $L = 7.32$ m and so the FSR of the cavity at $\Delta\nu_{FSR} = 20.49$ MHz. The width of the spectral lines without taking into account losses will be $FWHM = 0.184$ MHz.

Initial tests of the experiment were performed with a spherical end mirror. We started with a spherical mirror because it is well understood optically and allow us to characterize the rest of the system.

The radius of curvature of this optic was the largest available among commercial mirrors with a high reflectivity coating ($r_2^2 = 0.999$) and 2 inch size. It had the value $R_{roc} = 8$ m. The $g-$parameters for such a cavity will be $g_1 \simeq 1$ and $g_2 \simeq 0$, like a nearly-confocal cavity, producing close to the maximum spacing between the transverse modes but also a near degeneracy between different axial series. Another reason why this value for R_{roc} was chosen was that it gives us a nearly unstable cavity, like the designed Mesa beam cavity.

From a geometrical point of view, the flat input mirror dictates that for the resonant modes in both spherical and Mexican hat configurations,

the cavity waist be on the flat input mirror. Hence in the spherical case the resonant fundamental mode will be half of a *nearly-concentric* gaussian beam. The expected beam waist in this case will be

$$w_0^{sph} = \sqrt[4]{\left(\frac{\lambda}{\pi}\right)^2 L(R-L)} = 0.869\text{mm}. \tag{5.4}$$

This value has been used to mode match the input beam which was characterized in the previous section.

5.2.3 MH mirror production and test mirrors analysis

The test MH mirrors were designed using the waist size of the minimal gaussian with $L = 2L_{cavity}$ as a reference length, so that $b = 1.57$ mm and the mesa beam radius $D = 4b = 6.30$ mm. In order to have 1 ppm diffraction losses the mirror radius was set to $R = 13$ mm.

At the end of March, the production of the first Mexican hat mirrors was completed at the Laboratoire des Materiaux Avances in Lyone (LMA). Their procedure to manufacture these mirrors consists of a three step deposition process over a micro-polished flat substrate: the general shape is deposited with a precision of about 60 nm using a profiled mask and rotating the substrate to generate the cylindrical symmetry. The mask, calculated from the thickness profile of the ideal Mexican hat, is placed between the sputtered flow of silica and rotating substrate.

The second step is a more precise correction of the "general shape" previously obtained. This method controls the deposited profile with a precision of about 10 nm Peak-to-Valley (PV). Nevertheless, it is not possible to coat more than 100 nm with this technique, because this would require a deposition time which is prohibitively long.

The first operation of the second step above is to measure the achieved mirror surface and compare it with the theoretical shape of the MH. The measurement of the achieved mirror is performed using a Fizeau interferometer. The comparison between the achieved and the desired mirror shape generates a data file which is used to move the robot arm, positioning the mirror in front of the corrective silica beam. The main limitations of the corrective technique come from the measurement of the wavefront, the precision

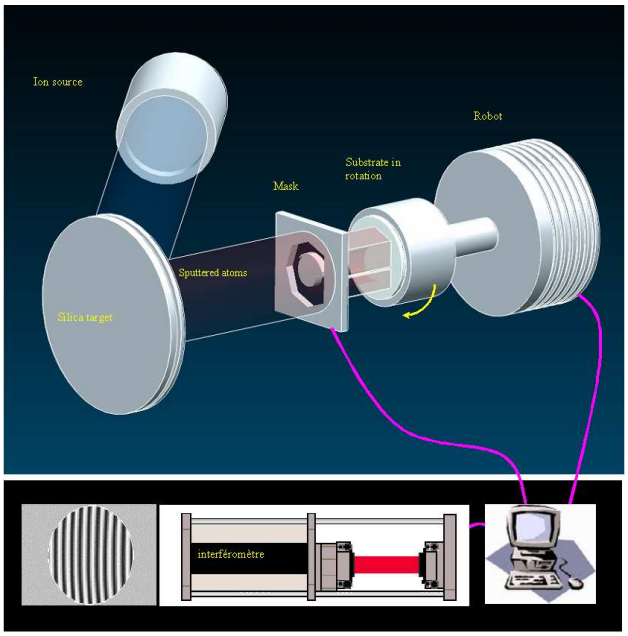

(a) General shape deposition process

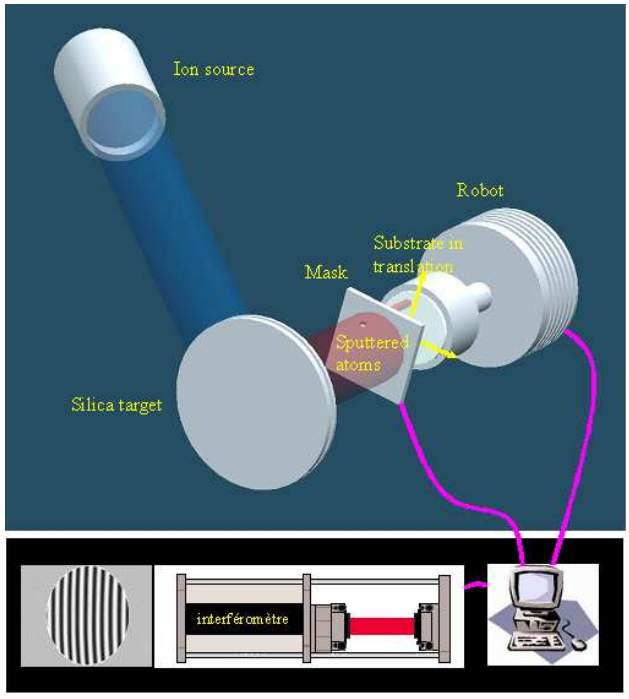

(b) Corrective treatment

Figure 5.6: LMA Laboratories' technique for MH manufacture: schematic diagrams.

of the robot arm movement and the size and resolution of the SiO_2 corrective beam. The maximum measurable slope is 500 nm/mm, thus setting a limit on the smallest feasible Mexican hat mirror. Finally, a high reflectivity SiO_2/Ta_2O_5 multi-layer coating is deposited on the corrected substrate. The manufacture steps are shown in Fig. 5.6.

Since the beginning of the test runs, the second step of the process caused many difficulties. These were essentially due to the mirror positioning stages, which are not well suited to the required precision [53]. In particular, the corrective treatment produced at the beginning a large offset of the central bump which was gradually corrected and almost completely eliminated, and a slope on the silica deposition which amounts to about 1 μrad on the central part (diameter 14 mm) or more.

All the other sources of light loss such as light scattering, substrate and coating absorption, are below tenths of ppm's. The transmission maps are not uniform and reveal a transmission peak on the center. The average values are all around 1000 ppm.

The three mirror maps were analyzed by implementing them in a FFT routine that simulates beam propagation inside our cavity in the paraxial approximation regime. The results of these simulations showed that the resonant beam shape will be affected by this mirror slope, but it is possible correct it by applying the same amount of tilt to the mirror.

The ripples in the central area are inevitable due to the limited accuracy of the corrective coating deposition and set a limitation of about 10 % PV on the flatness of the power distribution on the top of the beam. However the steep fall on the edges and the width of the beam should be very close to the ideal perfect mirror case.

Of the three mirror samples, I decided to first install the one which performed best in the simulations: mirror C05008 [see Fig. 5.7]. All the resonances should not be affected by scattering and absorption, since they will be at least two orders of magnitude less than the transmitted light. Diffraction losses are even lower than other loss mechanisms and this should be true for all the lowest 'TEMs'[2].

[2]We denote 'TEM' the transverse modes for the Mexican hat cavity in order to not confusing them with the ordinary gaussian modes

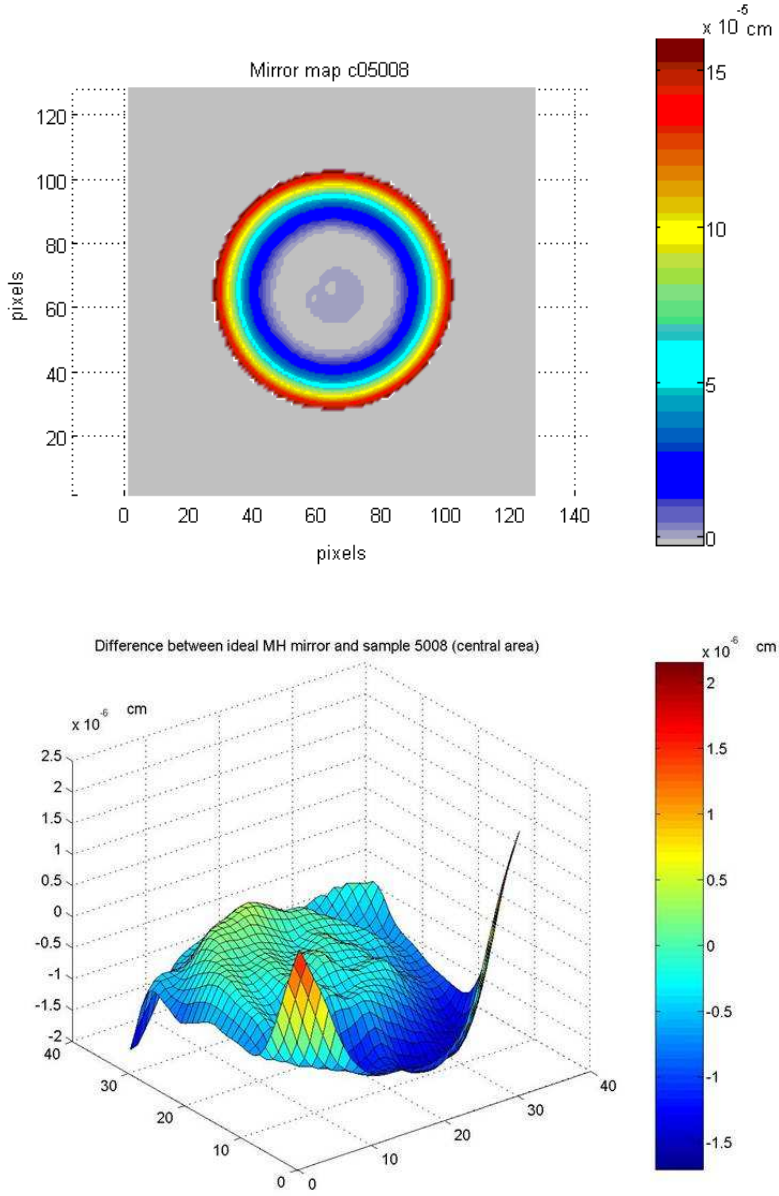

Figure 5.7: Mirror profile of the Mexican hat sample number C05008 and difference between the ideal profile and the actual map in the central part.

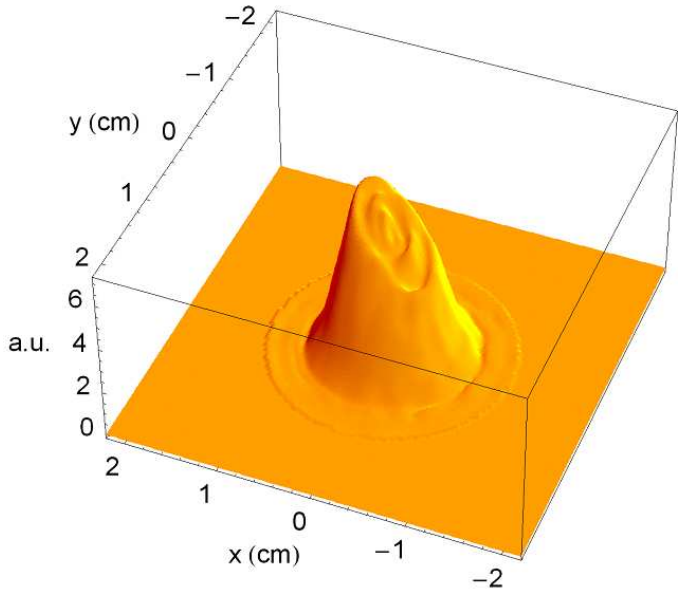

(a) Transverse electromagnetic field result from FFT mirror map implementation

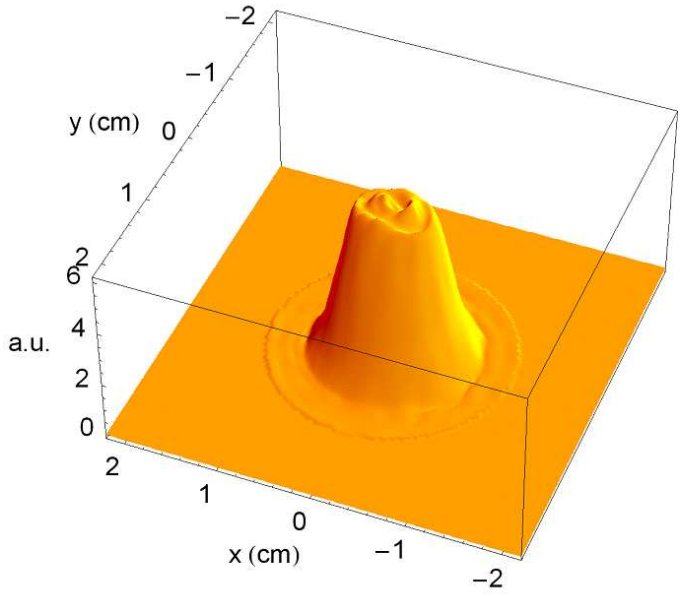

(b) Transverse electromagnetic field at the input mirror after the correction tilt

Figure 5.8: FFT simulations to determine the fundamental mode of a FP cavity with the MH mirror C05008

5.3 Cavity control electronics and piezo driver circuit

Cavity lock was obtained by taking a fraction of the transmitted power from the end mirror or one of two transmitted beams from the folding mirror. During the test with the spherical end mirror both the layouts were tested. In order to feed the whole power distribution into the photo detector, a lens is necessary before the beam splitter, another lens would then be necessary to re-focus the beam in order to be acquired [see Fig. 5.3]. In order to avoid beam distortions and secondary reflections, I separated the beam profile acquisition from the output signal acquisition, leaving the latter on the input bench and moving the camera used to study the resonant beam to the bench at the opposite end of the cavity.

The photodiode used was a Thorlabs DET110 [54], a high speed Si photo detector. It transforms the light power signal into a current signal. This information is then transformed into a voltage signal using a resistive termination (50 Ω or 4.7 kΩ). This raw signal is preliminarily processed by a preamplifier (model Stanford Research Systems SR560), which amplifies the signal and works as low pass filter. The amplitude gain and the bandwidth can be set in order to improve servo performance.

Such an output signal is used to generate the servo error signal and is sent either to a digital oscilloscope or a DAQ board installed in a computer in order to be read in real time or saved and analyzed later.

Two different servo loops have been implemented in order to lock the cavity. The first loop is based on the sidelock technique and uses laser injection current feedback to control the resonant beam detuning phase. The second loop is a dither locking scheme, and both the modulation and the feedback occur on the cavity length. The lock schemes are shown in Fig. 5.9.

Both servo loops used a custom *servo amplifier* that I designed and implemented. It consists of three stages of DC amplification. The first stage is the DC bias. It consists of an inverter, made with an operational amplifier with unity gain. Here the external input, through a BNC, goes to the negative input. At the positive input, a +10V voltage is applied through a potentiometer which sets the DC offset. The difference that comes from the amplifier can be used as an error signal for the sidelock scheme.

The second part of the circuit is the proportional-integral amplifier stage: the error signal is fed in parallel to a variable gain inverting amplifier and

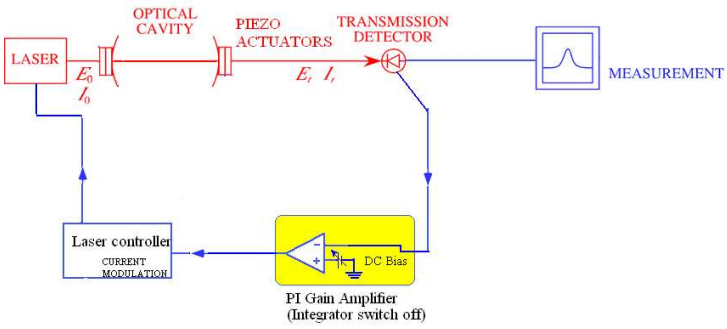

(a) Cavity sidelock servo loop: the transmission signal is compared to a DC offset and fed back to the laser controller

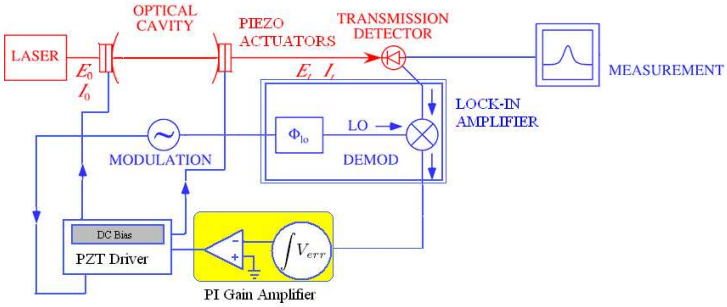

(b) Cavity dither servo loop: the cavity dither modulation is applied through the PZT driver which amplifies the modulation signal. The same signal is used to create the local oscillator (LO) signal which is used to demodulate the transmitted signal.

Figure 5.9: Schematic configurations of the servo loops for the cavity locking

an integrator circuit. The last part has been designed with a JFET input operational amplifier (model LF 356) to avoid drift effects due to offsets and bias current, and a high RC time constant ($\simeq$ 0.1 sec) to compensate drift effects of the laser frequency. A two pole switch is connected to the capacitor pins to turn off and on the integration. The proportional stage is then summed to the integrated signal and the resultant signal is finally processed in the third stage which provides a fine amplitude adjustment and the possibility to choose between the inverted or non-inverted signal.

The schematic of this circuit is shown in Fig. 5.10.

As previously explained, the sidelock scheme is implemented by comparing the reference bias signal to the photodiode signal inside the servo amplifier. This signal is directly fed back to the laser controller through the current modulation BNC.

In order to lock on the peaks of the cavity spectrum, a dither lock servo loop was also used. In this case, the error signal is generated by a lock-in amplifier (model Stanford Research System SR510), as described in Sec. 3.3.1. A wave function generator was used to provide the length modulation and the reference signal. The sinusoidal signal is sent to the PZT driver circuit with a dither frequency which was found to be optimal between 10 and 20 kHz. The demodulated error signal is then fed back to the cavity through the servo amplifier where the error signal is integrated.

The cavity dither modulation is applied through the simultaneous movement of the three piezo actuators on the cavity input mirror. This is made possible by a voltage signal generated by a custom driver circuit. I designed and constructed this simple *PZT driver circuit* as a DC voltage amplifier. The main purpose of this device is to provide the needed voltage to move the mirrors for cavity alignment without touching the cavity. It has to be able to amplify an external input as a dither or a feedback signal with a limited bandwidth.

The PZT driver circuit has 10 channels with two amplifying stages: a preamplifier which can sum the external input and the positive DC bias, shunting any negative any voltage swings through a Schottky diode on its feedback network. It is able to provide an output DC bias up to +15V and it has a AC gain of about 5. Such a signal can be sent directly to the piezos or to the second stage. This second stage has been implemented with a power amplifier (APEX PA82) able to reach a voltage amplitude of 100 V,

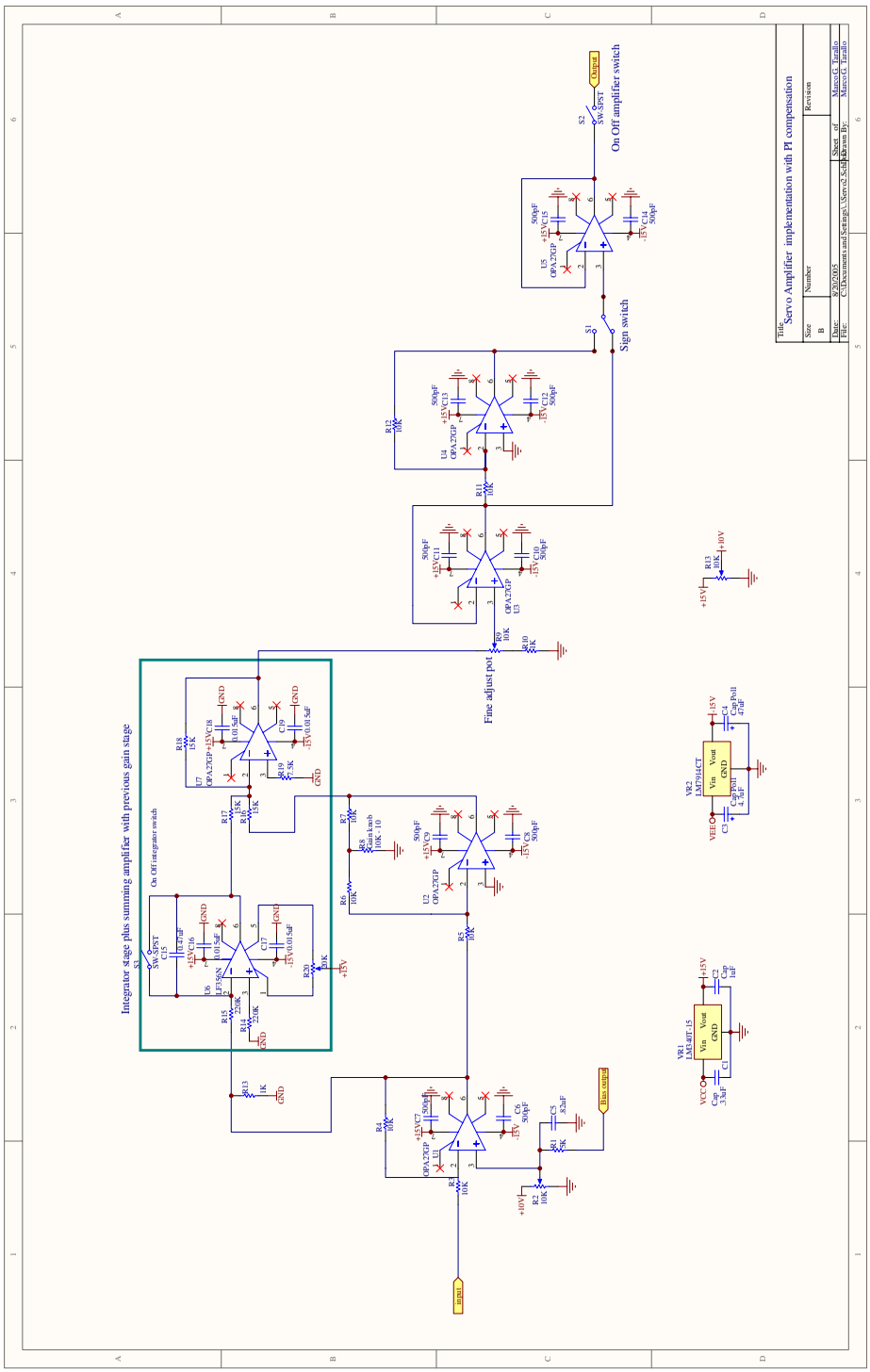

Figure 5.10: Schematic diagram of the servo amplifier used to lock the cavity prototype

which corresponds to the full design range of the piezo actuators. This stage essentially consists of a non-inverting DC amplifier; a capacitor has been placed on its feedback network in order to reduce the high frequency gain. The schematic diagram of the single channel design is shown in Fig. 5.11.

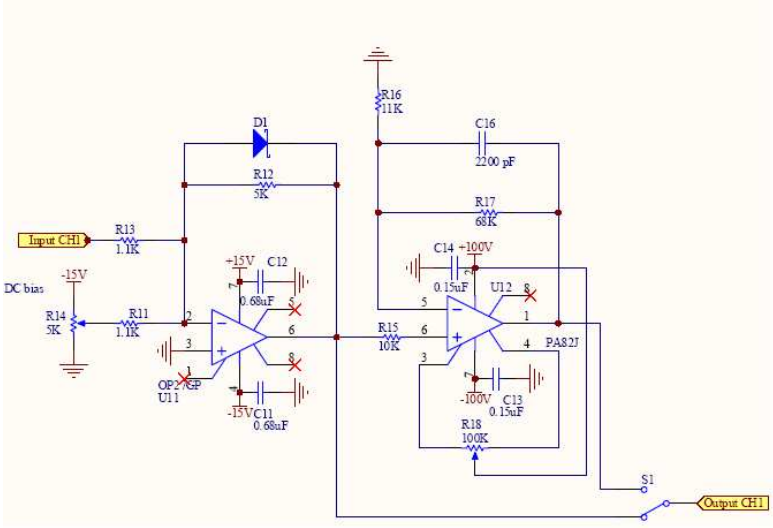

Figure 5.11: Schematic diagram of the single PZT driver channel

Since the piezo driving is a crucial task, the driver channels connections were built on two printed circuit boards with a ground plane to reduce electromagnetic coupling effects. The boards were designed to reduce coupling noise between the channels, and the whole driver box works as Faraday cage. A digital panel voltage meter has been put on the driver allowing the driving bias applied to each piezo to be measured. Details of these two issues are exposed in Appendix A.

5.4 Beam profile acquisition

The resonating transverse electromagnetic field distribution is analyzed using the power intensity map grabbed by a CCD (charge-coupled device) camera, the LaserCam IIID 1/2". As with all common beam diagnostic CCD cameras, it has a limited beam size resolution and a very sensitive 2-D array. It means

that beam profiling requires a preliminary adaptive optics before analyzing the beam. In Fig. 5.12 the layout of the profile readout optics is shown.

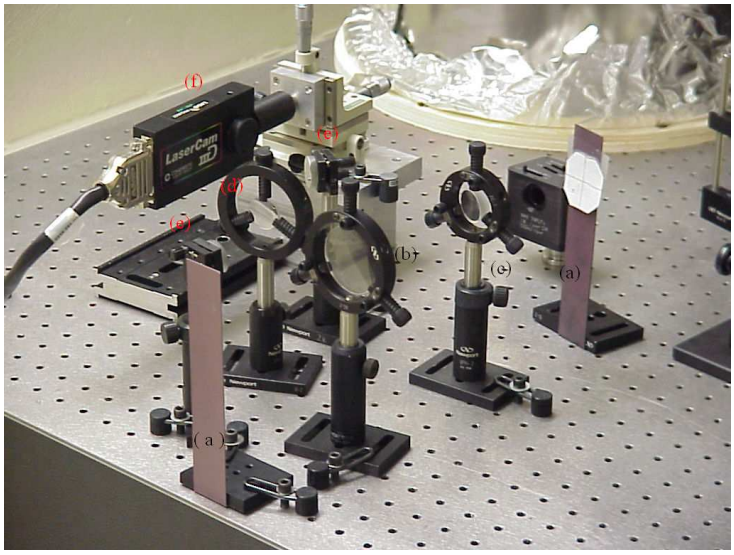

Figure 5.12: Profile readout optics layout: (a)beam dumps; (b)focusing lens; (c)wedge; (d,e) mirrors; (f)beam profiler on the movable stage

The main features of the diagnostic camera are summarized in Tab. 5.3: the CCD array sensitive area is 4×4.7 mm^2 with a spatial resolution less than 20 μm in both transverse dimensions. The intensity saturation is 0.8 mW/cm^2 if the Low-Distortion Face Plate (LDFP) filter is mounted before the array. It is also equipped of a large dynamic range, resulting in a high resolving power.

The LDFP filter, mounted in front of the camera array, is a laser-grade neutral density (ND) filter glass specified and polished for diagnostics use. It provides sufficient attenuation of room light, so that operation with room lighting on was possible. It also provides protection from dust which can yield diffraction patterns on the image.

In order to reduce the beam intensity under the saturation level, a 10◦, 1 inch wedge was employed, because of its low image distortion and lack of interference fringes as produced by ordinary ND filters. A focusing lens was placed in front of it during the operations with the spherical end mirror. During MH operations, the large mesa beams are focused by two lenses, one of which has 2 inch diameter to reduce spherical aberrations and vignetting.

Camera name	**LaserCam IID 1/2”**
Sensor Array	Interline Transfer CCD (frame integration)
Spectral Response	Silicon, 400 nm to 1100 nm
Digitized Pixel Resolution	17.05 μm $\times$ 19.69 μm
Saturation	1.5 mW/cm^2 (at 632.8 nm CW)
	0.8 mW/cm^2 (at 1064 nm CW)
Background	0.6 nW/cm^2 (at 632.8 nm)
Optical Dynamic Range	Greater than 900 to 1
Field Rate	60 Hz

Table 5.3: Summary of the CCD profiler physical characteristics [56]. The data above is referred to the camera complete with an LDFP

Two mirrors work as a periscope to align the beam onto the sensitive area of the camera. Finally the camera itself is mounted on a translation stage.

Beam profiling tests were performed with a He-Ne laser, whose power stability has been demonstrated in previous experiments [55]. The gain uniformity over the camera array and data acquisition process were checked.

The laser beam from the test laser was sent to the camera placed on the readout bench with the same layout of the cavity beam acquisition. A ND filter was placed in front the laser to provide further beam attenuation. The reflected beam from this filtering stage was read using a photodiode to monitor the laser intensity stability. In the end, a mirror folded the beam to the wedge. Moving the camera in orthogonal directions, several data of intensity peaks have been taken. The fit result for a constant intensity beam shows a variance $\sigma^2 = 9.8$ digits^2 with an average value of $< I >= 210.1$ digits. This means that the camera uniformity is about 1.5 %. It is more difficult to estimate the single pixel fluctuations. Assuming a perfect gaussian shape for the test beam, I can conservatively estimate the relative intensity fluctuations as the average of the ratio between the fit residual absolute value and the model value. The average of the ratios between the single pixel residual and its expectaton value (given by the best fit result) gives a pixel to pixel maximum relative error of 5.9 %.

5.5 Experimental setup characterization: optics, mirrors nanopositioning and noises

In the previous sections a general overview of the components of the experiment was presented. In this section I want to point out our attention to how the experiment has been modified and characterized, during the cavity operations, in order to get the results of the next chapter. In particular, the input mode matching was changed to match the new input waist and the large distance between the cavity tank and the optical bench. The Fabry-Perot itself was used as a position sensor to calibrate the piezo actuators by imposing a displacement equal to half of a wavelength when two longitudinal resonant peaks were found. Finally, during lock runs, several transmitted power signals were captured and spectral analyses were performed on them to understand potential sources of noise and instability in the mechanics or in the control electronics.

5.5.1 Input mode matching

Once determined the reference value for the input waist size and position, the input mode matching for the half nearly-concentric test resonator was just a matter of choosing the optimal focal length in accord with Eq. 3.40. For a characteristic length $f_0 = 292.5$ mm, since both d_1 and d_2 are proportional to f, the best solution was $f = 400$ mm, which sets $d_1 = 436$ mm and $d_2 = 2480$ mm. Thus, the folding mirrors were placed on the optical bench in order to satisfy these distances.

In the case of the MH cavity mode matching, a more detailed analysis was done. The mode-matching problem for such cavities can be treated as a gaussian beam mode-matching problem taking a reference waist size value to match w_G introduced in the previous chapter. This means that our w_2 is

$$w_2 \equiv w_G = 3.62b = 5.7 \text{ mm} \tag{5.5}$$

This value set the required magnification ratio to $w_2/w_1 = 50$, and the characteristic length of the re-focusing system to $f_0^{MH} = 1918.6$ mm. The principal parameters to take into account are the finite space available and the "stability" of the solution, i.e. small translations of the optical elements should not affect too much the resulting beam. It is clear that a one lens

mode-matching would require very long distance d_{tot} between input waist and the input mirror surface (about 40 meters for a perfect mode matching if f = 2000 mm). On the other hand, an exact solution for a two lens telescope with fixed value d_{tot} around three meters requires a precision of the order of tens of microns, which I considered unreasonable.

Thus, the design of the optical system to mode-match the MH cavity was modeled as a problem of minimizing the power lost by the fundamental to the excited modes. Considering the problem as a gaussian beam mode-matching, to first order the power lost is the square of the coupling coefficients for a mode mismatch, as shown in Sec. 3.3.2. Thus, I defined the quantity to minimize Q defined as

$$Q = \frac{1}{2}\left(\frac{(w_G - W)^2}{w_G^2} + \left(\frac{z_0 - Z}{2z_R}\right)^2\right), \tag{5.6}$$

where here W is the waist size of the input beam, z_0 and Z are respectively the position of the input mirror and of the input beam waist, and z_R the Rayleigh range of the beam to match.

Of course, this is a good approximation in the limit in which $Q << 1$. So, a satisfactory input telescope has to keep this value as low as possible. Solutions of the problem were proposed for the one lens system and for the two lenses system studying the solution of Eq. 3.41. In the end, the single lens telescope was preferred with the following parameters: f = 2033 mm; d_1 = 2033 mm; d_2 = 830 mm (distance between input mirror and lens); Q = 0.002. Details of the analysis are shown in Appendix B. Another estimate of how good is the coupling for such a input beam has been done by evaluating the FFT results for the cavity power: here the real shape of the MH mirror is also considered.

5.5.2 Piezo actuators calibration

In order to know how much a piezo translator tilts the mirror, the displacement for 1 Volt input has to be known. This task was performed by sweeping the cavity length (with the spherical end mirror inside) and measuring the difference of potential applied to the actuators to complete a full FSR, which corresponds to displacement equal to $\lambda/2$ = 532 nm.

In particular, intensity maps of the transmitted power were recorded for different triangular wave amplitudes and frequencies. Ten FSRs were recog-

nized on each sample along one ramp of the sweeping signal. The results for the input mirror are shown in Fig. 5.13.

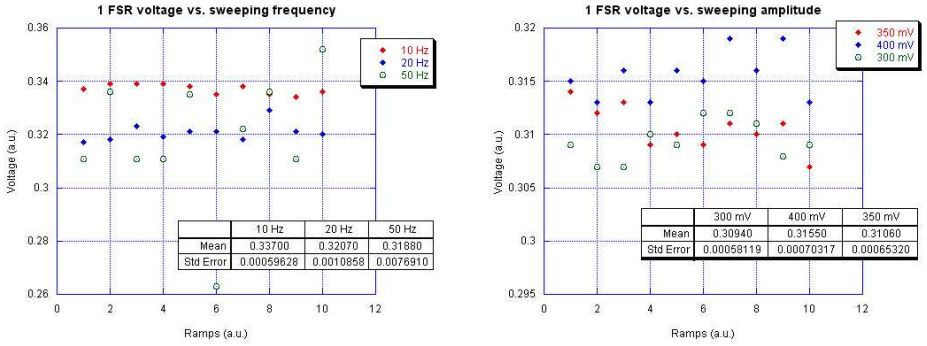

Figure 5.13: Calibration curves for different amplitude and frequency sweep waves.

The data seems independent from the sweeping amplitude and sweeping frequency. In particular, at 50 Hz the sampling rate (f = 40 kHz) and a bad cavity alignment caused worse peak recognizing as shown in the graph.

Once the driver gain is factored in, the calibration values for each mirror can be extracted averaging among the amplitude sweeping samples. The displacement values when a one Volt is applied are:

$$\Delta l(\mathrm{IM}) = 52.0\mathrm{nm}, \quad \sigma(\mathrm{IM}) = 0.5\mathrm{nm};$$
$$\Delta l(\mathrm{EM}) = 51.1\mathrm{nm}, \quad \sigma(\mathrm{EM}) = 1.5\mathrm{nm};$$

5.5.3 Cavity noises

A brief overview of the lock signal is presented. Several samples with 4 seconds length were acquired by the DAQ system. They were analyzed with MATLAB in order to recognize evident sources of noise in the mechanical or electronic environment, or possible servo loop instabilities which could yield servo oscillations. However, since our experimental purposes were just to keep the beam stable enough to analyze its optical features, the servo performances were not optimized. In fact, when a good alignment was achieved, the cavity

kept its lock for very long periods, allowing us to perform beam analysis "on-line".

Figures 5.14 and 5.15 show two typical power spectra of the transmitted power signal respectively when the sidelock scheme and the dithering are used.

In the case of side locking, the most relevant problems were: a limited offset range due to a large response of the laser for small voltage error signals which sometimes were translated in oscillations at the servo pole frequency f = 2340 Hz; two (or more) narrow resonances of the system at 32.25 Hz and 40.25 Hz. We believe they are mechanical resonances of the rigid structure which were sometimes excited by acoustic noise.

For dither lock scheme, The two resonances at 32 and 40 Hz are almost invisible but a strange coupling with AC line is present: all the harmonics of 120 Hz have a peak in the power spectra (probably from the lock-in amplifier). Perhaps locking to the top of the resonance, where $dV/dl = 0$ and so the cavity is less sensitive to length changes, the acoustic coupling is strongly suppressed with respect electronics disturbances.

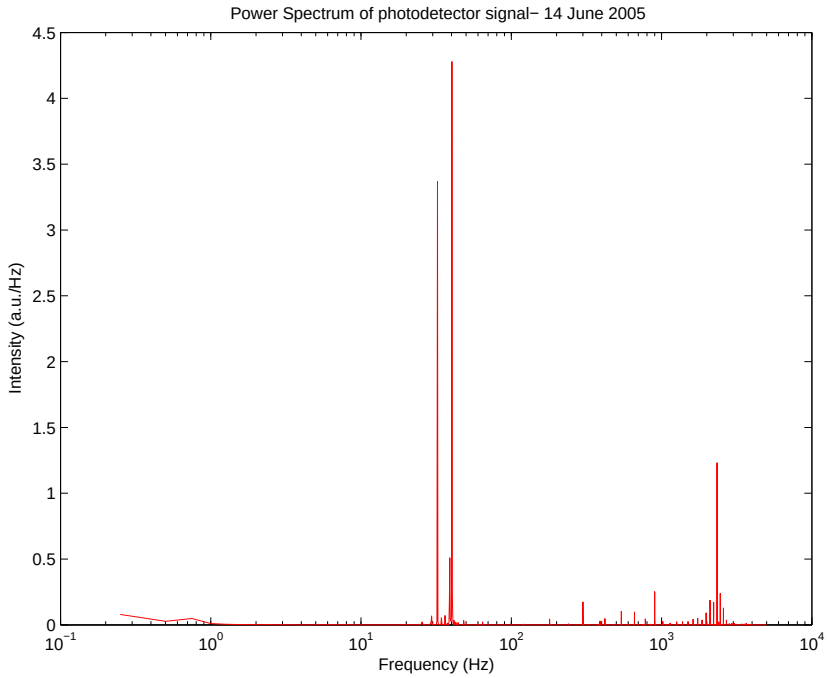

Figure 5.14: Power spectrum of a transmission signal from the photo detector during a cavity lock in the side lock scheme

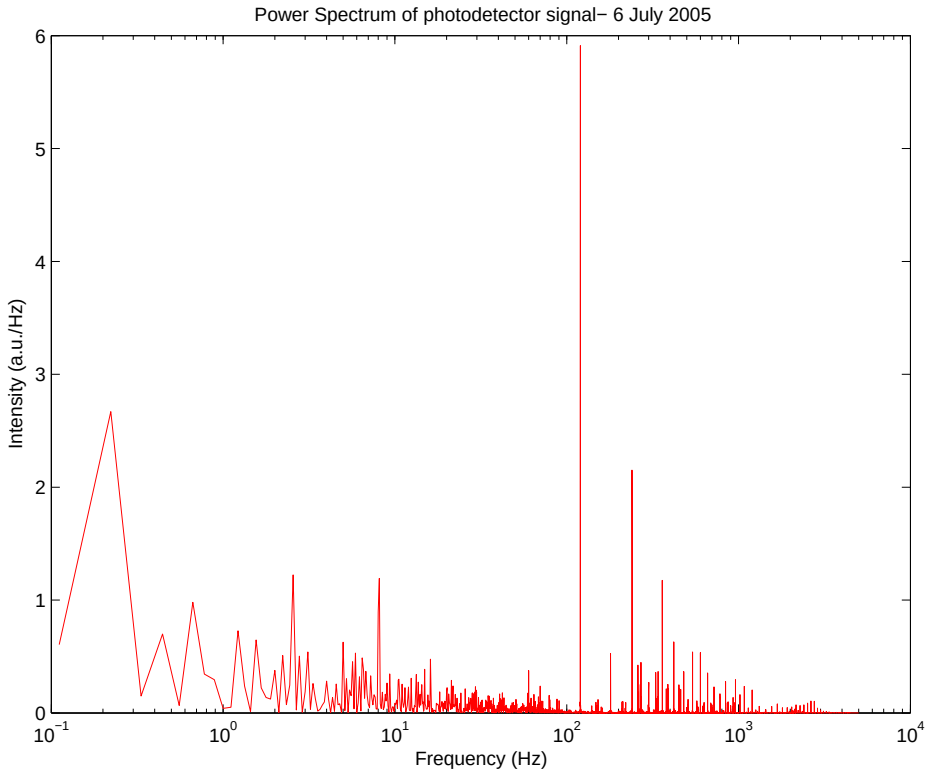

Figure 5.15: A particular power spectrum of a transmission signal from the photo detector during a cavity lock in the dithering scheme. The highest peak is at 120 Hz

Chapter 6

Results

In this chapter the beam profile analyses for both spherical and Mexican hat optical configurations are presented. The comparison between gaussian electromagnetic field patterns and actual intensity maps were performed for several of the transverse modes of the cavity, trying to model every deviation from the ideal case.

When the first MH mirror was installed, the main task was to find a satisfactory alignment configuration of all the optical elements. Several unpredicted resonant modes were found and their lock was stable and powerful.

I used a dedicated FFT model, the same used to predict the resonant beam for each MH sample, to recognize the resonant modes and characterize the causes of such behavior. It resulted that most of the resonant field patterns can be seen as due to misalignments of the input beam or the cavity mirrors.

Since simulations predicted the possibility to lock on some modes similar to the ideal Mesa beam, other causes were investigated. In particular, changing the flat mirror mounting and increasing the cavity insulation from external effects, a Mesa beam profile was finally recorded. The beam profile and spectral analysis are presented.

6.1 Cavity prototype resonant modes with spherical end mirror

Preliminary cavity operations were done with the spherical end mirror as described in the previous chapter. An important task of these tests was

the complete characterization of an optical resonator, in terms of its modal structure and its response to perturbations such as input mismatches or misalignments.

Since gaussian functions are the only ones which remain the same when they propagate through free space, it is possible to study beam profile data in any longitudinal position and compare the beam profiles with the ideal gaussian transverse modes. Mode shape asymmetries induced by optics astigmatisms or aberrations were than estimated by the observation of the fit residuals.

Figure 6.1 shows some transverse intensity patterns which have a marked cylindrical symmetry.

During the analysis of the residual maps for pure Laguerre-gaussian functions, the readout optics were modified in order to improve the quality of these data sets. In particular, the folding mirror was replaced with one with one degree wedge on the uncoated surface to reduce interference effects due to secondary reflection.

The goodness of fit has been evaluated for most of the beam profile samples acquired. A measure of this is the "coefficient of determination" R^2, defined as the ratio of the model sum of squares to the total sum of squares[1]:

$$R^2 \equiv 1 - \frac{SS_{res}}{SS_{tot}} \tag{6.1}$$

It quantifies how much the fit model is able to explain the error of the experimental data. In Tab. 6.1 some of the R^2 values for the analyzed data are presented for the Laguerre-gaussian eigenfunctions fits.

We tried to reduce parasitic interference fringes by means of the installation of the wedge instead of a 1 cm polarizer cube beam splitter. It had an effect on the fundamental mode fit but, for the higher orders the goodness of fit became worse and worse. Attempts to improve cavity alignments resulted in the gradual complete lost of the cylindrical shape of the resonant modes, which changed their intensity distribution into the Hermite-gaussian mode set.

Serveral Hermite-gaussian eigenmode profiles were analyzed. Some of their intensity distributions are shown in Fig. 6.2.

[1]In case of nonlinear regression the calculus of R^2 uses the corrected sum of squares instead of the total sum of squares[57].

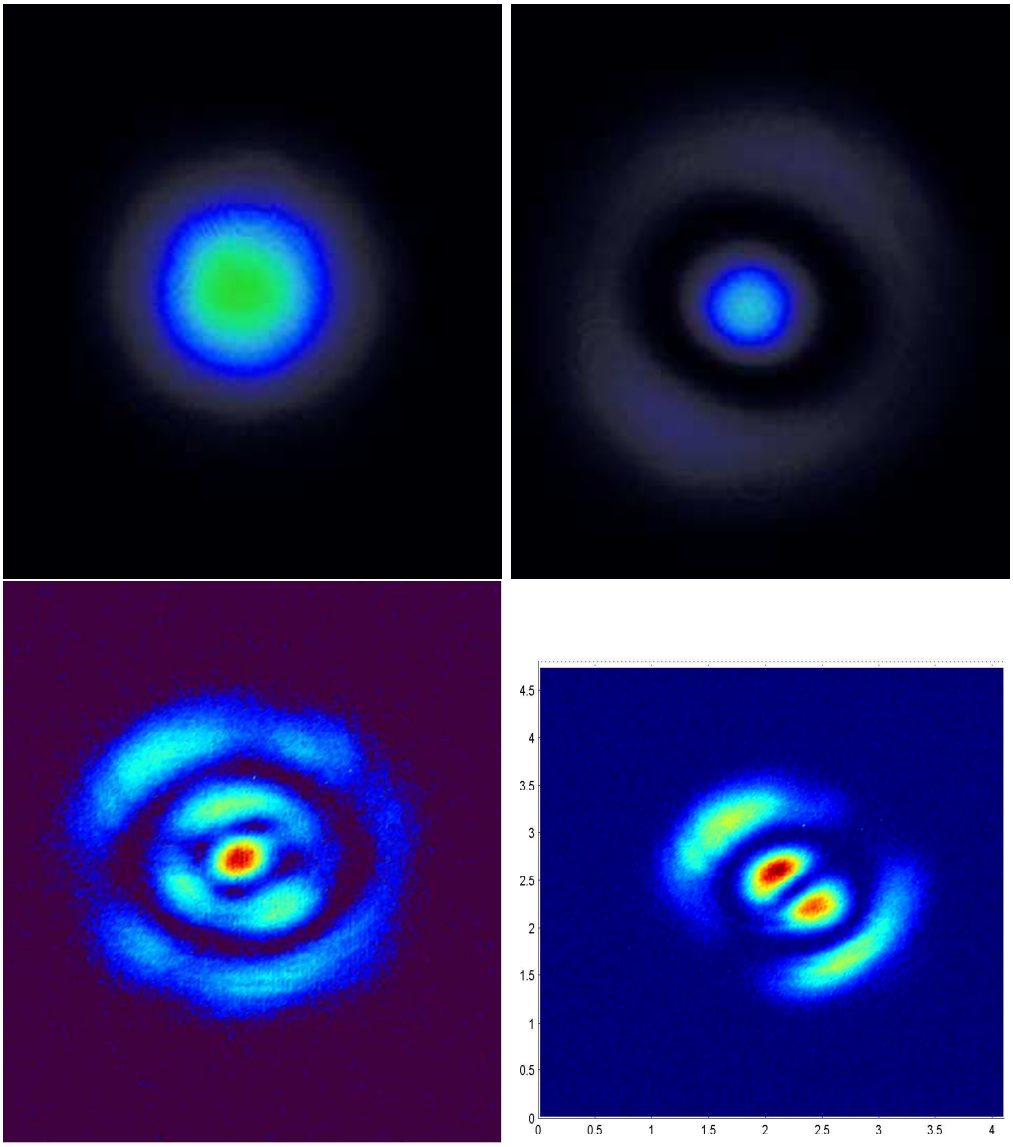

Figure 6.1: Two-dimensional profiles of Laguerre-gaussian eigenmodes for the Fabry-perot cavity prototype during test runs with a spherical mirror. Clockwise from the top left corner: TEM00, TEM10, TEM20, TEM11. The last two were plotted with MATLAB since their peak intensity is too low for the Beam Analyzer software

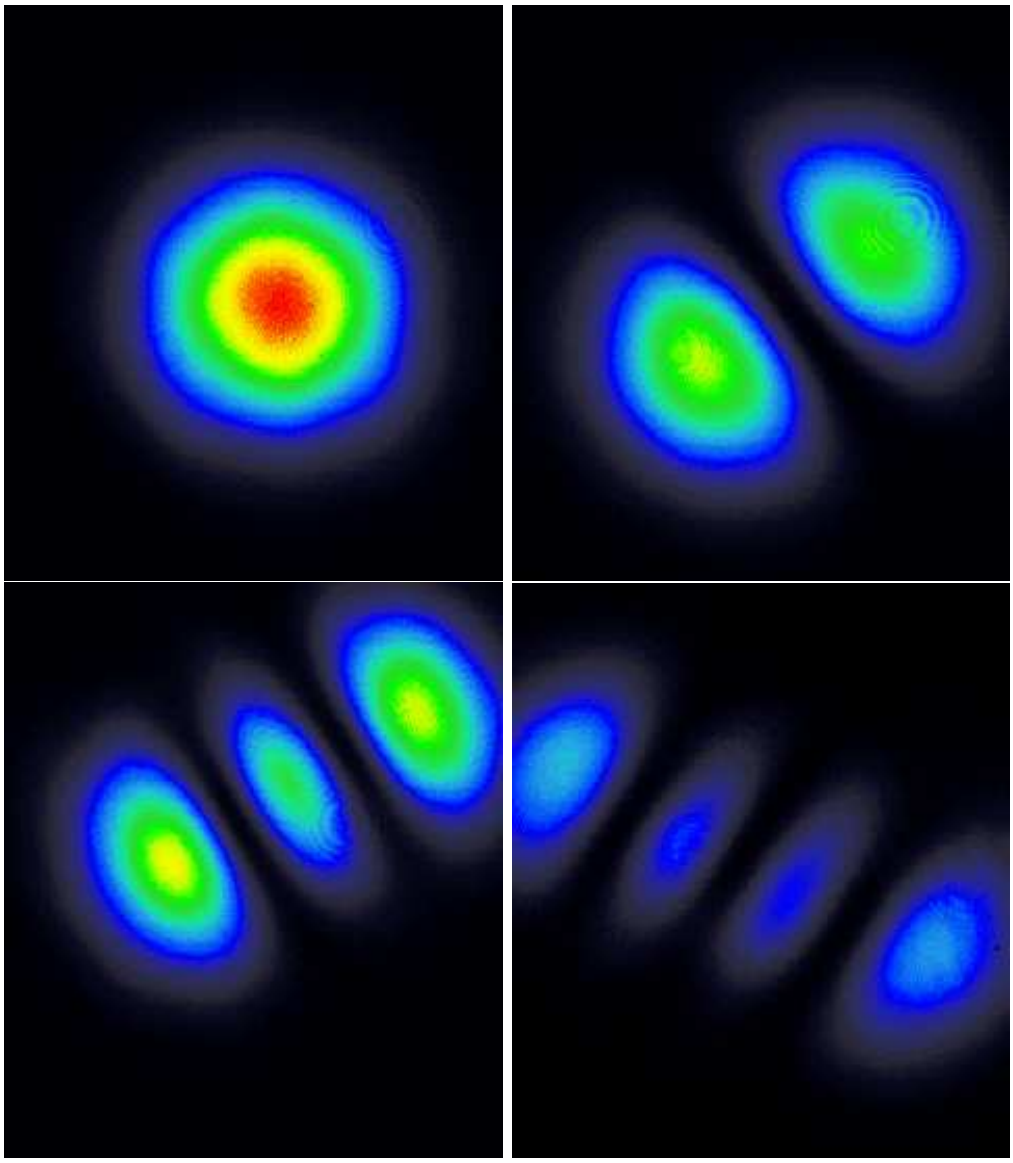

Figure 6.2: Hermite-gaussian transverse field power distributions. Clockwise from the top corner: TEM_{00},TEM_{10},TEM_{20},TEM_{30}. It is possible to observe that one of the two symmetric peaks is always brighter than its correspondent for the higher TEMs.

TEM(pl)	**Rsquared**	**Ellipticity**	
TEM_{00}	0.979	1.05	
TEM_{00}	0.998	0.99	
TEM_{01}	0.958		
TEM_{10}	0.960		
TEM_{10}	0.729		
	0.956	0.98	(same sample but fit func. as superposition of HG20+HG02)

Table 6.1: Results from the nonlinear regression on the pseudo-Laguerre-gaussian resonant eigenmodes for the spherical setting of the cavity prototype. The ellipticity parametrizes the asymmetry introduced in the fit function.

The main peculiarity of these data was the marked unbalance between transverse peaks which are supposed to have the same intensity. From eight acquired intensity patterns of the TEM_{10}, the average unbalance between the two peaks amounts to 13.9 %.

The modal structure of the test spherical setup for our cavity prototype was studied analyzing the cavity spectral behavior (one of the recorded spectra has been shown in Fig.3.3). Although the large separation for the transverse modes may yield a degeneracy between modes belonging to different axial series, the minimal frequency separation expected is always larger than the nominal FWHM. In fact, locking on the peak of the Airy curve did not eliminate the intensity peak unbalance problem.

Remote alignment adjustments were applied to the cavity mirrors by the piezo translators. No change was seen in the TEMs power distribution. For large amount of mirror tilts, we saw the change of the optical axis manifested as a change of the beam position on the camera array.

As for the pseudo-Laguerre-gaussian, a table for the Hermite-gaussian fit is presented in Tab.6.2.

The beam profiling analyses can be improved if known sources of noise such as local random fluctuations due to the digitized process of image acquisition and diffraction circles due to dust grain are filtered from the raw

TEM(mn)	Rsquared	Ellipticity
TEM_{00}	0.996	0.93
TEM_{00}	0.996	0.98
TEM_{00}	0.996	1.02
TEM_{00}	0.998	0.99
TEM_{10}	0.981	0.92
TEM_{10}	0.995	1.02
TEM_{20}	0.976	1.06

Table 6.2: Results from the nonlinear regression on the pseudo-Hermite-gaussian resonant eigenmodes for the spherical setting of the cavity prototype

data. This task can be performed by using the convolution method to filter the image noise.

Preliminary tests were done on some beam samples. The kernel used during these first attempts was a gaussian function with 10 pixels width in both the transverse directions. Looking at the second sample of TEM_{00} in Tab.6.2, the smoothed data gave as result an R^2= 0.9995 with ellipticity 0.998, which parametrizes the asymmetry of the beam. Still, the residual map of the smoothed data shows the same structure of the raw data. This means that the filtering process for such a filter does not corrupt the structure of the acquired data [see Fig.6.3].

From the data acquired one can conclude that our spherical cavity was able to sustain gaussian beams with a reasonable good shape with respect the environmental limits. The profile data were understood through a gaussian model with a precision which is more than 98 %. On the other hand, higher order modes were less precise and their residual maps sometimes showed a well defined structure and a strong asymmetry in the power distribution (see Fig.6.4). This asymmetry for higher order modes may be explained taking into account that the higher order transverse field modes explore a larger surface of the optics than the fundamental mode, and therefore sample more

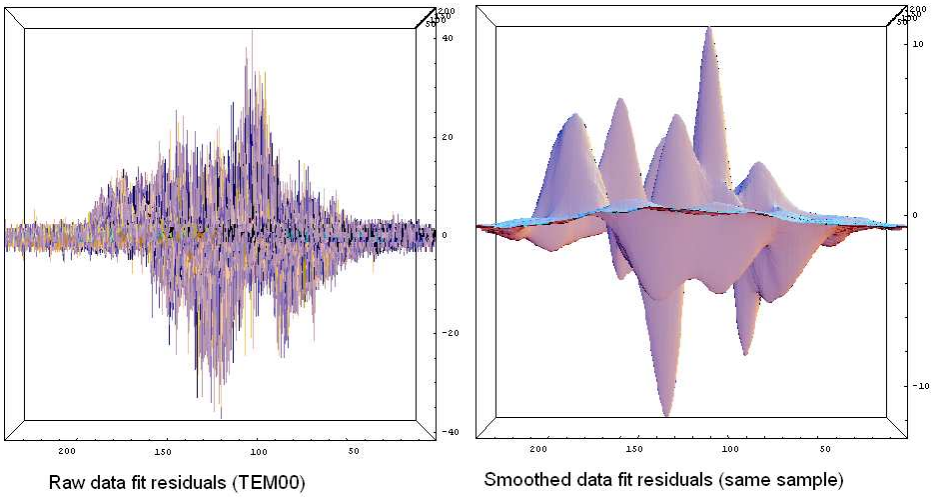

Figure 6.3: Example of image filtering effects on the fit residuals map: the random hot spots are completely erased but the residual structure is still present (kernel width = 10 pixels). Note that the maximum amplitude of the error is gone from about 40 digits to 10 digits (both raw data and the smoothed one have the same amplitude).

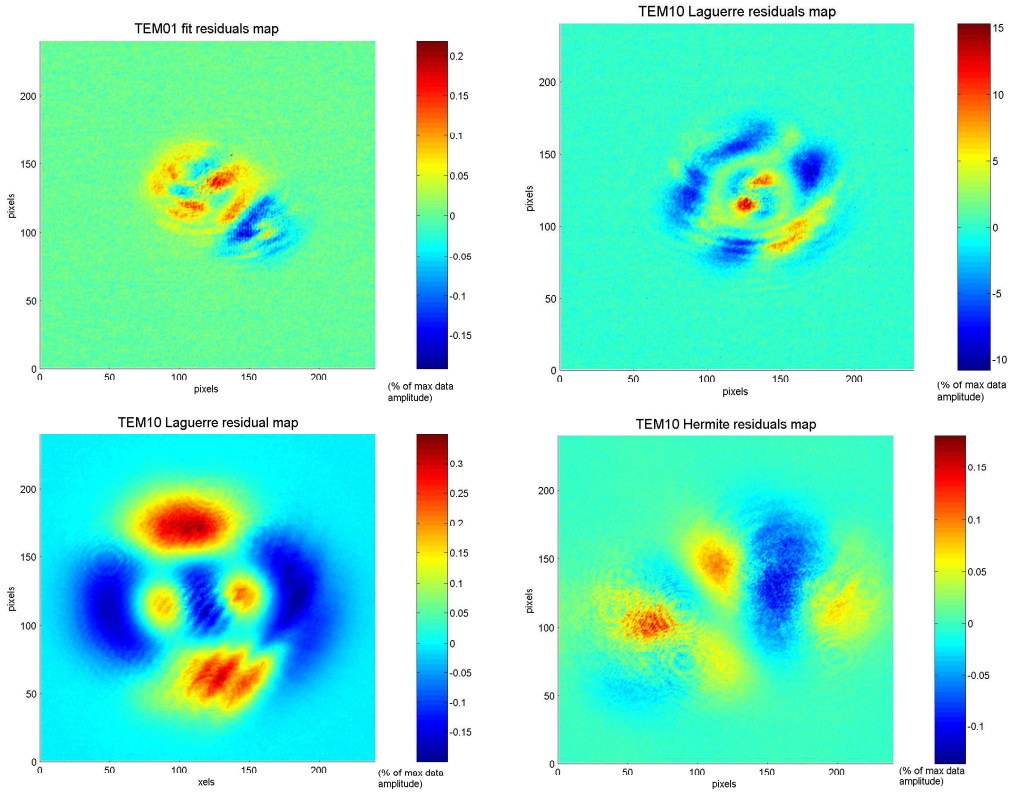

Figure 6.4: Residual maps for some of the acquired beam profiles: the two on the bottom have some resemblance with some transverse mode.

aberrations.

6.2 First results and analysis with the Mexican hat mirror

As done for the spherical optics cavity, the main purpose of study, when the first Mexican hat mirror was installed, was to characterize how a real MH resonator behaves, in particular the coupling with the gaussian input beam, the transverse modes, spectral structure, and their field distribution.

Before any meaningful work could be carried out, the best cavity alignment had to be found. We found that the cavity optical axis was very sensitive to the input beam positioning. In particular, the light beam started

to resonate just on one side of the mirror and the field distribution appeared as a small bump with oval shape, as shown in Fig 6.5. This is in contrast with what we saw during the operations with the spherical mirror, in which misalignment does not change the modes, but only moves them.

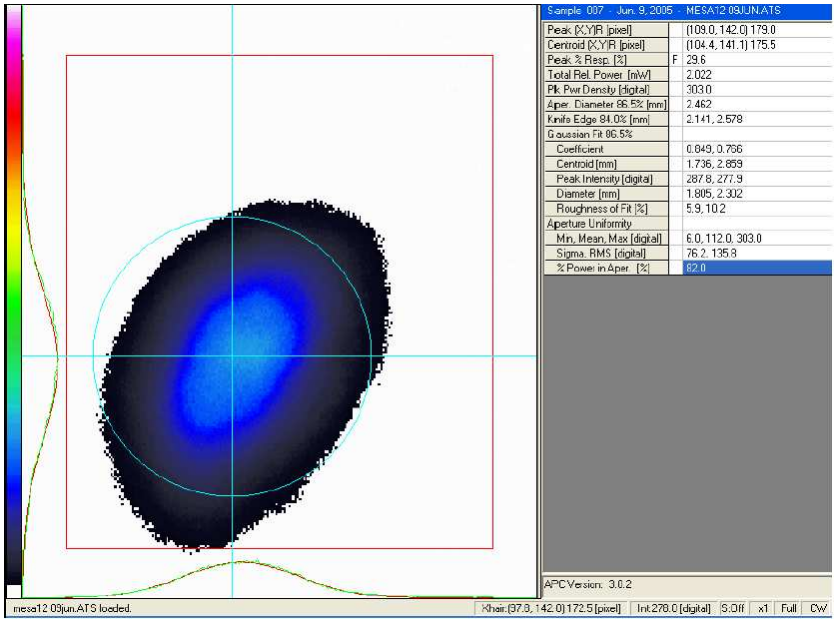

Figure 6.5: One of the first attempts to align the cavity. The Beam Analyzer software is showing the gaussian fit for the crossair one-dimensional profiles. These results seems very close to the actual profiles

This phenomenon can be explained as the result of the very low focusing power of the MH end mirror at its center, while on its edge it behaves almost like a spherical mirror surface and so it can focus much more the light on the flat surface of the input mirror.

Once the input beam was directed close to the centers of the input and end mirrors, we were able to lock the cavity to a number of transverse field patterns which resembled the ordinary Laguerre-gaussian eigenmodes. Some of these electromagnetic field patterns are shown in Fig. 6.6.

As shown in Sec.4.3, the expected resonant higher order modes have a cylindrical symmetric power distribution which differs from the analougus gaussian. Since there is no analytical formula for such cavity eigenfunctions, it is only possible to compare the numerical solution of the ideal cavity

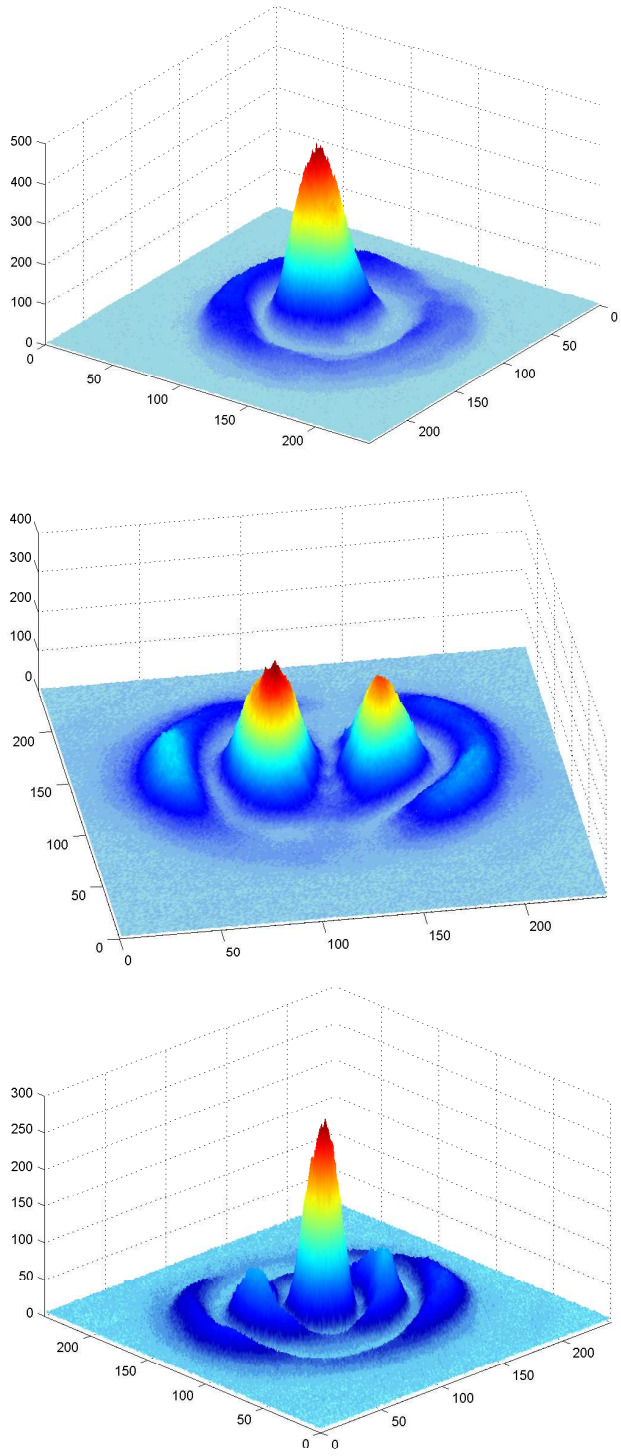

Figure 6.6: High order Mesa beam transverse modes. From the top: 'TEM_{10}','TEM_{11}','TEM_{20}'

eigenequation with the actual data. This comparison was done by taking as fit function the interpolating function for the mesa-eigenmode 'TEM'_{10} (the same data set plotted in Fig.4.4), scaled over the minimal gaussian waist size, so that b becomes the main fit parameter. The result for the one-dimensional profile are shown in Fig.6.7.

Even if the MH mirror profile is not ideal and the alignment could not be proved to be perfect, higher order mesa-modes resonate with beam shapes in a reasonably good agreement with theoretical behavior. Most of all, the hypothesis of "gaussianity" for these cavity 'TEMs' is completely excluded.

To align the cavity to the ideal fundamental mesa-mode was much more difficult. Cavity mirror alignment and input beam pointing determined the actual shape of the cavity fundamental mode, which in this case we can consider as the one with only one node. Fig. 6.8 shows one of these resonant beams which have a good resemblance with the ideal Mesa beam but an unexpected node on one side. In particular, this field pattern cannot be explained as a superposition of the eigenfunctions for the unperturbed cavity in a easy way.

Taking just the x section of this data set it is possible to perform a "qualitative" analysis of how "mesa" this beam is. In order to clean the data from the evident diffraction pattern on one of its sides, the x-profile data was extracted and preliminarily smoothed by convolution with a gaussian kernel. The analytical expression for the ideal Mesa beam was used as fit function, with b as fit parameter and the beam radius value $D = 4b$ as set for the nominal nearly-flat Mesa beam. Fig. 6.9 shows the result for the regression: the visual comparison of the data with the theory demonstrates that the steep fall on the tails of the beam is respected, while the flat-top shape is less precise than for an ideal Mesa beam. So one could guess there is a strange coupling effect even the x-direction.

The spectral structure of such a cavity behaves as an ordinary nearly flat spherical cavity. The expected frequency distribution inside a FSR has no longer has a symmetric structure. Still, the resonant frequencies should increase by increasing the mode order with a frequency separation of the order of half of a MHz, as shown in Tab 6.3.

The cavity was aligned trying to maximize the intensity of the transmitted peaks, in particular looking at the first one. It was helpful in order to find the best alignment for the input telescope on the input bench, but once

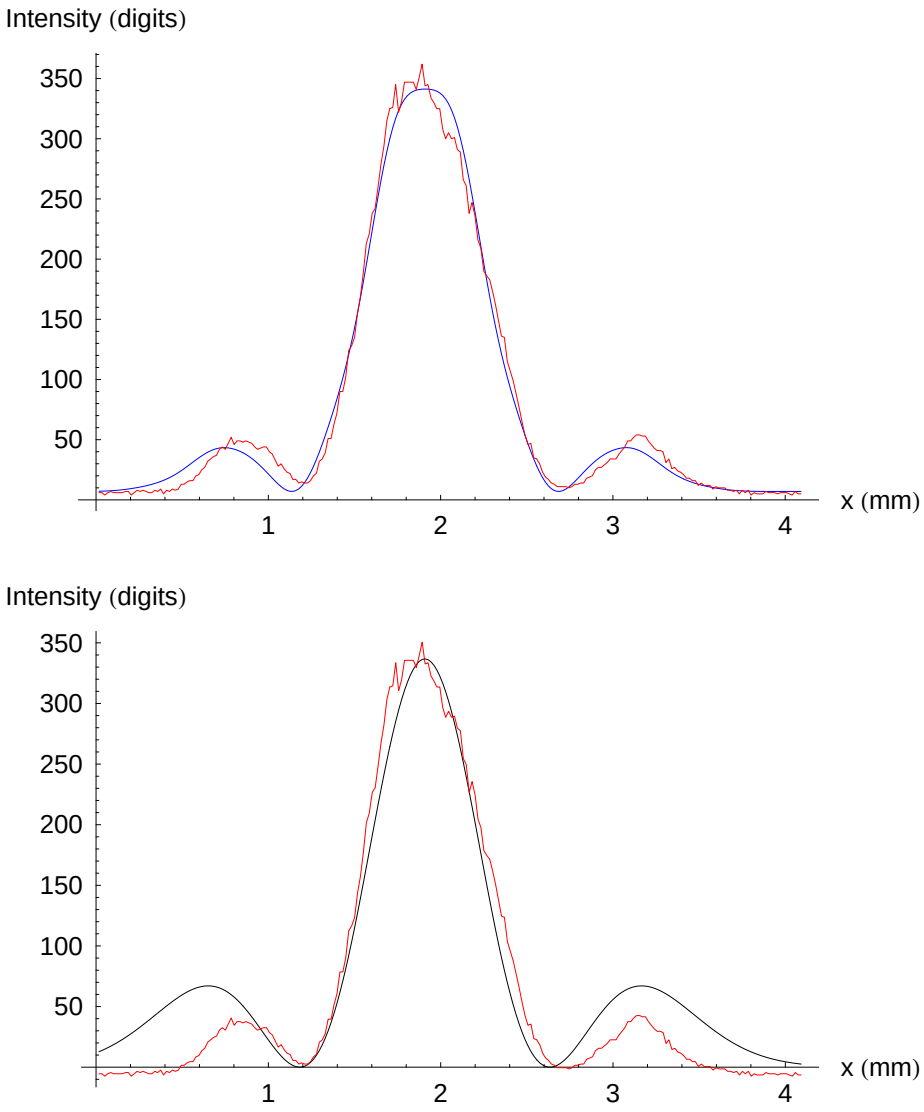

Figure 6.7: Results of the nonlinear regression for the 'TEM'_{10} x-profile. On the top, the fit function is the interpolating function of the numerical eigenfunction with one radial node. The coefficient of determination for this regression resulted $R^2 = 0.990$. On the bottom, the regression was performed with a Laguerre-gaussian function. In this case $R^2 = 0.929112$.

Figure 6.8: Two-dimensional beam profile of a quite flat resonant beam with a node.

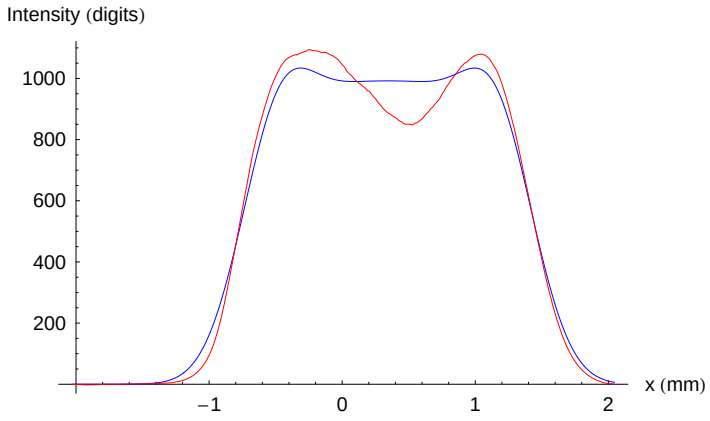

Figure 6.9: One-dimensional fit result for the data sample shown in Fig. 6.8 after smoothing process. The steep fall on the sides of the beam is almost perfectly respected.

	p = 0	p = 1	p = 2	p = 3	p = 4
l = 0	0	1.65422	4.40503	7.863	11.8556
l = 1	0.414052	2.87887	6.00313	9.75768	13.9934
l = 2	1.09453	4.17538	7.68077	11.7063	16.0626
l = 3	1.99054	5.55228	9.42209	13.7201	18.3046

Table 6.3: Frequency spacing between eigenmodes for the 7.32m long MH cavity prototype. The 'TEM'_{00} frequency is set equal to zero. The frequency values are expressed in MHz [58].

I tried to align the mirrors, the peak amplitudes didn't show any evident improvements.

The initial tests were also affected imperfect mode matching. Once a good compromise was found, the first spectral line became the highest. The best found mode shape for the 'TEM'_{00} is plotted in Fig 6.10. The lock for such a electromagnetic field wasn't neither very intense or stable. In fact, the power distribution oscillated between the two sides where the peaks were. As a qualitative comparison, in the same figure I plotted the linear superposition of the first two 'TEMs' for the unperturbed cavity with both the modes having the same power and a relative phase of 1.68 rad.

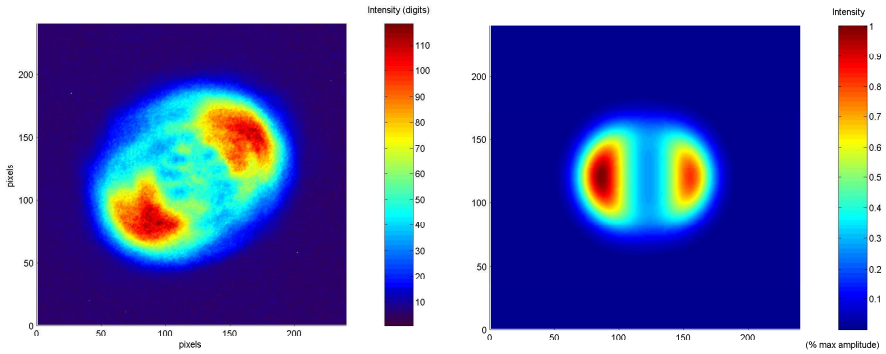

Figure 6.10: Fundamental mode for first configuration of the Mesa beam cavity prototype, and beside a linear superposition of the first two numerical eigensolutions for the cavity prototype.

Switching to dither locking did not change that the experiment preferred to keep its resonance on misaligned configurations (one peak on half of the

mirror surface for the 'TEM'_{00}) or distorted beams. As for the spherical optic case, the quasi-cylindrical symmetry of the resonant beams was gradually lost. In Fig. 6.11 one calibrated cavity spectrum is plotted.

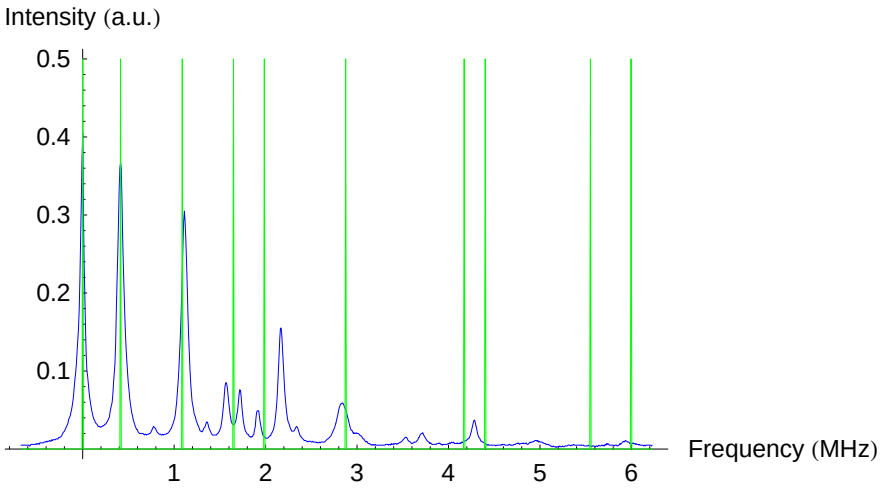

Figure 6.11: Cavity spectrum for the MH cavity prototype. The vertical lines are the calculated mode frequencies shown in Tab. 6.3.

As we expected, the regular frequency distribution of the cavity 'TEMs' is completely lost. Some of the lower order spectral lines (their frequencies are shown in Tab. 6.3) intercept the actual resonant peaks. Furthermore, more resonant peak than we expected are present. However, the known nonlinear translation of the piezos through a FSR (due to a not uniform response of the three actuators and to the mechanical clamping system shown in Fig. 5.5) does not allow us to conclude that we are in presence of large discrepancies from the theoretical prediction.

Another factor to take into account is that the eigenvalues were calculated solving the eigenequation for a cylindrical symmetric system. This yields a degeneration of the eigenvalues which is evidently broken in the real case.

6.3 Beam deformation modeling and analysis by FFT simulations

During the beam profile acquisition, I tried to model the misalignment effects we were observing on the resonant beam shape, using a dedicated Mathematica simulation code. It consists of an implementation of a Fast Fourier Transform (FFT) model [59] developed to simulate an optical system when realistic mirrors are included. This numerical program simulates the propagation of a light beam in a optical cavity using the paraxial approximation. The first simulations didn't take into account of the presence of a folding mirror and the real maps for the two flat mirrors. The final result of the simulation is the electromagnetic field on the input mirror surface. Since the field distribution changes when it propagates, the obtained map was then propagated through the free space which separates the input beam from the detector.

Since any alignment configuration could not be taken as reference to quantify the amount of cavity misalignments, I used the simulation tool to reproduce the grabbed beam profiles. Some of the measured unexpected resonant field patterns which resonate in the cavity are shown in Fig 6.12.

Some of these beams were reproduced by feeding into the cavity excited Hermite-gaussian functions as the cavity driving field. In this case, the waist used was the w_G as found in Sec. 5.5.1. The obtained results showed that small amounts of tilt at the MH mirror yield a complete transformation of field distribution. Applying as reference tilt angle $\theta = 4$ μrad in the vertical direction, many resulting beams from the simulation runs found a correspondence with the actual data.

For instance, the 'TEM' field with one large lobe, which seemed to be the most stable resonant beam inside the cavity, shows a remarkably good agreement with the fundamental mode of the perturbed cavity affected by a tilt of the Mexican hat mirror. Data and simulation result are plotted for this case in Fig. 6.13. Note that both these intensity distributions are affected by ripples in the central area due to the imperfections on the MH surface.

From this result, we can deduce that our cavity prototype loses a Mesa beam power distribution completely when the tilt misalignment is over a few micro radiant. Hence, the requirement for the cavity alignment amounts to less than 1 μrad. Once the cavity is misaligned, a new optical axis is defined and it intersects the MH mirror outside the central flat bump, so that the

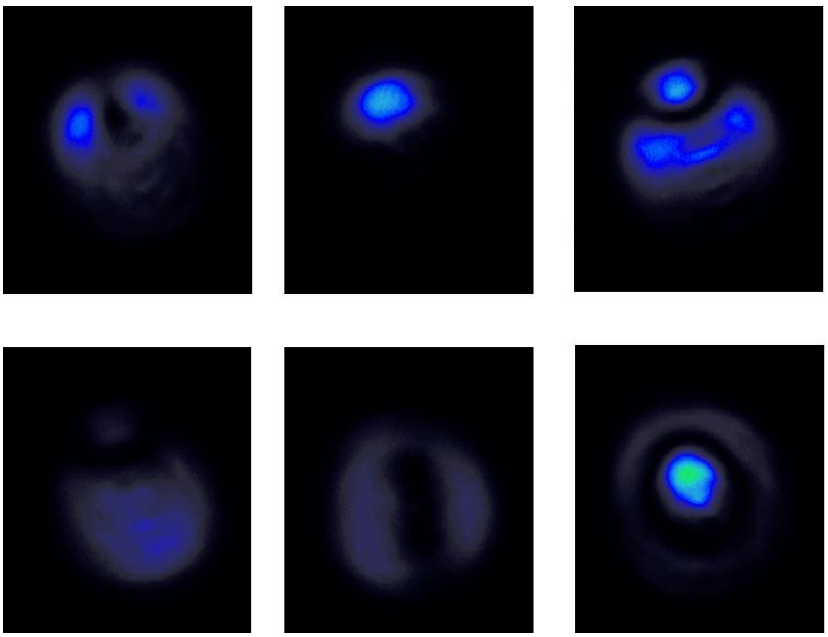

Figure 6.12: Some of the resonant field patterns found in the first test runs. The last two (corner bottom left) have a good resemblance with the unperturbed 'TEM'_{01} and 'TEM'_{10}

new fundamental mode has again a clear peak as for the gaussian case.

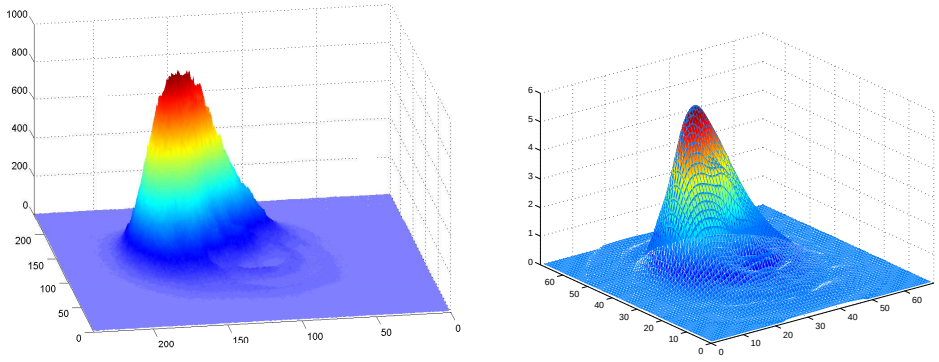

Figure 6.13: Comparison between real data and simulation with the installed MH mirror. The simulated power distribution was obtained applying 4 μrad tilt to the end mirror

As for the fundamental mode case, same agreement is observed for some distorted 'TEM'_{01} beam distributions around the new cavity axis, which were identified by feeding both the TEM_{01} and TEM_{10} Hermite-gaussian functions (see Fig.6.14).

Simulations were also performed to evaluate the impact of input beam offsets from the MH mirror center. For the unperturbed cavity, small translations of the input axis from the cavity axis do not affect the resonant beam shape. However, when the cavity mirrors are misaligned, small translations of the input beam direction from the end mirror center allow different couplings with the cavity resonant modes.

Fig 6.15 shows the resonant beam power distributions obtained simulating an input offset of $\pm$ 2 mm when the MH mirror is tilted of 4 μrad. When the input axis is close to the new one due to the tilt, the light resonates on the new fundamental and its maximum amplitude is increased with respect to a well centered input beam. On the contrary, when the input field is in the opposite direction, other transverse modes are on resonance.

Cavity simulations also confirmed that higher order 'TEMs' as the 'TEM'_{10} are not as affected by the mirror tilt as the fundamental [see Fig. 6.16]. Some simulation with a unmatched gaussian driving field also gave the TEM_{10} as cavity resonant mode.

Under the alignment limits enumerated in this section, there is no reason the cavity should not resonate on transverse modes which behave like the

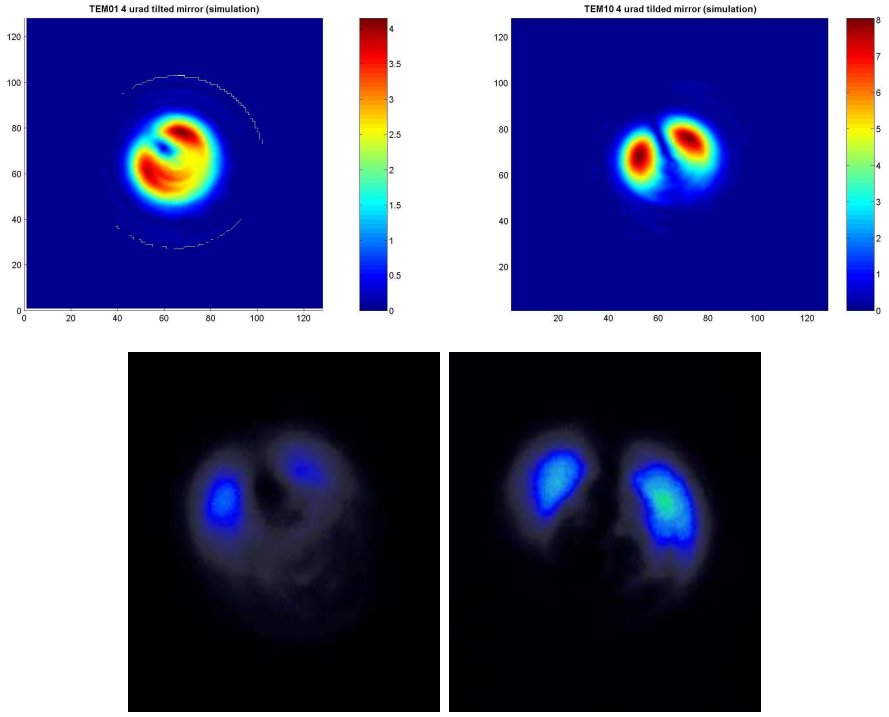

Figure 6.14: On the top, simulated higher order electromagnetic fields. On the bottom, two similar beam profiles from the CCD camera

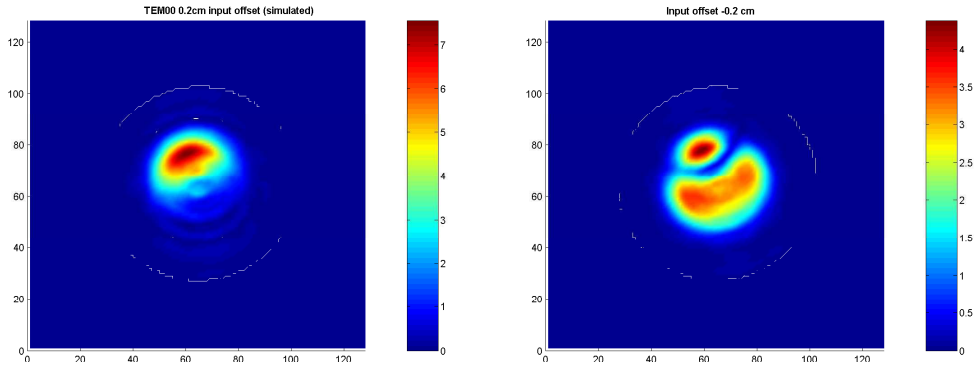

Figure 6.15: Evaluation of input offsets in the two opposite directions (+ 0.2 cm on the left along the vertical direction, - 0.2 cm on the left along the same direction) when the end mirror is tilted 4 μrad

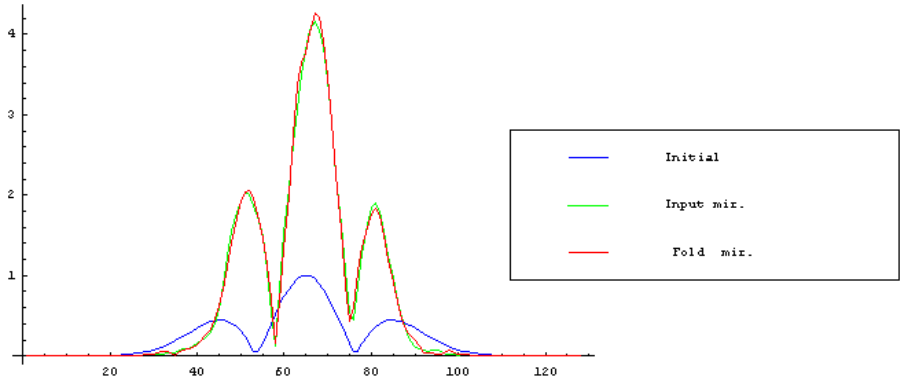

Figure 6.16: Simulated profile for the 'TEM'_{10} when a 4 μrad tilt is applied. The Laguerre-gaussian TEM_{10} was used as input beam (blue line). The power distribution is quite the same with a small shift on the tilt direction.

design Mesa beam.

6.4 New mirror mounting and first Mesa beam observation

In the previous section, cavity simulations showed that within 1 μrad angular adjustments precision and small input offsets (with respect the central bump size), the cavity fundamental mode should present all the main features of the ideal Mesa beam: a wider power distribution and a slightly cylindric shape with its top hat quite flat.

Another factor to take into account was the non-stationarity of the beam shape during the cavity operations: once a cylindrical symmetry was found for the resonant modes, any attempt to improve the alignment failed or made it worse.

A first check of systematics was to measure the flatness of the other two mirrors. The manufacture nominal flatness is $\lambda/10$ for He-Ne wavelength. Fig. 6.17 shows the measured surface maps for the input and folding mirror, when the clamping system was tight, a huge deformation is present.

We tried to correct this systematic changing the mirror mountings [see Fig. 6.18]. Since the thickness of these mirrors is 1 cm, much less than the 3

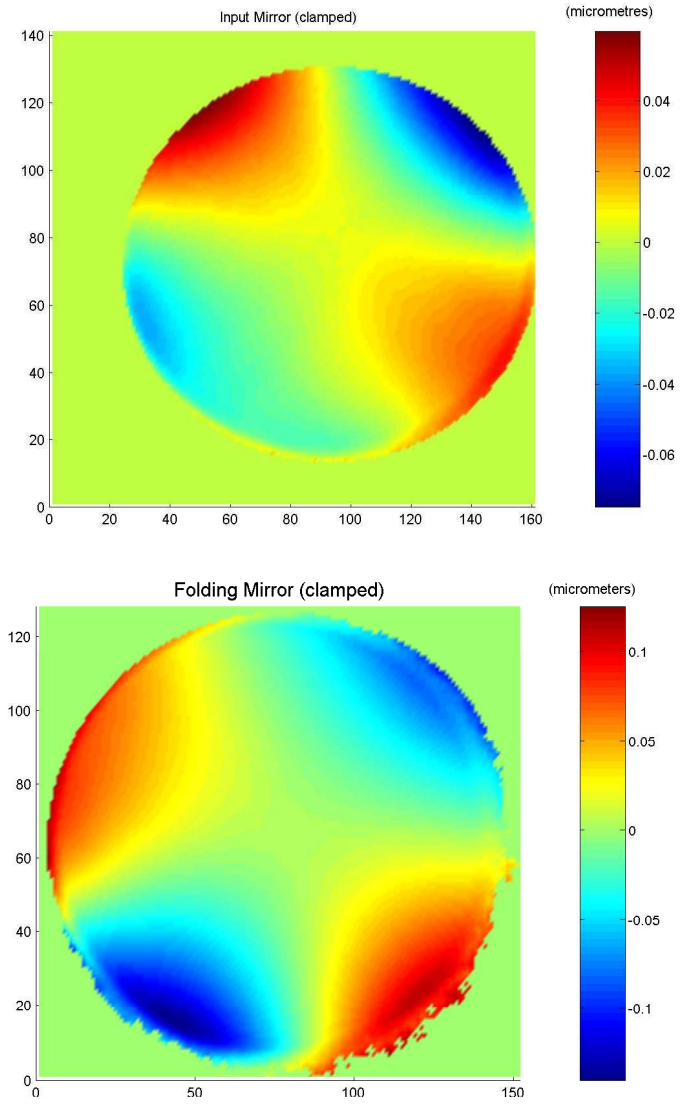

Figure 6.17: Flat mirrors maps with tight clamping. The deviation from flatness is about 60 nm for the input mirror and more than 100 nm for the folding mirror.

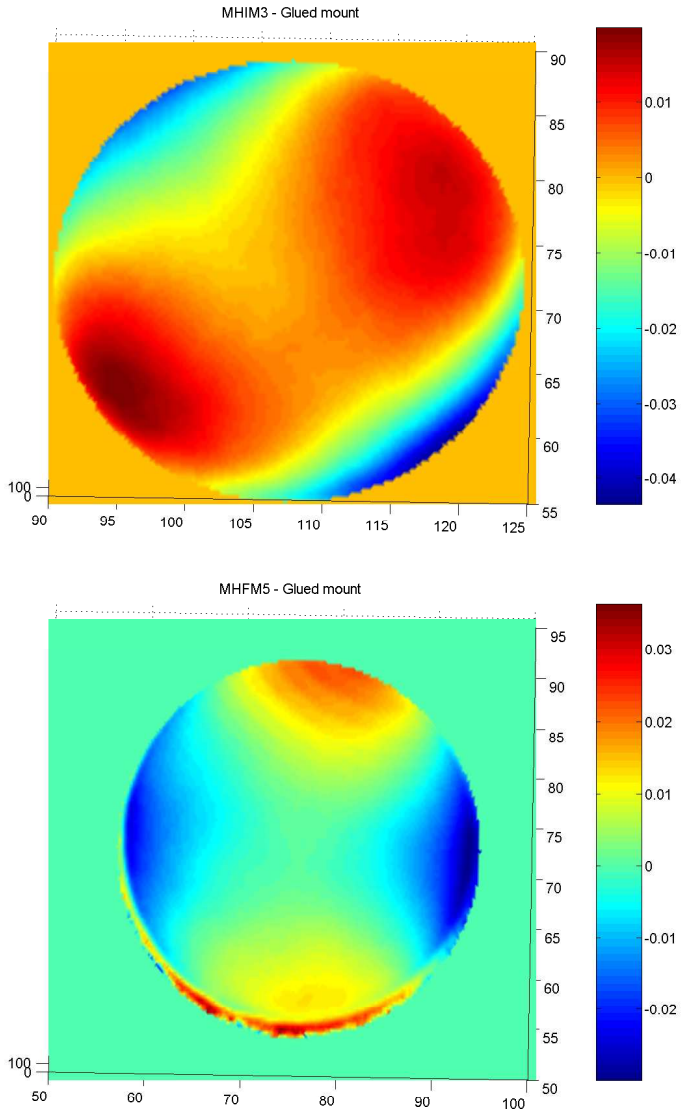

Figure 6.18: Flat mirrors maps after the new mounting system (the colormap unit is micrometer). On the top, the input mirror map; on the bottom, the folding mirror map.

cm of free space inside the monolithic holder, a spacing ring was placed on one side of both of these two mirrors. In this way, the piezos were directly pushing the coated surface nonuniformly, causing the strain distribution showed by the mirror maps.

The new holding system consists of two rings, instead of one, put on the two surfaces of the mirror, which now is glued to these ring with Vac-seal epoxy. In this way the stress is applied on the aluminum ring surface and the glue better averages the surface imperfections of the mounting rings.

The mirror surfaces were measured again and some deformations were still present. Comparing the two mirror profile data sets, we can observe that the new mounting system reduced the maximum height difference from the mirror's center from 60 nm to 10 nm for the input mirror, and from 100 nm to 20 nm for the folding mirror. The central part is also more uniform than before in both cases.

Other improvements were the installation of the final input mode matching lens and the change of the last two folding mirrors on the input bench. These have 2" diameter to reduce beam distortions or aberrations. The cavity itself was also better isolated from the air motion by closing the circular windows on the thermal shield at the ends of the cavity.

Finally, dithering the laser frequency and maximizing the first spectral peak in the transmission signal map, a good alignment compromise was found and a Mesa beam was locked on resonance. Fig. 6.19 shows this first event as it was acquired by the CCD camera.

Smoothing the data with a gaussian kernel with 5 pixel width, the power distribution shows a clear resemblance with the ideal Mesa beam. It shows also an evident asymmetry. A first analysis was done to evaluate how ideal this beams is. Nonlinear regressions on the transverse profiles of the beam are plotted in Fig. 6.21. Both the profiles show a residual tilt effect that could be explained as either a small mirror misalignment or a surface imperfection of one of the two flat mirrors of our resonator.

Since one peculiarity of the Mesa beam is its wider power distribution over the mirror surfaces, one interesting check is the extrapolation of the beam width on the folding mirror, where the analyzed beam comes from.

As definition of beam width for an arbitrary beam along an arbitrary axis, one is usually referred to the second-order moment of the beam power distribution as follow [32]:

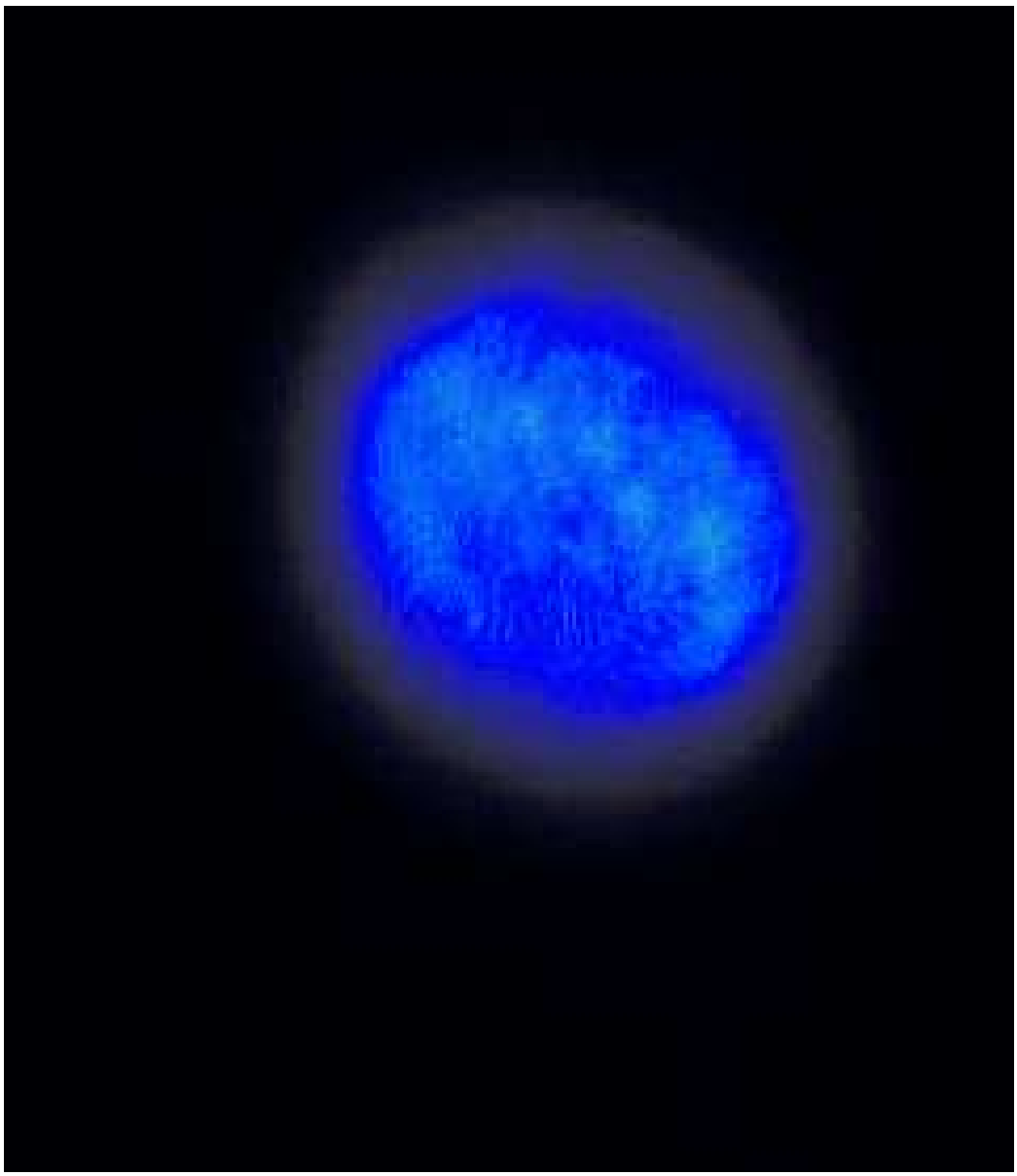

Figure 6.19: First Mesa beam profile as grabbed by the beam profiler. It is possible to observe the chromatic uniformity of the intensity distribution

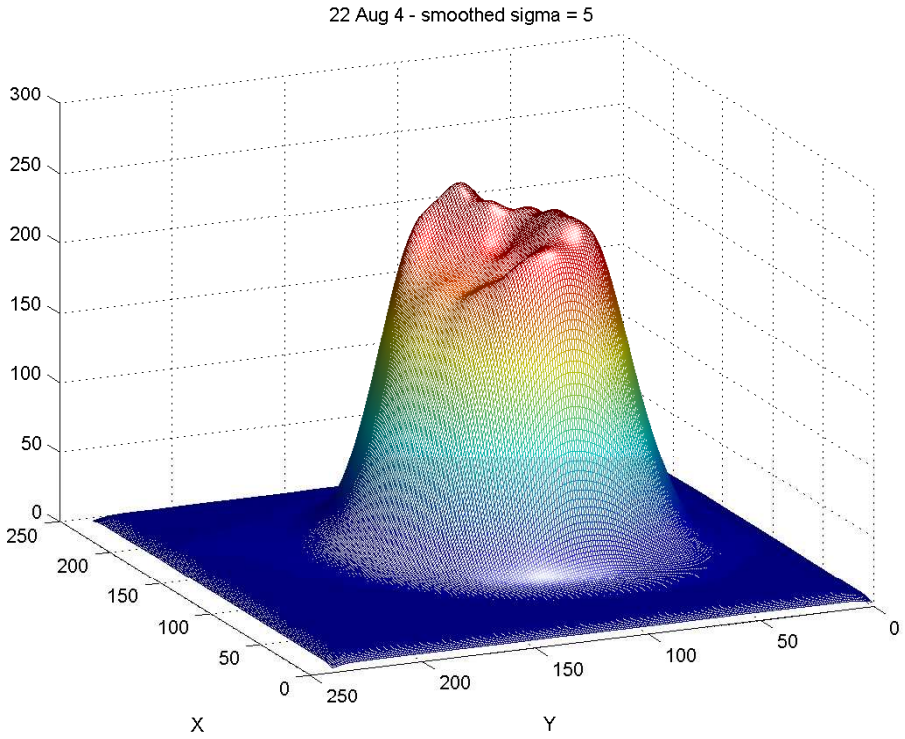

Figure 6.20: Three dimensional view of the Mesa beam intensity distribution. Smoothed data.

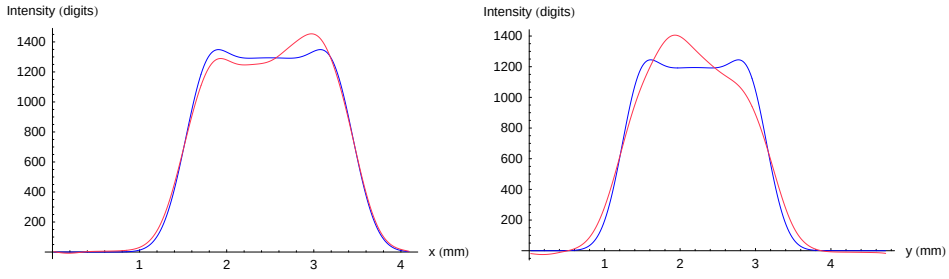

Figure 6.21: The smoothed profiles of the data shown in Fig. 6.20 are plotted with the best mesa fit function.

$$W^2(z) = \frac{4\int_{-\infty}^{+\infty} x^2\psi^2(x,z)dx}{\int_{-\infty}^{+\infty} \psi^2(x,z)dx} \tag{6.2}$$

Using this definition it is possible to show that the beam width amounts to 6.685 mm at the waist position, while after seven meters $W(z)$ is 6.679 mm. Even if the tails of the distribution are lightly larger, the power is distributed more on the central part in such a way that the second-order moment of the distribution corresponds to a power amplitude value higher than at the waist position. This represents a difference from the ordinary gaussian case. However, in our case the width changes are of the order of 10^{-3} mm, and we can use geometrical optics for a collimated light beam to estimate the expected beam on the folding mirror.

The numerical value at z_{fold} = 3.6 m for the Mesa beam width is taken $W(z_{fold})$ = 6.68 mm. Since the fit values are b_x =0.290 mm and b_y = 0.288 mm, then the widths on the camera are about $W_x(z_{CCD})$ =1.231 mm and $W_y(z_{CCD})$ =1.225 mm. These values are obtained just using Eq. 6.2 and 4.3[2]. Once the two focal lengths (f_1= 250 mm, f_2= 88.3 mm) and the space separations are known, the expected values for the beam widths on the folding mirror are W_x^{exp} =7.6 ± 0.9 mm and W_y^{exp} = 7.6 ± 0.9 mm, which we have to compare to $W(z_{fold})$. The large error is due to the not sufficiently precise measurement of the distances (error on the distance between the lenses is about 3 mm) of the di-focus system before the camera. This is translated in a very bad accuracy of the beam width estimation.

Although this estimate is quite rough, we can say that with a imperfect optics, the cavity environment has been able to resonate a transverse field distribution which is close to the design Mesa beam for a nearly flat cavity.

6.5 Conclusions

After about one year of commissioning and operations, the Mesa beam cavity prototype has been upgraded enough to permit the study of some optical features of the ordinary optical resonators with good accuracy. When the Mexi-

[2]It is possible to re-write ψ_{mesa} as function of z by using the minimal gaussian as function of z. Using Eq.4.3 the error amounts to some micrometers

can hat mirror samples were available, very interesting results were observed and experimental work was accompanied by a deep theoretical investigation to try to understand the acquired data.

Gaussian tests pointed our attention to some problems related to the optics: thin mirror substrates were subjected to stress deformations which changed the optical path of the resonant beam, allowing field pattern asymmetries and power distribution unbalances [60].

Initial tests and numerical simulations demonstrate that higher order modes with one or more radial nodes are less sensitive to cavity misalignments than the modes with transverse nodal lines. In particular, the 'TEM'_{10} coupled very well with a mismatched gaussian beam, even if it is the fourth line of the cavity spectrum. Both spectral lines and then FFT simulation confirmed this prediction.

During the test runs we saw how variable is the beam shape when misalignments and optics imperfections perturb a nearly flat MH cavity. At the moment, it seems that a good compromise could be quickly found so that a quantitative measure of how mirror tilts deform the fundamental Mesa beam mode. For what concerns the feasibility of the Mesa beam generation and control, we can conclude that the MH Fabry-Perot case is not very far from an ordinary spherical cavity.

About the MH mirror manufacture, first simulations revealed that ripples in the central area of the mirrors set a limitation of about 10 % PV on the flatness of the electromagnetic field pattern. Even the best data showed strong intensity fluctuation on that area which could be a not indifferent problem for the requirements of a GWID.

First tests set the limits of accuracy for all the optical cavity elements: a large flatness is required in the central area of all mirrors. The next step could be to switch to thicker substrates for the flat mirrors which avoid astigmatism effects and other asymmetries.

Another possible upgrade could be trying to use the particular behavior of the power distribution under cavity tilts to design an automatic alignment control. It would be a help for our experiment to ease the lock, and a first test for future application in GWIDs.

Appendix A

PZT Driver Circuit

This appendix wants to show the details about the design of cavity prototype's PZT Driver Circuit. The schematic diagram of the PZT Driver Circuit board is presented, the design of the printed circuit and the DC bias calibration.

As presented in Sec. 5.3, a digital panel voltage meter (DPM) was inserted in the design of such driver circuit for quantifying the translation produced by each piezo on the two cavity end mirrors. Fig A.3 shows the typical linear measurement done by the DPM. The fits results give us as result for all the channels

$$1 \text{ DPM count} = 0.244 \pm 0.003 \text{ V}$$

Hence,it is possible to know the exact amount of translation for each piezo translator using the calibration values found in Sec 5.5.2.

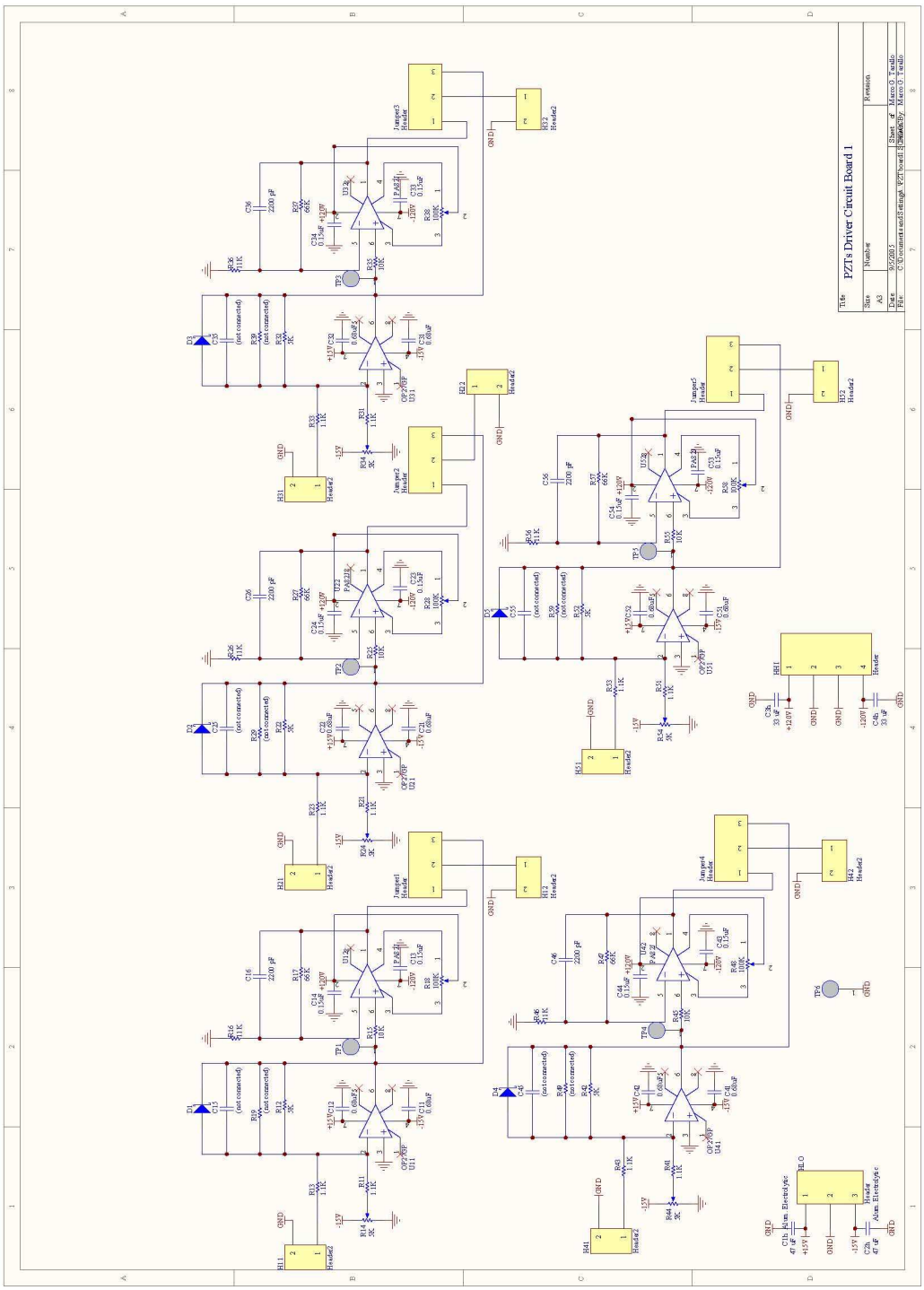

Figure A.1: Schematic diagram of the five channel board designed to drive the piezo translators on the cavity mirrors. A three pins header is used as jumper to select the high voltage or the low voltage stage output

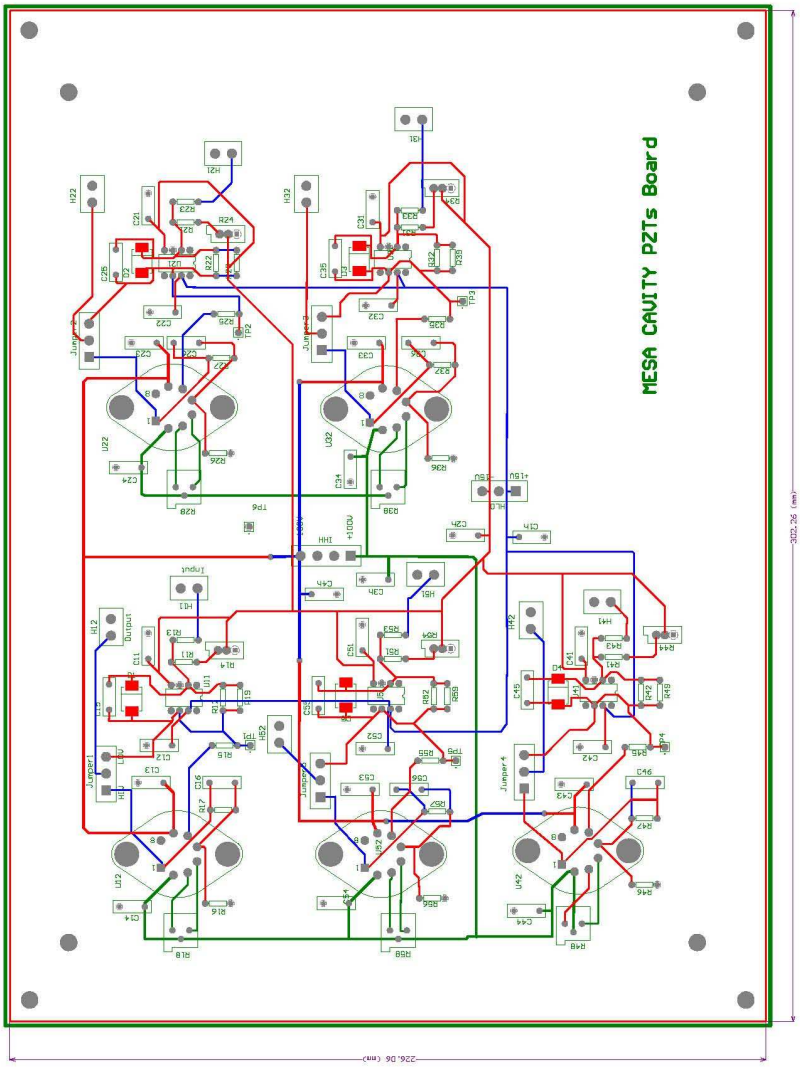

Figure A.2: Drawing of the printed circuit board where the driver channes were assembled. The green border symbolizes the internal (ground) plane

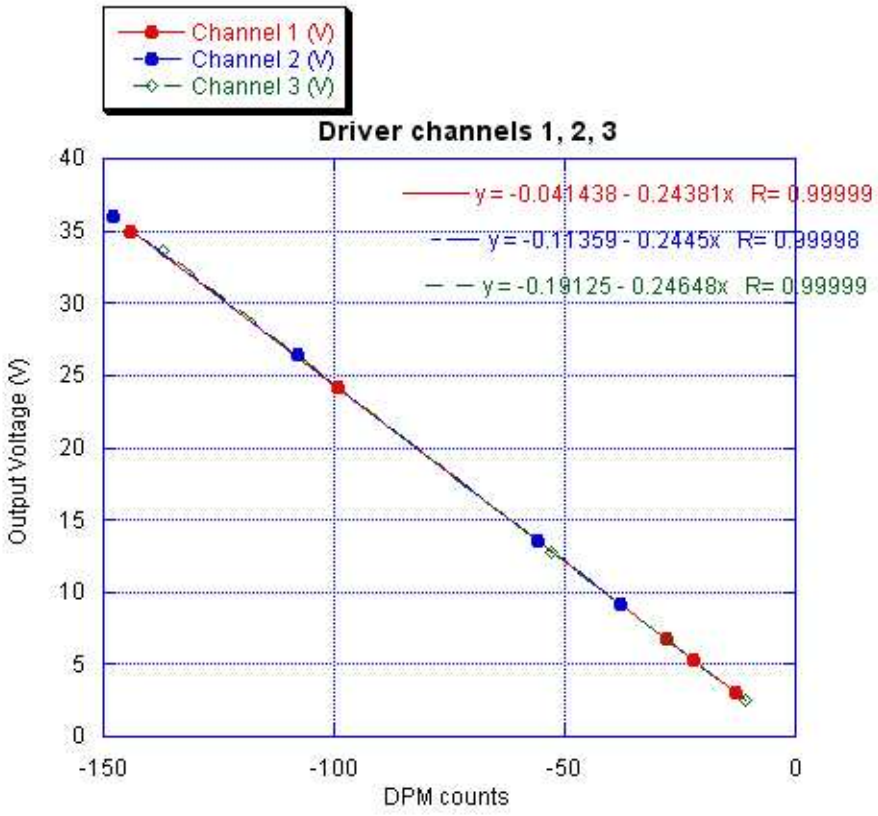

Figure A.3: Tipical behavior of the DC bias outputs mesured by the digital panel voltmeter of the driver

Appendix B

Mesa beam cavity mode matching

This appendix wants to point the attention on the MH cavity matching problem. The study of choosing the best telescope for the cavity mode matching is presented as a comparative analysis between the one lens and the two lenses optical system.

The predictions for such systems and some of the used "empirical" telescope layouts are than evaluated by means of the FFT simulations.

In the end, a table of possible input beam waist sizes is shown with the correspondent results. The input beam function used for the simulation is the normalized gaussian

$$\psi_{input}(r) = \sqrt{\frac{2}{\pi w^2}}\; e^{-\left(\frac{1}{w^2}+\frac{jk}{2R_{roc}}\right)r^2}. \tag{B.1}$$

B.1 Mode Matching Telescope

B.1.1 One lens mode matching

I want to study the best coupling issues for our cavity, starting from the two physical parameters that characterize our problem: waist size of the input laser and the length of the cavity itself.

$$\lambda = 1.064\ 10^{-3}\ \text{mm}; \quad \text{L} = 7320\ \text{mm}; \quad w_1 = 0.114\ \text{mm}.$$

Analytical calculations showed that for any MH Fabry-Perot cavity the best coupling occurs when a gaussian input perfectly matches the cavity waist with w_G as stated in Sec.4.3. If I take this value as my target, my mode match problem is reduced to a general gaussian problem. One way is try to solve it by using one single lens by using Eq.3.40. The problem was analyzed for the focal length $f = 2033$ mm, which was the only length available which satisfied the condition $f > f_0$ [see Eq.3.39].

The result is:

$$\text{for } w_2 = w_G, \qquad d_1 = 2046 \text{ mm}; \quad d_2 = 35657 \text{ mm}.$$

The nominal distance from the beam waist and the input mirror is considered to be 2863 mm (the same used for the spherical optics case). The Q value [see Sec.5.5.1] in this case would be Q = 0.016.

My target is trying to minimize the coupling efficiency Q. Let's try to see how much Q change when d_1 change. Solving Eq.3.40 the maximum achievable waist size is 6.04 mm. Eq.3.40 is just a particular solution of the general system of equations Eq.3.41 for the $\tilde{q}$ parameter. If I want to know how w_2 change with d_1 I should use that. The ABCD matrix elements for such system are:

$$\begin{aligned} A &= 1 - \frac{d_2}{f} \\ B &= d_1 + d_2 - \frac{d_1 d_2}{f} \\ C &= -\frac{1}{f} \\ D &= 1 - \frac{d_1}{f} \end{aligned}$$

The solutions for w_2 and d_2, which are related to the mode mismatch parameters, are found as function of d_1 [see Fig.B.1], and then the inserted in Eq.5.6.

The minimum is found at $d_1 = 2033$ mm and $\mathrm{Q}(d_1) =$ [see Fig.B.2].

B.1.2 Two lenses problem

We want to try to improve our Q using a telescope composed by two lenses (f_{in} and f_{end}) instead of just one. Let's start from the new transfer matrix

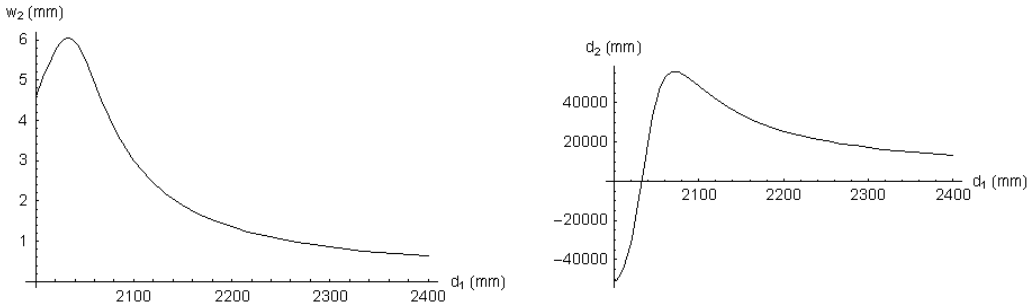

Figure B.1: Waist size and position as function of the lens position

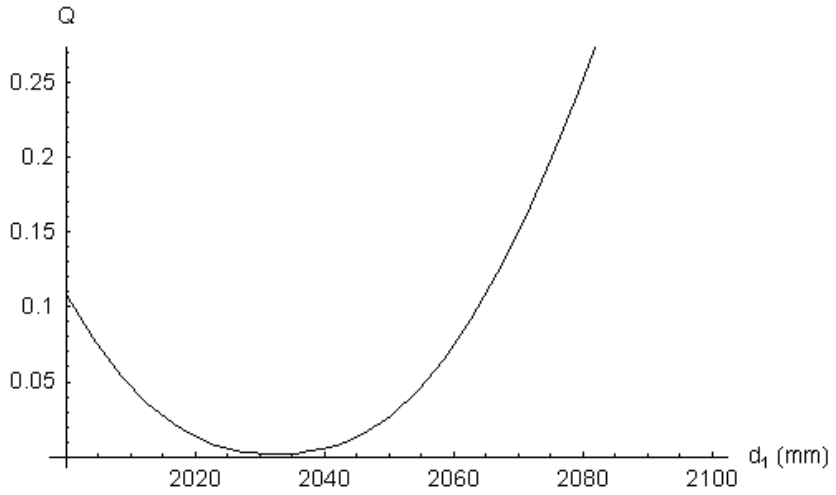

Figure B.2: Study of the best lens positioning (f = 2033 mm) to maximize cavity power coupling

for the new optical system (p_2 is the distance between the second lens and the cavity input mirror). The new ABCD matrix elements are:

$$\begin{aligned} A &= 1 - \frac{d_2}{f_{in}} + \left(-\frac{1}{f_{end}} - \frac{1}{f_{in}} + \frac{d_2}{f_{end} f_{in}} \right) p_2 \\ B &= d_1 + d_2 - \frac{d_1 d_2}{f} + \left(1 - \frac{d_1}{f_{end}} - \frac{d_2}{f_{end}} - \frac{d_1}{f_i n} + \frac{d_1 d_2}{f_{end} f_{in}} \right) p_2 \\ C &= -\frac{1}{f_{end}} - \frac{1}{f_{in}} + \frac{d_2}{f_{end} f_{in}} \\ D &= 1 - \frac{d_1}{f_{end}} - \frac{d_2}{f_{end}} - \frac{d_1}{f_{in}} + \frac{d_1 d_2}{f_{end} f_{in}} \end{aligned}$$

In this case the used procedure was: find the interval for d_2 where the di-focus system gives a real solution for $w_2 = w_G$. Then a value for this parameter is chosen as a compromise to get small values for d_1 and p_2.

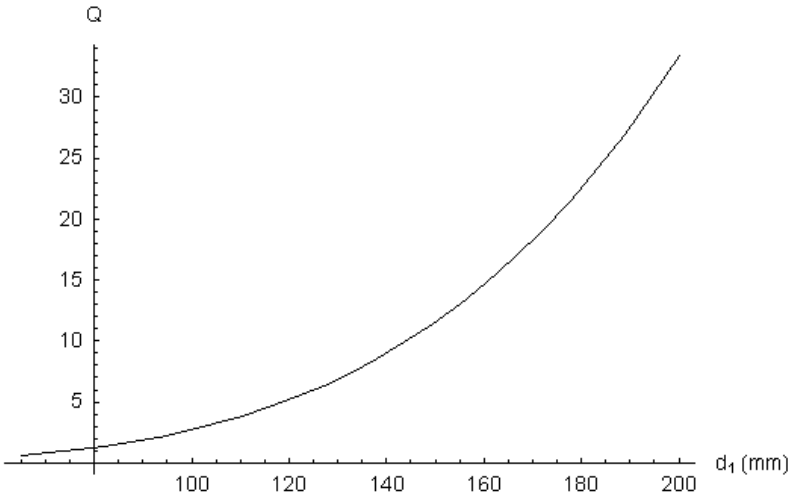

Figure B.3: Two lenses telescope: Q-curve for the system with f_{in} = -50 mm, f_{end} = 2000 mm, which has a magnification power of 40 close to the ratio between the two waists to transform into each other. Good Q values require a too small d_1.

The second step is leave w_2 free and, as for the one lens problem, minimize Q as function of d_1. Some Q-curve is shown in Fig.B.3 and B.4.

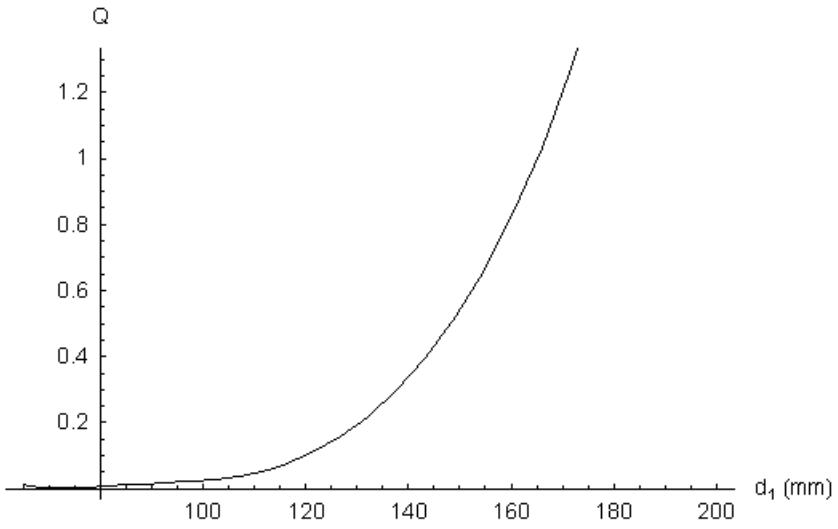

Figure B.4: Q-result for the two lenses telescope with f_{in} = -75 mm, f_{end} = 1000 mm. In this case for d_2 = 960 mm and d_1 = 105 mm, Q = 0.03.

Different solutions were studied for the two lenses telescope problem. The used focal lengths belonged to our laboratory lenses set. In the limit of physical constraints of the experimental setup, the found solutions for this problem were worse or at least comparable with the one lens result.

Thus, we decided to employ just one lens to match our Mesa beam Fabry-Perot cavity prototype.

B.2 Coupling efficiency estimation by FFT simulations

In table Tab.B.1 the FFT simulations results of the beam power at the input mirror are presented. In Fig.B.5 the first nine value of the previous table are plotted: the graph shows how the waist size mismatch affects the cavity power. The maximum is found at w = 0.57 cm, as expected.

The other values are the predicted w and R_{roc} for one lens solution (w = 0.606 cm, R_{roc} = -28675 cm) and two lenses (w = 0.637 cm, R_{roc} = -22732 cm), plus some other used configuration with -200 mm and 1000 mm focal

length lenses used during our preliminary runs.

Simulation results confirm our theoretical analysis. The expected power lack for the unperturbed cavity should be of about 0.4%, which is comparable with the found Q value.

Radius of curv.(cm)	**Waist (cm)**	**Cavity Power (W)**	**Cavity gain**
-10^8	0.570	71.3	8.44
-10^8	0.668	68.6	8.29
-10^8	0.700	66.8	8.17
-10^8	0.900	52.2	7.22
-10^8	1.200	34.0	5.82
-10^8	0.540	70.8	8.41
-10^8	0.440	59.3	7.70
-10^8	0.400	47.1	6.86
-10^8	0.370	33.3	5.76
-287000	0.606	71.0	8.42
-228000	0.640	69.2	8.36
-100000	0.606	70.8	8.42
-49980	1.200	33.5	5.79
-7898	0.635	35.2	5.92
7898	0.635	35.3	5.93
100000	0.606	70.8	8.41

Table B.1: Summary table about FFT simulations for the Mesa beam cavity prototype coupling with the driving (normalized) gaussian input beam. In the first part of the table, a waist mismatching evaluation is presented. The second half contains some realistic input beam parameters used to drive the cavity.

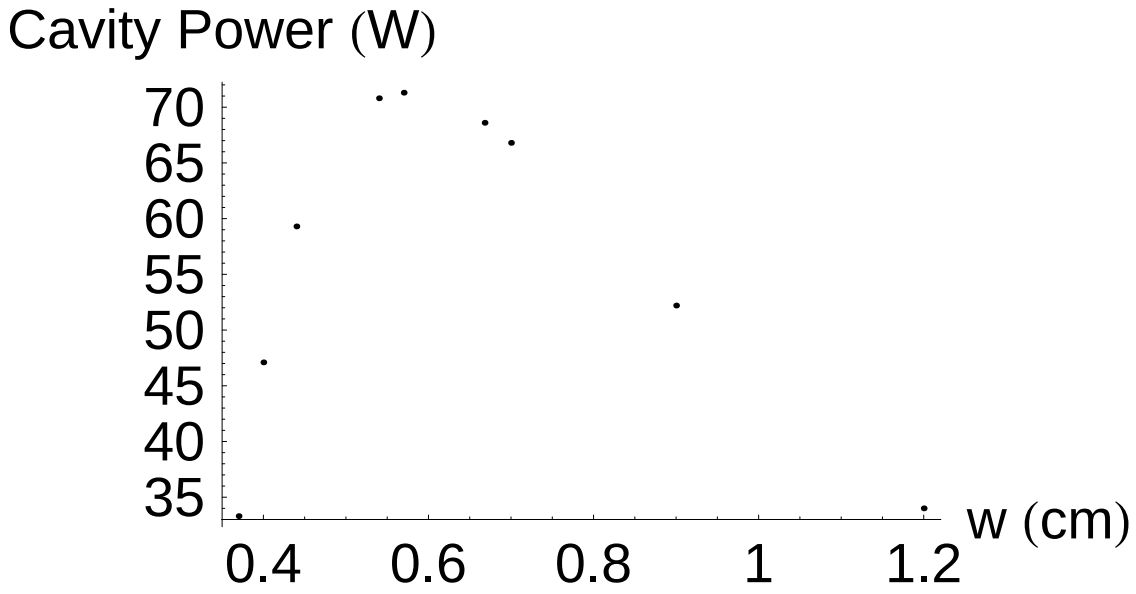

Figure B.5: Results of FFT simulations with a unitary power gaussian input beam with different waist sizes.

Acknowledgments

Many people deserve my acknowledgments, most of them at the LIGO Laboratories at Caltech, scientists, technicians and friends who never failed giving me their support and encouragement. I would like to thank Prof. F.Fidecaro and Dr. R. DeSalvo for giving me the chance to spend this year at Caltech, trusting me and always giving me precious suggestions.

I would like to thank Phil Willems who followed every step of my work, correcting my mistakes and appreciating my little successes. I would have never accomplished my task without his advice.

But nobody gave a contribute as determinant as Juri Agresti. He is a great scientist, a master in Mesa beams and Thermal noise, and always was a valid help for me. But he also became a true friend and almost a brother for me.

I also have to thank Dr. Erika D'Ambrosio for her suggestions and discussions about the theoretical implication of my experimental observations; Paul Russel and Ben Abbott for their patience and expertise when I built the electronics circuits; Garilynn Billingsley for her contribute on the mirror surfaces measurements; Lee Cardenas for his help during some cavity alignments and providing some optical components from his lab.

A special thank to John Miller, a great summer student at Caltech who gave a decisive support to get the last results and helped in writing this thesis.

I want to thank all the people that supported me during this long period with their patience and friendship, mostly when I was in a bad mood (almost always): Chiara, Artan, Paola, Domenico, Misha, Ciro and Simona, Enrico, Monica, Francesca, Alberto, Maria, Maria Paola, Ilaria, Sonia (logistic support in Pisa) and many many others.

The LIGO Observatories were constructed by the California Institute of Technology and Massachusetts Institute of Technology with funding from

the National Science 93 Foundation under Cooperative Agreement PHY-9210038.The LIGO Laboratory operates under Cooperative Agreement PHY-0107417

This thesis was attributed the LIGO DCC number P-050032-00-R.

Bibliography

[1] A. Einstein "Approximative integration of the field equations of gravitation" in *The Collected Papers of Albert Einstein*, pp. 201-210, Princeton University Press, 1987.

[2] R. Hulse and J. Taylor, "Discovery of a pulsar in a binary system," *The Astrophysical Journal*, vol. 195, pp. L51-L53, 1975.

[3] J. Taylor and J. Weisberg, "A new test of general relativity: gravitational radiation and the binary pulsar PSR1913+16," *The Astrophysical Journal*, vol.253, pp. 908-920, 1982.

[4] E. D'Ambrosio, R. O'Shaughnessy, S. Strigin, Kip S. Thorne, S. Vyatchanin and P. Willems, "Advanced LIGO: non gaussian beams", *Classical and Quantum Gravity*, vol.21, pp.867, 2004.

[5] B. Simoni "Design and Construction of a Suspended Fabry-Perot Cavity for Gaussian and Non-Gaussian Beam Testing. Preliminary Test with Gaussian Beam," Tesi Laurea Specialistica Univ. Pisa, LIGO-P040037-00-R, 2004.

[6] A. Einstein, *Anna. der. Phys.*, vol.17, pp. 549 ,1905.

[7] H. Nyquist, *Phys. Rev.*, vol.32, pp.110, 1928.

[8] H.B. Callen and T.A. Welton, *Phys. Rev.*, vol. 83, pp.34, 1951.

[9] R.F. Greene and H.B. Callen, *Phys. Rev.*, vol. 83, pp.1231, 1951.

[10] H.B. Callen and R.F. Greene, *Phys. Rev.*, vol. 86, pp.702, 1952.

[11] R.F. Greene and H.B. Callen, *Phys. Rev.*, vol. 88, pp.1387, 1952.

[12] J.L. Roubort and H.S. Sack, *J. Appl. Phys.*, vol.37, pp. 4803, 1966.

[13] C. Zener, *Phys. Rev.*, vol.52, pp. 230, 1937.

[14] C. Zener, *Phys. Rev.*, vol.53, pp. 90, 1938.

[15] P.R. Saulson, *Phys. Rev. D*, vol.42 N.10, pp. 2437-2445, 1990.

[16] Y. Levin, *Phys. Rev. D*, vol.57 N.2, pp.659, 1998.

[17] Y. T. Liu and K. Thorne, *Phys. Rev. D*, vol.62, ID 122002, 2000.

[18] F. Bondu, P. Hello and J.-Y. Vinet, *Phys. Lett. A*, vol.246, pp.227-236, 1998

[19] V. Braginsky and S. Vyatchanin , "Thermodynamical fluctuations in optical mirror coatings", *Phys. Lett. A*, vol.312, pp.244-255, (2003).

[20] V. Braginsky, M. Gorodetsky, and S. Vyatchanin, "Thermodynamical fluctuations and phot-thermal shot noise in gravtational wave antennae", *Phys. Lett. A*, vol.264, pp.1-10, 1999.

[21] G. M. Harry *et al.*, *Class. Quantum Grav.*, vol.19, pp.897, 2002.

[22] M.M. Fejer *et al.*, *Phys. Rev. D*, vol.70, ID 082003, 2004.

[23] R. O'Shaughnessy, S. Strigin and S. Vyatchanin, "The implications of Mexican-hat mirrors: calculations of thermoelastic noise and interferometer sensitivity to perturbation for the Mexican-hat-mirror proposal for advanced LIGO", gr-qc/0409050 v1, 2004.

[24] J. Agresti, "Flat Beam Profile to Depress Thermal Noise", *2005 Aspen Winter Conference*, LIGO-G050041-00-Z, 2005.

[25] H. Koegelnik and T. Li, "Laser Beams and Resonators", *Appl. Opt.*, vol.5, pp.1550-1567, 1966.

[26] A.E. Siegman, "Lasers", *University Science Books*, 1986.

[27] G.D. Boyd and J.P. Gordon, "Confocal multimode resonator for millimiter through optical wavelength masers", *Bell Sys. Tech. J.*, vol.40, pp.489-508, 1961.

[28] D.Z. Anderson, "Alignment of resonant optical cavities", *Appl. Opt.*, vol.23, pp.2944-2949, 1984.

[29] K.E. Oughstun, *Opt. Commun.*, vol.42, pp.72, 1982.

[30] H. Koegelnik, *Bell Sys. Tech. J.*, vol.44, pp.455-494, 1965.

[31] K. Kanzler, "Transformation of a gaussian laser beam to an Airy pattern for use in focal plane intensity shaping using diffractive optics", *SPIE Con. Laser Beam Shaping II*, 2001.

[32] P.A. Belanger and C. Paré, *Opt. Lett.*, vol.16, pp.1057, 1991.

[33] C. Paré and P.A. Belanger, *IEEE J. Quant. Elect.*, vol.28, pp.355, 1992.

[34] C. Paré and P.A. Belanger, *IEEE J. Quant. Elect.*, vol.30, pp.1141, 1994.

[35] P.A. Belanger, R.L. Lachance and C. Paré, *Opt. Lett.*, vol.17, pp.739, 1992.

[36] F. Gori, "Flattened gaussian beams", *Opt. Comm.*, vol.107, pp.355-341, 1994.

[37] A.A. Tovar, "Propagation of flat-topped multi-Gaussian laser beams", *J. Opt. Soc. Am. A*, vol.18, pp.1897, 2001.

[38] E. D'Ambrosio *et al.*,"Reducing Thermoelastic Noise in Gravitational-Wave Interferometers by Flattening the Light Beams", gr-qc/0409075 v1, 2004.

[39] E. D'Ambrosio, "Non-spherical mirrors to reduce thermoelastic noise in advanced gravity wave interferometers", *Phys. Rev. D*, vol.67, ID 102004, 2003.

[40] J. Agresti, Annual status report to the Doctoral School Board, Univ. of Pisa, LIGO-T040225-00-R, 2005.

[41] J. Sidles and D. Sigg, "Optical Torques in Suspended Fabry-Perot Interferometers", to be submitted to *Phys. Lett. A*, LIGO-P030055-B, 2003.

[42] P. Savov and S. Vyatchanin, "Estimate of Angular Instability for Mexican-Hat and Gaussian Modes of a Fabry-Perot Interferometer", LIGO-T030272-00-Z, 2003.

[43] M. Bondarescu and K.S. Thorne, "A new family of Light Beams and Mirror shapes for Future LIGO Interferometers", gr-qc/0409083 v1, 2004.

[44] J. Agresti, E. D'Ambrosio, Y. Chen, and P. Savov, *Phys. Rev. D*, in preparation

[45] Courtesy of E. D'Ambrosio.

[46] See Mephisto 800NE Users Manual.

[47] M. Heurs *et al*, "Simultaneously suppressing frequency and intensity noise in a Nd:YAG nonplanar ring oscillator by means of the current-lock technique", *Opt. Lett.*, vol.29, pp.2140-2142, 2004.

[48] A. E. Siegman, "How to (Maybe) Measure Laser Beam Quality", *Optical Society of America Annual Meeting*, 1997.

[49] "Fast M2 (k-factor) Measures with Photon BeamProfilerTM", Application Note 230, Photon inc. (available on line: www.photon-inc.com).

[50] J. Agresti *et al.*, "Flat Top Beam Cavity Prototype", Proceedings SPIE Conference in pubbl.

[51] J. Agresti *et al.*, "Design and Construction of a prototype of a Flat Top beam interferometer and initial tests", Proceedings Amaldi6 Conference, to be sub. to *Classical and Quantum Gravity.*

[52] G.Cella *et al.*, "Seismic attenuation performance of the first prototype of a geometric anti-spring filter", *Nucl. Instr. and Meth. A*, vol.487, pp.652-660, 2002.

[53] A. Remellieux, private document.

[54] Thorlabs DET110 data sheet available on web site thorlabs.com

[55] P. Willems, private communication.

[56] See Coherent's Beam Analyzer Software Users Manual.

[57] S. Wolfram, "The Mathematica Book", Wolfram Media, Inc., 5th ed., 2003.

[58] Courtesy of J. Agresti.

[59] J. Vinet, P. Hello, C. Man, and A. Brillet, "A high accuracy method for the simulation of non-ideal optical cavities", *J. Phys. I*, vol.2, pp.12871303, 1992.

[60] J. Agresti, private communication about preliminary FFT results with actual flat mirror maps.